Imperial College London

Doctoral Thesis

Modelling In-Situ Upgrading (ISU) of Heavy Oil using Dimensionless Analysis and Operator Splitting Methods

Author:
Julien Maes

Supervisor:
Prof. Ann H. Muggeridge
Prof. Matthew D. Jackson

A thesis submitted in fulfillment of the requirements for the degree of Doctor of Philosophy

in the

Department of Earth Science and Engineering

November 2015

Declaration of Authorship

I, Julien Maes, declare that this thesis titled, 'Modelling In-Situ Upgrading (ISU) of Heavy Oil using Dimensionless Analysis and Operator Splitting Methods' is entirely my work under the supervision of Prof. Ann H. Muggeridge and Prof. Matthew D. Jackson. All published and unpublished materials used in this theisi have been given full acknowledgement. This work has not been previously submitted, in whole or in part, to any other academic institution for a degree, diploma or any other qualification.

Julien Maes
Department of Earth Science and Engineering
Imperial College London

Copyright

"My mother said I must always be intolerant of ignorance but understanding of illiteracy. That some people, unable to go to school, were more educated and more intelligent than college professors."

Maya Angelou

IMPERIAL COLLEGE LONDON

Abstract

Faculty of Engineering
Department of Earth Science and Engineering

Doctor of Philosophy

Modelling In-Situ Upgrading (ISU) of Heavy Oil using Dimensionless Analysis and Operator Splitting Methods

by Julien Maes

The In-Situ Upgrading (ISU) of bitumen and oil shale is a very challenging process to model numerically because a large number of components need to be modelled using a system of equations that are both highly non-linear and strongly coupled. In addition to the transport of heat by conduction and convection, and the change of properties with varying pressure and temperature, these processes involve transport of mass by convection, evaporation, condensation and pyrolysis chemical reactions. The behaviours of these systems are difficult to predict as relatively small changes in the material composition can significantly change the thermophysical properties. Accurate prediction is further complicated by the fact that many of the inputs needed to describe these processes are uncertain, e.g. the reaction constants and the temperature dependence of the material properties.

The large number of components and chemical reactions involves a non-linear system that is often too large for full field simulation using the Fully Implicit Method (FIM). Operator splitting (OS) methods are one way of potentially improving computational performance. Each numerical operator in a process is modelled separately, allowing the best solution method to be used for the given numerical operator. A significant drawback to the approach is that decoupling the governing equations introduces an additional source of numerical error, known as splitting error. Obviously the best splitting method for modelling a given process is the one that minimises the splitting error whilst improving computational performance over that obtained from using a fully implicit approach.

Although operator splitting has been widely used for the modelling of reactive-transport problems, it has not yet been applied to models that involve the coupling of mass transport, heat transfer and chemical reactions. One reason is that it is not clear which

operator splitting technique to use. Numerous such techniques are described in the literature and each leads to a different splitting error, which depends significantly on the relative importance of the mechanisms involved in the system. While this error has been extensively analysed for linear operators for a wide range of methods, the results observed cannot be extended to general non-linear systems. It is therefore not clear which of these techniques is most appropriate for the modelling of ISU.

Analysis using dimensionless numbers can provide a useful insight into the relative importance of different parameters and processes. Scaling reduces the number of parameters in the problem statement and quantifies the relative importance of the various dimensional parameters such as permeability, thermal conduction and reaction constants. Combined with Design of Experiments (DOE), which allows quantification of the impact of the parameters with a minimal number of numerical experiments, dimensionless analysis enables experimental programmes to be focused on acquiring the relevant data with the appropriate accuracy by ranking the different parameters controlling the process. It can also help us design a better splitting method by identifying the couplings that need to be conserved and the ones that can be relaxed.

This work has three main objectives: (1) to quantify the main interactions between the heat conduction, the heat and mass convection and the chemical reactions, (2) to identify the primary parameters for the efficiency of the process and (3) to design a numerical method that reduces the CPU time of the simulations with limited loss in accuracy.

We first consider a simplified model of the ISU process in which a solid reactant decomposes into non-reactive gas. This model allows us to draw a parallel between the in-situ conversion of kerogen and the thermal decomposition of polymer composite when used as heat-shield. The model is later extended to include a liquid phase and several reactions.

We demonstrate that a ISU model with n_f fluid components, n_s solid components and k chemical reactions depends on $9 + k(3 + n_f + n_s - 2) + 8n_f + 2n_s$ dimensionless numbers. The sensitivity analysis shows that (1) the heat conduction is the primary operator controlling the time scale of the process and (2) the chemical reactions control the efficiency of the process through the extended Damköhler numbers, which quantify the ratio of chemical rate to heat conduction rate at the heater temperature for each reaction in the model. In the absence of heat loss and gravity effects, we show that the ISU process is most efficient at a heater temperature for which the minimum of the extended Damköhler numbers of all reactions included in the model was between 10 and 20.

For the numerical method, the standard Iterative Split Operator (ISO) does not perform well due to many convergence failures, whereas the standard Sequential Split Operator (SSO) and the Strang-Marchuk Split Operator (SMSO) give large discretization errors. We develop a new method, called SSO-CKA, which has smaller discretization error. This method simply applies SSO with three decoupled operators: the heat conduction (operator C), the chemical reactions (operator K) and the heat and mass convection (operator A), applied in this order. When we apply SSO-CKA with the second-order trapezoidal rule (TR) for solving the chemical reaction operator, we obtain a method which generally gives smaller discretization errors than FIM. We design an algorithm, called SSO-CKA-TR-AIM, which is faster and generally more accurate than FIM for simulations with a kinetic model including a large number of components that could be regrouped into a small number of chemical classes for the advection and heat conduction operator. SSO-CKA works best for ISU models with small reaction enthalpies and no other reaction than pyrolysis reactions, but can give a large discretization method for ISU models with non-equilibrium reactions.

Acknowledgements

First and foremost I want to thank my supervisors Ann Muggeridge and Matthew Jackson. It has been an honour to work with such dedicated professors. I appreciate all their contributions of time, ideas, and guidance to make my Ph.D. experience productive and stimulating. Their constant support and regular advice helped me to become closer to the researcher I want to be. I am especially thankful for the immense opportunity to do this work at Imperial College London. I would like to thank every student and staff member which contributes to make this institution such a motivating place to go to every morning. In particular, I would like to thank Dr. Adriana Paluszny for welcoming me in her teaching team.

This work would not have been the same without the contribution of Prof. Michel Quintard and all the people from Institut de Mécanique des Fluides de Toulouse. I am grateful for the time that I spent in France working with them and the speed with which they could accommodate me every time. Working with Michel allowed me to extend my knowledge to more application fields. I am grateful for having the opportunity to attend the 15^{th} International Heat and Mass Transfer conference in Kyoto with them.

I will always be grateful to my sponsor and ex-employer Total for offering me this great opportunity. For the past three years, people around me have been amazed by the generosity with which they accepted to sponsor me while I was resigning and not intending to come back. I would like it to be known that I left Total only because I wanted to become an academic and not because I was unhappy there. I hope I can work with them as much as possible in my future career. Especially, I would like to thank Alexandre Lapene who had the difficult task to manage the link between us, Total and IMFT. He did it exceptionally well and on top of that was able to be a precious help with the technical stuff.

Finally, I would like to thank my family for all their love and encouragement. For my parents, my sister and my two older brothers, who raised me with love. For my twin brother who helped keeping it real (and mostly fun). And most of all for my amazing partner Julia whose support during all the stages of this Ph.D. was so essential, and my baby daughter Madeline, who kept me awake and sharp at night. Thank you.

Contents

List of Publications

- Maes, J., Muggeridge, A. H., Jackson, M. D., Quintard, M., and Lapene, A. (2014). *Scaling heat and mass transfer in the presence of pyrolysis*, Heat and Mass Transfer (Wärme und Stoffübertragung), DOI 10.1007/s00231-014- 1391-4.

- Maes, J., Muggeridge, A. H., Jackson, M. D., Quintard, M., and Lapene, A. (2014). *Modelling heat and mass transfer in porous material during pyrolysis using operator splitting and dimensionless analysis*, Proceedings of the 15th International Heat and Mass Transfer Conference (IHTC-15), 10-15 August, Kyoto, Japan

- Maes, J., Muggeridge, A. H., Jackson, M. D., Quintard, M., and Lapene, A. (2015). *Modelling in-situ upgrading of heavy oil using operator splitting methods*, Journal of Computational Geosciences, DOI:10.1007/s10596-015-9495-6.

- Maes, J., Muggeridge, A. H., Jackson, M. D., Quintard, M., and Lapene, A. (2015). *Scaling analysis of in-situ upgrading of bitumen and oil shale.* Submitted to FUEL.

- Maes, J., Muggeridge, A. H., Jackson, M. D., Quintard, M., and Lapene, A. (2015). *Numerical simulation of in-situ upgrading of bitumen using operator splitting, adaptive implicit and Runge-Kutta methods.* Under preparation.

List of Figures

List of Tables

Abbreviations

AIM	**A**daptive **I**mplicit **M**ethod
AK	**A**dvection-**K**inetic
ASO	**A**lternating **S**plit **O**perator
BHP	**B**ottom **H**ole **P**ressure
CKA	**C**onduction-**K**inetic-**A**dvection
CMG	**C**omputer **M**odeling **G**roup
CPU	**C**entral **P**rocessing **U**nit
DA	**D**imensional **A**nalysis
DOE	**D**esign **O**f **E**xperiment
EOR	**E**nhanced **O**il **R**ecovery
EROI	**E**nergy **R**eturn **O**n **I**nvestment
ESDIRK	**E**xplicit **S**ingle **D**iagonally **I**mplict **R**unge-**K**utta
FEM	**F**inite **E**lement **M**ethod
FIM	**F**ully **I**mplicit **M**ethod
FVM	**F**inite **V**olume **M**ethod
IA	**I**nspectional **A**nalysis
IMPES	**IM**plicit **P**ressure **E**xplicit **S**aturation
ISO	**I**terative **S**plit **O**perator
ISU	**I**n-**S**itu **U**pgrading
KA	**K**inetic-**A**dvection
LTE	**L**ocal **T**hermal **E**quilibrium
ODE	**O**rdinary **D**ifferential **E**quation
OS	**O**perator **S**plitting
PDE	**P**artial **D**ifferential **E**quation
RK	**R**unge-**K**utta

RSM	**R**esponse **S**urface **M**ethodology
SAGD	**S**team **A**ssisted **G**ravity **D**rainage
SIA	**S**equential **I**terative **A**pproach
SMSO	**S**trang-**M**archuk **S**plit **O**perator
SNIA	**S**equential **N**on-**I**terative **A**pproach
SSO	**S**equential **S**plit **O**perator
TR	**T**rapezoidal **R**ule

Physical Constants

Stefan-Boltzmann constant	σ	$5.67 \times 10^{-8}\ W/m^2/K^4$
Universal gas constant	R	$8.314\ J/mol/K$

Symbols

A	pre-exponential factor	s^{-1}
a	mass stoichiometric coefficient	no unit
C	mass concentration	kg/m^3
c	compressibility	$1/Pa$
E_a	activation energy	J/mol
e	thermal expansion	$1/K$
h	specific enthalpy	J/kg
K	rock permeability	m^2 or $D = 9.869 \times 10^{-13}\ m^2$
L	domain length	m
m_w	component molecular weight	kg/mol
m	mass	kg
P	pressure	Pa
q	energy flow by conduction	W/m^2
r	reaction rate	s^{-1}
T	temperature	K
S	saturation	no unit
t	time	s
V	volume	m^3
v	fluid velocity	m/s
x	one-dimensional coordinate	m
α	permeability function parameter	no unit
γ	specific heat capacity	$J/kg/K$
Δh_r	reaction enthalpy	J/kg
ΔT	temperature scale $\Delta T = T_i - T_0$	K
$\delta\mu$	viscosity temperature derivative	$Pa.s/K$

ϵ	emissivity	no unit
κ	thermal conductivity	$W/m/K$
μ	dynamic viscosity	$Pa.s$ or $cp = 10^{-3}\ Pa.s$
ρ	mass density	kg/m^3
τ	time scale of heat conduction in porous media	s
ϕ	porosity	no unit
ω	phase composition	no unit

Subscripts

0	initial value
C	charred residual
D	Dimensionless value
G	gas component
g	gas phase
H	heater value
I	inert solid
R	reactant
s	solid

Chapter 1

Introduction

1.1 Background, context and literature review

Heavy oil and oil sands are important hydrocarbon resources that account for over 10 trillion barrels [61], nearly three times the conventional oil in place in the world. There are huge, well-known resources of heavy oil, extra-heavy oil, and bitumen in Canada, Venezuela, Russia, the USA and many other countries. The oil sands of Alberta alone contain over two trillion barrels of oil. In Canada, approximately 20% of oil production is from heavy oil and oil sand resources.

Thermal EOR (Enhanced Oil Recovery) techniques are generally applied to very viscous heavy oil. These processes involve the introduction of external energy to the reservoir by various methods such as steam injection or electrical heating. The heat produced results in higher temperatures leading to a reduction in oil viscosity and an increase of oil mobility.

In order to enhance extra heavy oil and tar sands recovery, the Steam Assisted Gravity Drainage (SAGD) process has been widely used. In this process, steam is injected from a horizontal well, and forms a steam saturated zone which is usually called steam chamber. The steam flows to the perimeter of this steam chamber from the wells and condenses. The heat is transferred by thermal conduction to the surrounding reservoir, the viscosity of the oil is reduced and so it flows, driven by gravity, to a horizontal production well below. SAGD was first introduced in the early 1980's by Butler and co-workers [16] and has been described and used in several pilots and commercial projects [14, 15, 81].

However, such a process comes with some drawbacks essentially associated with water management. Moreover, the resulting hydrocarbons are still extra heavy oil/bitumen. Pipe transport of such viscous oil is challenging and refining on site is often required.

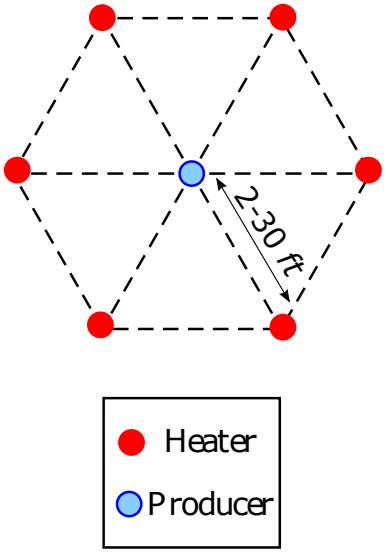

FIGURE 1.1: Top view of well pattern for in-situ upgrading process, Mahogany Field Experiment. The distance between a heater and a producer wells varies from 2 to 30 feets.

For these reasons, the process of In-Situ Upgrading (ISU) by subsurface pyrolysis has been applied in various pilot projects and laboratory experiments [28, 49]. The ISU process generally uses tightly spaced electrical heaters to slowly and uniformly heat the formation by thermal conduction to the conversion temperature of about 350 ^0C. At this temperature, the long chain oil molecules decompose through a series of chemical reactions of pyrolysis and cracking. Figure 1.1 shows the well pattern for the Mahogany Field Experiment, which is a part of the Shell's Colorado field pilot [28]. For these experiments, the distance between two wells varies from 2 ft ($\simeq 0.6m$) to 30 ft ($\simeq 9\ m$)

There are various potential advantages of using an ISU process. Firstly, at the recovery stage, there would be no requirement for a nearby water supply and water recycling facilities. Secondly, since upgrading of the oil takes place in-situ, the heavy components like coke will be left in the reservoir, and so the produced oil is lighter and of higher commercial value [82]. As a result, using the ISU process could lead to a reduction in the amount of required infrastructure and expenses on site for refining and pre-upgrading before transport.

To model the ISU process involves representing several physical and chemical phenomena. In addition to the flow of fluids through porous media and the change of properties with varying pressure and temperature, ISU involves transport of heat, evaporation, condensation and several chemical reactions. The temperature scale goes from reservoir temperature to several hundreds of degrees Celsius. As a result, thermodynamic and petrophysical properties vary significantly within the reservoir.

Numerical simulation of the outcome of ISU is challenging because of the large number of physical processes that need to be modelled, their varying time-scales and the non-linearity of the equations describing these processes. Accurate prediction is further complicated by the fact that many of the inputs needed to describe these processes are uncertain, e.g. the reaction constants and the temperature dependence of the material properties [30, 34].

Analysis using dimensionless numbers can provide a useful insight into the relative importance of different parameters and processes, especially if combined with Design of Experiments (DOE), which allows quantification of the impact of the parameters with a minimal number of numerical experiments. Dimensionless numbers are often used to scale laboratory results to the application length scale and conditions, and may be developed using techniques such as dimensionless Analysis (DA) [74] and Inspectional Analysis (IA) [78]. Ranking the different parameters controlling a given thermal decomposition application enables experimental programmes to be focused on acquiring the relevant data with the appropriate accuracy.

However, the main problem encountered when predicting the outcome of the ISU process is the time required for the numerical simulations. For the simulation of conventional reservoir processes such as water or solvent flooding, the fluid properties are generally described with a compositional model that includes only a limited number of pseudo-components (< 10). However, kinetic models describing heavy oil and kerogen decomposition generally include more than 20 components [8, 12]. Solving the transport step with such a large number of components is computationally expensive. Yet the chemical operator on its own is described by a set of Ordinary Differential Equations (ODE) that can be solved locally and represents a small computational effort in comparison with the transport step. Decoupling techniques, or so-called operator splitting methods, provide a framework to deal separately with each operator. This way, a large number of

components can be used to model accurately the chemical reactions but the transport step could be solved with a lumped model including only a small number of pseudo-components, potentially leading to large speed-ups with limited loss in accuracy.

However, decoupling the governing equations introduces an additional source of numerical error, known as the splitting error. Finding the best decoupling strategy that preserves the main interactions while splitting errors are limited is the challenge of this work. The use of dimensionless analysis combined with DOE could help us identify these main interactions and lead to the design of a more efficient splitting method.

In this chapter, we discuss the kinetic modelling of heavy oil cracking. The literature review on the subject highlights the importance of using an accurate model to describe the chemical reactions. We then discuss the use of fully coupled methods for the numerical simulation of the ISU process. We introduce Operator Splitting (OS) methods as a potential solution to reduce the computational time. These methods have been applied to various reactive transport models [5, 6, 23, 25, 41, 68, 76, 91]. We then present the aim and objectives of this work and provide a summary of the following chapters.

1.2 Heavy oil upgrading kinetic model

Oil and gas accumulations result from the evolution of petroleum systems over geological time. Kerogen, an organic constituent of some sedimentary rocks (known as source rocks) is a precursor to oil that forms during sediment diagenesis. Kerogen, which is not soluble in water nor in common organic solvents, is progressively thermally cracked and transformed into petroleum fluids during sediment burial. It first decomposes into bitumen which is soluble in organic solvents. It is then subsequently cracked into hydrocarbon rich oil, with further thermal maturation typically leading to light crude oil and gas. These oil and gas products often migrate through adjacent rock layers until reaching the surface or becoming trapped within a porous rock reservoir. In the reservoir, this oil and gas products may be subject to alteration [86]. Nearly all the deposits of heavy hydrocarbons are degraded products of accumulations of conventional oils. By heating the reservoir to a temperature of above 300^oC, the ISU process attempts to reproduce the natural geological maturation of kerogen in order to obtain a lighter product, but at a much faster rate.

The ISU process can also be applied to oil shale reservoirs. Oil shale is the term used to describe the fine textured rock of sedimentary origin that contains kerogen. The kerogen of oil shale is not distinct from the kerogen of source rocks that transform to petroleum fluids through geological time. However, the natural maturation process, which would eventually lead to oil and gas, is at a very early stage and may still require millions of years. This process can be accelerated through ISU. Unlike oil sands, oil shale initially has a very low permeability, until kerogen breaks down through reactions of pyrolysis, which opens up pores for flow. The fundamental aspects of kerogen pyrolysis upon heating in industrial processes are similar to the ones of natural diagenesis [86]. Thermal ISU processes for producing hydrocarbons from oil shale have gained attention recently, in part because of promising results reported by Shell [22].

Thermal cracking of extra-heavy oil and oil shale can be described by a compositional kinetic model. The pyrolysis products from kerogen and bitumen are dominated by heteroatomic (N, S, O) compounds, of very high molecular weight. The $NSOs$ are primary products of kerogen decomposition and hydrocarbons are generated from secondary cracking of these $NSOs$ [7, 8, 86]. Depending on reservoir pressure, pyrolysis of kerogen and bitumen happens over a large range of temperature from 150^oC to 800^oC. In the absence of oxygen, pyrolysis usually takes place at $250 - 300^oC$ during which the asphaltenes crack into saturates and aromatics. An accurate compositional model is a pre-requisite to be able to predict the chemical reactions that occur in this process.

A first kinetic model of oil cracking has been proposed by Tissot and Espitalie [85]. Ungerer et al. [87] derived a more detailed model but still simple enough to be calibrated on pyrolysis experiments of real oils. Braun and Burnham [12] reported a significant deviation with the measured cracking rate when this model is used at temperature less than 420^o C. They proposed a more complex and rigorous model that accounts for this discrepancy. Behar et al. [8] extended this model by focusing on the most unstable chemical classes of oils: the C_{14+} saturates, aromatics and polar compounds $NSOs$. The model can be extended to include thermal cracking of the $C_6 - C_{14}$ classes. A full kinetic model is described by [49] and its reaction scheme is represented in figure 1.2.

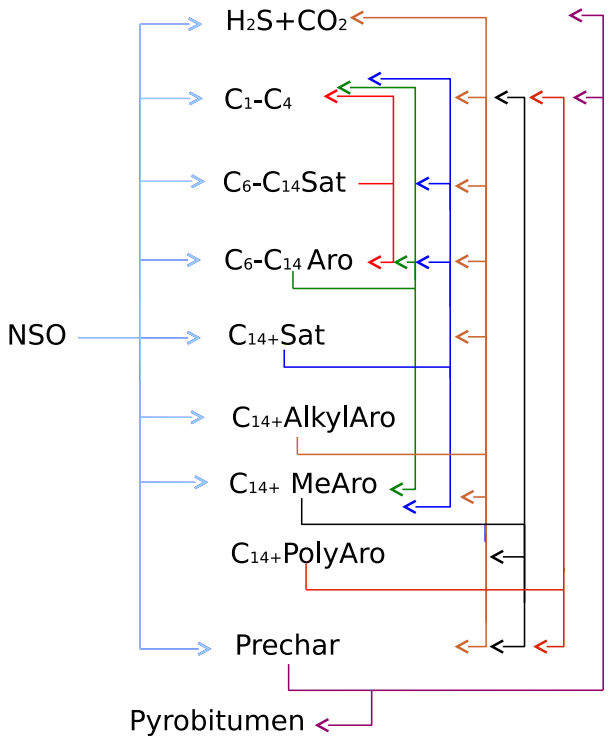

FIGURE 1.2: Kumar's kinetic model reaction scheme (figure from [49])

1.3 Fully Coupled Numerical Methods for Thermal Reactive Reservoir Simulation

Thermal reservoir processes are inherently highly non-linear. The mass transport, heat transfer and phase behaviour of these thermal compositional systems, in which the components partition across multiple fluid phases as a function of composition, pressure and temperature, are difficult to model accurately. When solving the transport problem in thermal reservoir simulation, the coupled non-linear conservation equations of mass and energy are discretized using different techniques, for instance the Finite Volumes Method (FVM) or the (mixed) Finite Elements Method (FEM). The resulting discrete equations are generally solved using various methods based on Newton's algorithm [63, 89].

The numerical simulation of thermal reactive transport processes brings up several challenges. The energy conservation equation leads to strongly coupled phenomena. A fully implicit strategy is generally applied in order to preserve this coupling. In conventional

reservoir simulation, chemistry and heat transfer do not play a key role in the transport equations. Hence, the coupling between transport and thermodynamics is driven by the pressure and a special strategy can be applied to the linear solver, that is known to be the most time consuming computational kernel and the bottleneck for scalable parallel simulation [17]. In the case of strong thermal coupling associated with chemical reaction, the pressure is no longer the main driving variable.

In addition to that, the large number of components and chemical reactions involves a non-linear system that is often too large for full field simulation. The IMPES (IMplicit Pressure Explicit Saturation) method can potentially reduce the computational time but sometimes requires unaffordable small time-steps to prevent instabilities [20]. The Adaptive Implicit Method (AIM) [73] seeks a middle ground between the Fully Implicit Method (FIM) time stepping, which allows large time-steps but is expensive in CPU time and storage, and an IMPES-type method. With AIM, the expensive implicitness is confined to the part of the simulation that requires it, allowing the rest of the computation to be done explicitly. AIM is widely used for thermal compositional simulations with a large number of components and the stability analysis is well-known [20, 59]. However, accounting for chemical reactions is very challenging. They tend to be stiff and very localized leading to very small time-steps. Accordingly, solving such a problem is very expensive in terms of CPU time.

A detailed compositional simulation of the In-Situ Upgrading of oil shale is given by [24]. A kinetic model for the thermal cracking of kerogen has been implemented in the Stanford General Purpose Simulator (GPRS) using FIM and was used to simulate the Mahogany Demonstration Project-South (MDP-S) conducted by Shell [28]. The numerical experiments conducted in this study show that the time-steps required in ISU simulation are much smaller than in compositional simulation without reactions.

1.4 Operator Splitting Methods

Operator splitting is a widely used method for solving reactive transport problems [25, 41]. The basic idea is to split the original problem into a sequence of smaller problems. Then, dedicated solvers can be applied to each operator. IMPES-based (or

AIM) transport codes can be coupled with chemical reaction models. For example, accurate ODE (ordinary differential equation) solvers can be employed to cope with the sometimes stiff systems of equations describing the chemical reactions. In addition, different time stepping strategies can be applied to the different operators, and in the case of ODE, local time steps may be used.

Operator splitting methods have been routinely employed in models to describe hydrogeochemical transport [5, 6, 91], atmospheric systems [51], combustion-reaction problems [68], and multiphase flow problems in petroleum engineering applications [23, 76]. However, the challenge of applying them to ISU resides in the presence of multiphase thermodynamics with stiff fronts coupled with chemical reactions. Choosing carefully among the numerous operator splitting methods, i.e., achieving an acceptable compromise between accuracy, computation resources and time, is essential.

OS methods offer two distinct approaches. In a Sequential Non-Iterative Approach (SNIA), each operator is applied once sequentially [5]. The classical SNIA, also called Sequential Split Operator (SSO) can be modified by using two time steps and alternating the order of the operators, as it is done in the Strang-Marchuk Split Operator (SMSO), also called the Alternating Split Operator (ASO) [51]. On the other hand, in the Sequential Iterative Approach (SIA), iterations are performed between each operator until convergence is obtained for each time step [45]. The most common SIA is the Iterative Split Operator (ISO), also called implicit-explicit iterative method.

However, a significant drawback of splitting technique is that they introduce an additional source of numerical error, known as the splitting error. Valocchi and Malmstead [88] showed that for one-dimensional transport with first-order radioactive decay, SSO generates a splitting error of order one. Kaluarachchi and Morshed [44] extended this result to the one-dimensional advection-diffusion-reaction equation with first-order reaction under steady-state flow. They showed that an order one error occurs for SSO and an order two error for SMSO. This error can be decreased by reducing the time-step size. Alternatively, ISO removes the splitting error through sequential iterations.

Convergence and stability of SSO, SMSO and ISO have been established for linear reactive transport [26, 38, 40, 71] and observed in some particular cases of non-linear reactive transport [29, 45], although this does not necessary apply for strongly non-linear problems such as ISU. The applicability of SIA depends mainly on the stability

requirements and the rate of convergence of the iterations [38] and can be challenging to obtain because of the implicit-explicit treatment of the operators [42].

Even when stable and convergent, the use of OS methods generates additional computation cost to obtain a precision equivalent to a fully coupled approach, either by decreasing the time-step size or iterating through the splitting scheme. However, when the splitting error is limited, the use of efficient dedicated solvers for each operator can potentially generate large speed-ups.

1.5 Objectives and Summary of Chapters

The objective of this work is to evaluate the use of OS methods for the modelling of the ISU process. Since the convergence and precision of these methods depend strongly on the various couplings in the model, we first try to identify which physical parameters have the most impact on the process. We use dimensionless groups to reduce the number of parameters. The use of DOE allows quantification of the impact of the dimensionless numbers on the energy efficiency of the system. This analysis provides the groundwork to the development of a new splitting method that preserves the main interactions so the splitting errors are limited. Dedicated solvers are then used to improve the computational cost of the transport step and the precision of the chemical reaction step.

In Chapter 2, we define a simplified model where a solid reactant decomposes into non-reactive gas. This model enabled us to draw a parallel between ISU and thermal decomposition of polymer composite when used as heat-shielding for spacecraft re-entry. This meant our numerical model could be validated by comparison with experimental result obtained by Henderson and Wiecek [34], where a thin slab formed of polymer composite material was subjected to a pure radiant heat flux. Our simplified model was able to reproduce the coupling between heat propagation, chemical reaction and gas flow with good agreement for this test case. Inspectional Analysis was used to determine the minimum number of dimensionless groups that can be used to describe both processes. Particular attention was given to the Damköhler number D_K, which describes the ratio of chemical reaction rate to heat conduction rate at a hypothetical infinite temperature, and the Arrhenius number N_a, which quantifies the ratio of activation energy of the reaction to potential energy. Our analysis highlights the importance of both numbers and allows

us to identify a new dimensionless number, called the extended Damköhler number $\tilde{D_K}$ which is a combination of D_K and N_a and quantifies the chemical reaction rate at the heater temperature. The study of $\tilde{D_K}$ enabled us to define a reaction temperature for the process.

Chapter 3 describes the use of DOE to identify primary parameters for both processes. A two-level factorial design [2] with Response Surface Methodology (RSM) [65] is used to examine the relationship between the response and the parameters of the experiment, leading to a classification of the dimensionless numbers as primary parameters, secondary parameters and insignificant parameters. The methodology is first applied to study the energy efficiency of thermal decomposition of kerogen into gas. We focus the study on the kinetic parameters of the decomposition. We observe that, when the extended Damköhler number is small, the reaction is slow and the process is inefficient. However, when the Damköhler number is very large, the reaction is very fast, but since the heat conduction is the primary mechanism for the process, an important part of the energy given to the system is simply used to heat up the rock. This analysis allows us to identify an optimal heater temperature for the performance of the process. We then use the same methodology to measure the performance of polymer thermal protection systems. We observe that the most important numbers for this case are the reduced volumetric heat capacity of the reactant Γ_R^* and the reduced heat of decomposition Δh_r^*. Indeed, while the reactant is consumed, the temperature increases slowly as the system requires enough energy for the decomposition. This analysis allows us to identify a protection temperature and a protection time.

For both cases, we observe that the heat conduction was the primary mechanism controlling the process, until the chemical reaction becomes important. Apparition of large volume of gas generated by the chemical reactions results in an increase of pressure until the flow becomes important. This observation can help us design a robust splitting method for the numerical simulation of the process. The main interactions are conserved in a decoupling method where the heat conduction is performed first, followed by the chemical reaction and finally the heat and mass convection step.

Chapter 4 focuses on the numerical methods. We describe the most common OS methods used in the literature. We observe that ISO failed to converge for our model. SSO and SMSO provide converged solutions but generate a large discretization error. Based on

the final observations of Chapter 3, we develop a novel splitting method, defined as SSO-CKA, where the heat is transported by conduction first, followed by a chemical reaction step, and finally the mass and heat convection is performed. SSO-CKA provides the best results in term of precision and performance. However, the splitting error still needs to be controlled to avoid large discretization errors and instability. We use DOE to study the performance of the method when applied to a large panel of physical parameters. A time-stepping strategy based on time truncation error of 0.01 is applied to both FIM and SSO-CKA. We observe that the most important parameters for the precision of SSO-CKA are the extended Damköhler number $\tilde{D_K}$, the reduced volumetric heat capacity of the reactant Γ_R^* and the reduced heat of decomposition Δh_r^*. We show that a potential way to ensure that the splitting error remains limited is to apply a time-step strategy with a target time truncation error of 0.005 instead of 0.01.

The methodology is extended to a more complete mathematical model describing the ISU of heavy oil and oil shale in Chapters 5 and 6. We use DOE to study the energy performance of the process. We then study the impact of the Damköhler numbers D_{Ki}, one for each reaction, on two test cases, one representing the ISU of bitumen, and one representing the ISU of oil shale. We study the optimal temperature for the two test cases and obtain a similar correlation as for the simplified model described in Chapter 3.

We then evaluate the use of OS methods for the ISU of heavy oil and oil shale. Again, we observe that ISO does not perform well due to convergence failure and that SSO-CKA gives the least discretization error of the four SNIA methods. We compare the error of FIM and SSO-CKA when we apply a time-step strategy based on the time truncation error. The discretization error is lower for SSO-CKA than for FIM when the reaction enthalpies are neglected. When the reaction enthalpies are not neglected, the error is larger than for FIM. This can be solved by dividing the target time truncation error by a factor 2.0, but the computational cost is also increased by two.

Another way of reducing the discretization error is to apply a higher order method to the chemical reaction operator. We apply the second-order trapezoidal rule and the third-order four stage explicit singly diagonal implicit Runge-Kutta method described by Kvaerno [50]. These methods reduce the discretization error with none or limited

additional computations. We then study the impact of equilibrium deviation on the energy efficiency of the process and the performance of the numerical method.

Finally, we summarize our findings and conclusions in Chapter 7, and we give recommendation for future work.

Chapter 2

Modelling thermal decomposition of solid reactant into non-reactive gas

This chapter treats a simplified form of the In-Situ Upgrading system: the thermal decomposition of a solid reactant into non-reactive gas. This system used a simplified description of the fluid by treating all reactants of the decomposition as solid and all products as non-reactive gas. This allows us to initially focus the analysis on three physical mechanisms: the thermal conduction, the heat and mass convection and the chemical reaction. Later in Chapter 5, the model is extended to include a liquid phase and several reactions between solid, liquid and gas components.

To quantify the relative importance of each mechanism is essential to understand the behaviour of the system. For example, the temperature for which the chemical reaction starts to be significant depends on the time scale of the whole process. If no heat is injected in the domain, the time scale is simply the time taken to consume all reactant at initial condition and the reaction is significant at initial temperature. Dimensionless analysis provides a useful insight into the relative importance of different parameters and mechanisms.

This chapter has three main objectives. First, we develop and validate a mathematical model that describes the thermal decomposition of solid reactant into non-reactive gas. We consider two applications: the thermal conversion of oil shale into non-reactive

gas and the thermal decomposition of polymer composites when used as heat shielding during spacecraft re-entry or for rocket nozzle protection. Secondly, we identify the set of dimensionless numbers that fully represents the system. They depend on the choice of a reference time scale for the process. Finally, we use these dimensionless numbers to define the temperature for which the reaction becomes significant for the process, simply called the reaction temperature.

2.1 Mathematical model

The first application we investigate is the thermal conversion of oil shale into non-reactive gas. In this process, the reservoir is exposed to an external energy source such as electrical heaters or gas burners. The ISU process generally uses tightly spaced electrical heaters in boreholes to slowly and uniformly heat the formation by thermal conduction to the conversion temperature of about 350 ^0C [28]. The gas created by the decomposition of the oil shale flows into the bore hole of a producing well.

To model this application, we consider a one-dimensional oil shale reservoir (figure 2.1a). The domain is bounded by a heater bore hole on the left end and the well producer on the right end. To define the boundary conditions, we assume a constant temperature T_H around the heater. On the left end of the domain, we assume no mass flow. On the right end of the domain, the well produces at constant pressure and, due to the symmetry of the well pattern (figure 1.1), we assume no heat transfer by conduction around the producer. The top and bottom boundaries are considered impervious to both flow and heat transfer. Thus, heat loss is neglected here. This is generally a good assumption for thermal decomposition of polymer since the composite thickness is much less than its vertical length. However, this is not necessary the case for oil shale and it has been demonstrated that heat loss to overburden and underburden could have an impact on the efficiency of the process [24] depending on the ratio of formation thickness to well spacing. The wider the well spacing and the thinner the formation then the more important heat loss becomes. Here we chose to neglect them to focus on the other mechanisms of the process.

A mathematical model for this application was developed by Fan et al. [24]. The chemical reactions and the fluid and material behaviour can be described using the

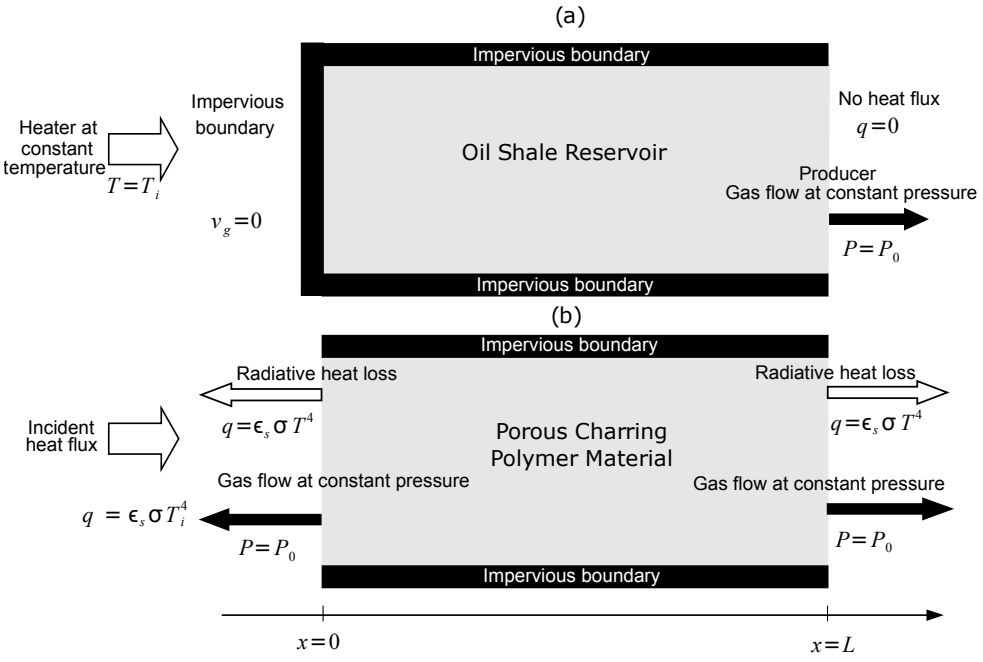

FIGURE 2.1: Model for thermal conversion of oil shale into non-reactive gas (a) and thermal decomposition of polymer composite as represented in Henderson and Wiecek experiment (b). The two models only differ in their boundary conditions.

same model as Henderson and Wiecek's thermal decomposition of polymer composite [34]. The two processes only differ in their geometry, boundary conditions and fluid and material properties. Thus it is sensible to consider the two processes in the same study as we can then validate our mathematical model with Henderson and Wiecek's experimental data.

Figure 2.1b shows Henderson and Wiecek's [34] conceptual model, where the gas can flow out of the lateral boundaries. Radiative heat flux causes the thermal decomposition and is represented by the incident heat flux on the left end of the domain. The material can exchange heat at both ends by radiation. The boundary pressure on both ends is equal to the initial pressure P_0.

For both models, the following assumptions are made:

1. The solid decomposes into a non-reactive gas with a single reaction mechanism (following [34, 46]). Further primary pyrolysis reactions do occur but for simplicity are ignored.

2. The decomposition gas behaves ideally
3. Gas flows are described by Darcy's law
4. The gas viscosity has a linear dependence on temperature
5. Porosity and permeability are linear functions of the solid fraction remaining as the reaction progresses.
6. Local thermal equilibrium (LTE) exists between the solid and the decomposition gas
7. Thermal expansion of the solid is negligible
8. Solid and gas heat capacities and thermal conductivities are constant
9. The thermal conductivities of the inert solid and the reactant solid are equal.

Assumptions 1-5 have been used previously by Kansa et al. [46] and Henderson and Wiecek [34]. Florio et al. [27] used analytical methods to study the validity of assumption 6 during the thermal decomposition of a particular glass-filled polymer composite. They found that the gas and solid phases were not always in LTE but this affected mainly the mechanical behaviour of the composite rather than the heat and mass transfer. Puiroux et al. [70] also found that the main impact was on the maximum pressure reached and hence the mechanical response of the material although they did observe a small effect on the position of the pyrolysis front. Our study is focused primarily on the scaling of heat and mass transport rather than the mechanical behaviour (hence assumption 7) so assumption 6 simplifies our analysis without significantly affecting our predictions. Assumptions 7 and 8 are discussed in the next section.

The domain is formed of an inert porous solid I. Initially, the pore-space is occupied by a solid reactant and gas. Figure 2.2 shows a conceptual representation of the pore space. The reactant R decomposes into gas G and charred solid residual C:

$$R \longrightarrow a_G G + a_C C \tag{2.1}$$

where a_G and a_C are the mass stoichiometric coefficients. The models are described by the following equations. The rate of decomposition of total reactant mass m_R follows

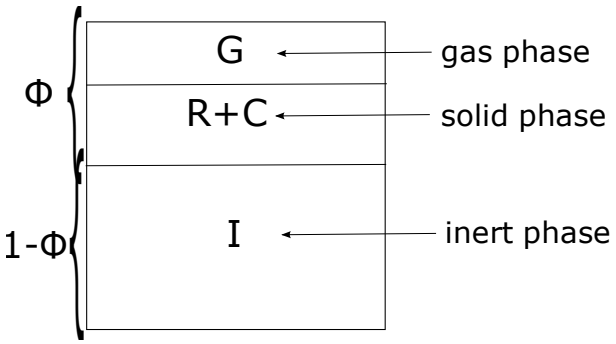

FIGURE 2.2: Conceptual representation of the pore space.

an Arrhenius law of order n:

$$\frac{1}{m_{R,0}}\frac{\partial m_R}{\partial t} = -A\left(\frac{m_R}{m_{R,0}}\right)^n \exp\left(-\frac{E_a}{RT}\right) \tag{2.2}$$

where the terms with subscript 0 are initial values. Note that we decided to use a more common formulation for the rate of decomposition [30] than Henderson and Wiecek, who used the initial mass of total solid in Equation 2.2 instead of the initial mass of reactant:

$$\frac{1}{m_{s,0}}\frac{\partial m_R}{\partial t} = -A_{HW}\left(\frac{m_R}{m_{s,0}}\right)^n \exp\left(-\frac{E_a}{RT}\right) \tag{2.3}$$

The pre-exponential factor used in Equation (2.8) is obtained from A_{HW}:

$$A = A_{HW}\left(\frac{m_{R,0}}{m_{s,0}}\right)^{n-1} \tag{2.4}$$

We define ρ_I the density of the inert solid, ρ_R the density of the solid reactant and ρ_C the density of charred residual C. The total density of the solid phase obeys the mixing law:

$$\frac{1}{\rho_s} = \frac{\omega_R}{\rho_R} + \frac{\omega_C}{\rho_C} \tag{2.5}$$

where ω_R and ω_C are the mass fraction of components R and C in phase s, respectively. Hence, the total mass of reactant can be written as:

$$m_R = \phi\omega_R\rho_s S_s V \tag{2.6}$$

where V is the volume of the domain, S_s is the saturation of solid phase. Initially, it is formed exclusively of reactant so the initial mass of solid is equal to:

$$m_{s,0} = (1-\phi)\,\rho_I V + \phi \rho_{s,0} S_{s,0} V \tag{2.7}$$

Substituting Equation 2.7 into Equation 2.2, we find:

$$\frac{\partial}{\partial t}\left(\omega_R \rho_s S_s\right) = -\frac{A}{\left(\rho_{s,0} S_{s,0}\right)^{n-1}} \left(\omega_R \rho_s S_s\right)^n \exp\left(-\frac{E_a}{RT}\right) \tag{2.8}$$

The conservation of solid residual is given by:

$$\frac{\partial}{\partial t}\left(\phi \omega_C \rho_s S_s\right) = -a_C \frac{\partial}{\partial t}\left(\phi \omega_s \rho_s S_s\right) \tag{2.9}$$

and the total mass conservation equation reads:

$$\frac{\partial \phi \rho_s S_s}{\partial t} + \frac{\partial \phi \rho_g S_g}{\partial t} = -\frac{\partial \rho_g v_g}{\partial x} \tag{2.10}$$

where S_g is the gas saturation in pores:

$$S_g = 1 - S_s \tag{2.11}$$

and v_g the gas velocity. The gas density is given by the ideal gas law:

$$\rho_g = \frac{m_{wG} P}{RT} \tag{2.12}$$

where m_{wG} is the molecular weight of the gas component.

In the initial state, a significant fraction of the pore-space is occupied by the solid phase. Hence, the permeability of the material is often quite low. As the reactant decomposes, the permeability increases significantly. Exponential [56] or power-law models [60] are often used to describe this change. In this work, we use a simple exponential relationship:

$$K = K_0 \exp\left(-\alpha\left(S_s - S_{s,0}\right)\right) \tag{2.13}$$

The velocity of the gas is given by Darcy's law:

$$v_g = -\frac{K}{\mu_g}\frac{\partial P}{\partial x} \tag{2.14}$$

The gas viscosity is assumed to have a linear dependency on temperature [27, 34] with slope $\delta\mu_g$:

$$\mu_g = \mu_{g,0} + \delta\mu_g \left(T - T_0\right) \tag{2.15}$$

Assuming LTE, the energy conservation equation is:

$$\begin{aligned}\frac{\partial}{\partial t}\left(\left(1-\phi\right)\rho_I\gamma_I + \phi\rho_s S_s h_s + \phi\rho_g S_g h_g\right) = &-\frac{\partial}{\partial x}\left(\rho_g v_g h_g\right) - \frac{\partial q}{\partial x} \\ &- \Delta h_r \frac{\partial}{\partial t}\left(\phi\omega_R\rho_s S_s\right)\end{aligned} \tag{2.16}$$

The term on the left hand side of Equation (2.16) is the rate of energy accumulation in the domain; the first term on the right represents the rate of energy transferred by convection; the second term represents the rate of energy transferred by conduction; the last term accounts for energy consumption or generation by chemical reaction. As defined here, the heat of decomposition is negative as the reaction is endothermic. The specific enthalpies h_s and h_g are defined by:

$$\begin{aligned} h_s &= \gamma_s \left(T - T_0\right) \\ \gamma_s &= \omega_R\gamma_R + \omega_C\gamma_C \end{aligned} \tag{2.17}$$

and

$$\begin{aligned} h_g &= \gamma_g \left(T - T_0\right) \\ \gamma_g &= \gamma_G \end{aligned} \tag{2.18}$$

where γ_R, γ_C and γ_G are the specific heat capacity of the reactant, charred and gas components, respectively. Equation (2.16) is modified by expanding the accumulation and convection terms and then substituting into the mass conservation equation (2.10), to give:

$$\begin{aligned}\left(\left(1-\phi\right)\rho_I\gamma_I + \phi\rho_s S_s\gamma_s + \phi\rho_g S_g\gamma_g\right)\frac{\partial T}{\partial t} = &-\rho_g v_g\gamma_g\frac{\partial T}{\partial x} - \frac{\partial q}{\partial x} \\ &- \left(\Delta h_r + a_G\left(h_s - h_g\right)\right)\frac{\partial}{\partial t}\left(\phi\omega_R\rho_s S_s\right)\end{aligned} \tag{2.19}$$

Finally, the heat flow by conduction q is modelled using Fourier's law:

$$q = -\left(\left(1-\phi\right)\kappa_s + \phi\kappa_s S_s + \phi\kappa_g S_g\right)\frac{\partial T}{\partial x} \tag{2.20}$$

In Equation 2.20, we have adopted for convenience a simple estimate of the effective thermal conductivity which depends on the volume fraction of the solid and gas in the material. This approximation has been previously used [9]. More complex expressions

would not fundamentally change the analysis. Equations (2.8), (2.10), (2.14), (2.19) and (2.20) form a set of coupled non-linear equations to be solved simultaneously for S_s, ω_R, P, T, v_g and q.

For thermal conversion of oil shale, we applied constant temperature on the left end and no heat transfer on the right end for the heat flow boundary conditions. The heating temperature T_H on the left side is equal to the temperature of the heater well bore. We assumed no heat transfer on the right end because of the symmetry of the heater pattern (figure 1.1). For the mass flow boundary conditions, we apply no mass flux on the left end (near the heater) and constant pressure P_0 on the right end (near the producer). This gives:

$$\begin{aligned} &\text{at} \quad x = 0 \quad \forall t \\ &T = T_H \qquad\qquad \text{and} \qquad v_g = 0 \\ &\text{at} \quad x = L \quad \forall t \\ &q = 0 \qquad\qquad \text{and} \qquad P = P_0 \end{aligned} \tag{2.21}$$

For the thermal decomposition of polymer composite, we apply constant heat flow with temperature dependent heat loss by radiation on the left end. The incident heat flow is defined by the effective heating temperature T_H. On the right end, we only have heat loss by radiation. For the mass flow boundary condition, we apply constant pressure P_0 on both ends. This gives:

$$\begin{aligned} &\text{at} \quad x = 0 \quad \forall t \\ &q = \epsilon_s \sigma \left(T_H^4 - T^4\right) \quad \text{or} \qquad P = P_0 \\ &\text{at} \quad x = L \quad \forall t \\ &q = -\epsilon_s \sigma T^4 \qquad\qquad \text{or} \qquad P = P_0 \end{aligned} \tag{2.22}$$

Finally, we apply the following initial conditions:

$$\begin{aligned} &S_s = S_{s,0} \\ &T = T_0 \qquad \text{at} \quad t = 0 \quad \forall x \\ &P = P_0 \end{aligned} \tag{2.23}$$

2.2 Numerical simulations

To solve the system of equations, we developed a C++ simulator called EXTEND (EXtended Thermal simulator for Evaluating new Numerical Discretization). The source code of EXTEND is provided in the CD-ROM attached to this thesis. The numerical methods used in the software are detailed in Appendix B.

We use the Finite Volume Method (FVM) with a fully implicit formulation for the discretization. The resulting discretized non-linear equations are solved using Newton's method. Initially, we use a constant dimensionless time step $\Delta t = 10^{-3}$, but different time-step strategies are discussed in Chapter 4.

For the two 1D simplified models represented in figure 2.1, we use a $50 \times 1 \times 1$ grid shown in figure 2.3. The heater well (or radiative source) is located on the left of the grid and the producer well (or constant pressure boundary surface) on the right.

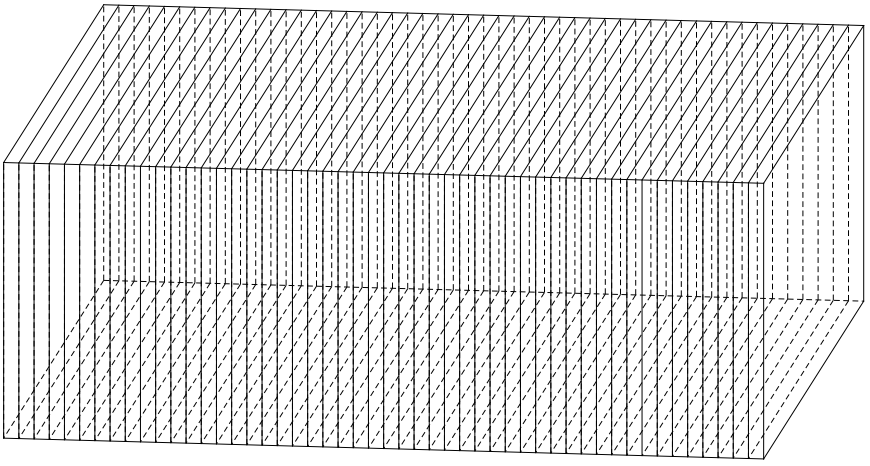

FIGURE 2.3: Finite Volume grid for the 1D simplified models represented in figure 2.1. The heater well (or radiative source) is located on the left of the grid and the producer well (or constant pressure boundary surface) on the right.

2.3 Validation using Henderson and Wiecek's experiment for thermal decomposition of polymer composite

Experimental data for the In-Situ Upgrading of heavy oil are scarce in the literature. We have knowledge of two papers that report experimental results for ISU of bitumen [49] and oil shale [24]. Unfortunately, these experiments are too complicated to be represented by such a simplified model with no liquid phase and only one reaction. In Chapter 4, our model is extended to two-phase flow with two chemical reactions and is able to describe Kumar's experiment for the ISU of bitumen [49]. For now, we note that our simple mathematical model describes both polymer degradation and ISU of oil shale, the only difference between the two systems is in the boundary conditions. Therefore, we can use experimental results for the first application to validate our model.

We first compare the model outputs with analytical solutions for the trivial cases of very short time (heat conduction and no reaction) and very long times (after pyrolysis is finished). Having obtained good agreement for these cases, we then compare its predictions with the experimental data for the thermal decomposition of a polymer composite obtained by Henderson and Wiecek [34]. Henderson and Wiecek also developed a mathematical model for one dimensional heat transfer in a polymer matrix composite during pyrolysis and performed laboratory experiments to validate their model. The material used in their experiments consisted of a basic phenolic resin and was chosen because it displays typical decomposition/expansion behaviour for glass-filled composites and is used in a large number of high-temperature thermal protection applications [27, 34]. The experimental study was conducted using a 3 cm thick slab subjected to a pure radiant heat flux. The pressure at both ends, as well as the initial pressure, was 1×10^5 Pa and the initial temperature was 297 K (24 ^oC). Two composite materials identified as H41N and MXBE-350 were studied. The gas and material properties used in their simulations were obtained after a careful literature review [34, 35, 36, 37].

In our study, we choose to neglect the thermal expansion of the solid (assumption 7). The maximum solid elongation reported by Henderson and Wiecek [34] was less than 20%. Therefore, we assume that solid expansion has little impact on the heat propagation, the solid decomposition and the gas flow. In order to further simplify the model, the thermal properties of the solid and gas (heat capacity, thermal conductivity and emissivity) are

taken as constant and so do not change with temperature and the fraction of remaining reactant (assumption 8). We note that Henderson and Wiecek [34] allowed the thermal properties to change with temperature in their study; however, we choose constant values for these thermal properties so that the solid temperature obtained in our simulations and the solid temperature reported in Henderson and Wiecek [34] are similar. The solid and gas properties, along with the initial and boundary conditions that we use in our simulation are summarized in Table 2.1.

TABLE 2.1: Summary of parameters used in our model to simulate the Henderson and Wiecek experiment [34].

Property	Material	
	H41N	MXBE-350
Length L (cm)	3.0	3.0
Porosity ϕ	0.274	0.231
Initial reactant saturation $S_{s,0}$	0.5876	0.6970
Initial permeability K (m^2)	2.6×10^{-18}	4.44×10^{-16}
Permeability function parameter α	6.4	5.7
Total solid initial density $(1-\phi)\,\rho_I + \phi\rho_{s,0}S_{s0}$ (kg/m^3)	1810	1720
Inert solid specific heat capacity γ_I $(J/(kgK))$	1500	1300
Reactant specific heat capacity γ_R $(J/(kgK))$	2200	2500
Solid thermal conductivity κ_s $(W/(mK))$	1.2	0.9
Mass decomposition m_f/m_0	0.795	0.7
Activation energy E_a $(kJ/kmol)$	2.6×10^5	2.2×10^5
Pre-exponential factor A_{HW} $(1/s)$	1.98×10^{29}, $m/m_0 \geq 0.91$	2.48×10^{44}, $m/m_0 \geq 0.96$
(see Equation 2.4)	8.17×10^{18}, $m/m_0 \leq 0.91$	8.47×10^{16}, $m/m_0 \leq 0.96$
Order of reaction n	17.33, $m/m_0 \geq 0.91$	50.64, $m/m_0 \geq 0.96$
	6.3, $m/m_0 \leq 0.91$	4.2, $m/m_0 \leq 0.96$
Heat of decomposition Δh_r (kJ/kg)	-234.0	-553.0
Gas molecular weight m_{wG} $(kg/kmol)$	18.35	18.35
Gas initial viscosity $\mu_{g,0}$ $(Pa.s)$	1.54×10^{-5}	1.54×10^{-5}
Gas viscosity derivative $\delta\mu_g$ $(Pa.s/K)$	2.5×10^{-8}	2.5×10^{-8}
Gas specific heat capacity γ_G $(J/(kgK))$	2880	2880
Gas thermal conductivity κ_g $(W/(mK))$	0.14	0.14
Initial pressure P_0 (Pa)	10^5	10^5
Initial temperature T_0 (^0C)	24	24
Emissivity ϵ	0.85	0.9
Incident heat flux $q_i = \sigma T_H^4$ (W/m^2)	2.8×10^5	2.8×10^5

Figure 2.4 compares our simulated predictions of the temperature, pressure and solid mass profiles with those obtained experimentally and numerically by Henderson and Wiecek [34] using the composite material identified as H41N. In Henderson and Wiecek's numerical simulation, the solid elongation was not neglected. Thus, the control volume widths were not constant and their spatial positions changed during the simulation. To compare the numerical results with ours, we plot the temperature evolution at different initial positions x_0 (figure 2.4a). As discussed before, the values of the heat capacity

and thermal conductivity of the solid and gas have been chosen so that the temperature profiles are similar. Nonetheless, we observe similar profiles for the dimensionless pressure and the solid mass fraction (figures 2.4b and 2.4c). The relative error between our results and the numerical results of Henderson and Wiecek is less than 5% while the relative error for the temperature between the experimental result and our results is less than 10%. We conclude that our simplified model was able to reproduce with good agreement the coupling between heat propagation, chemical reaction and gas flow for the test case and that our assumptions about the process are appropriate.

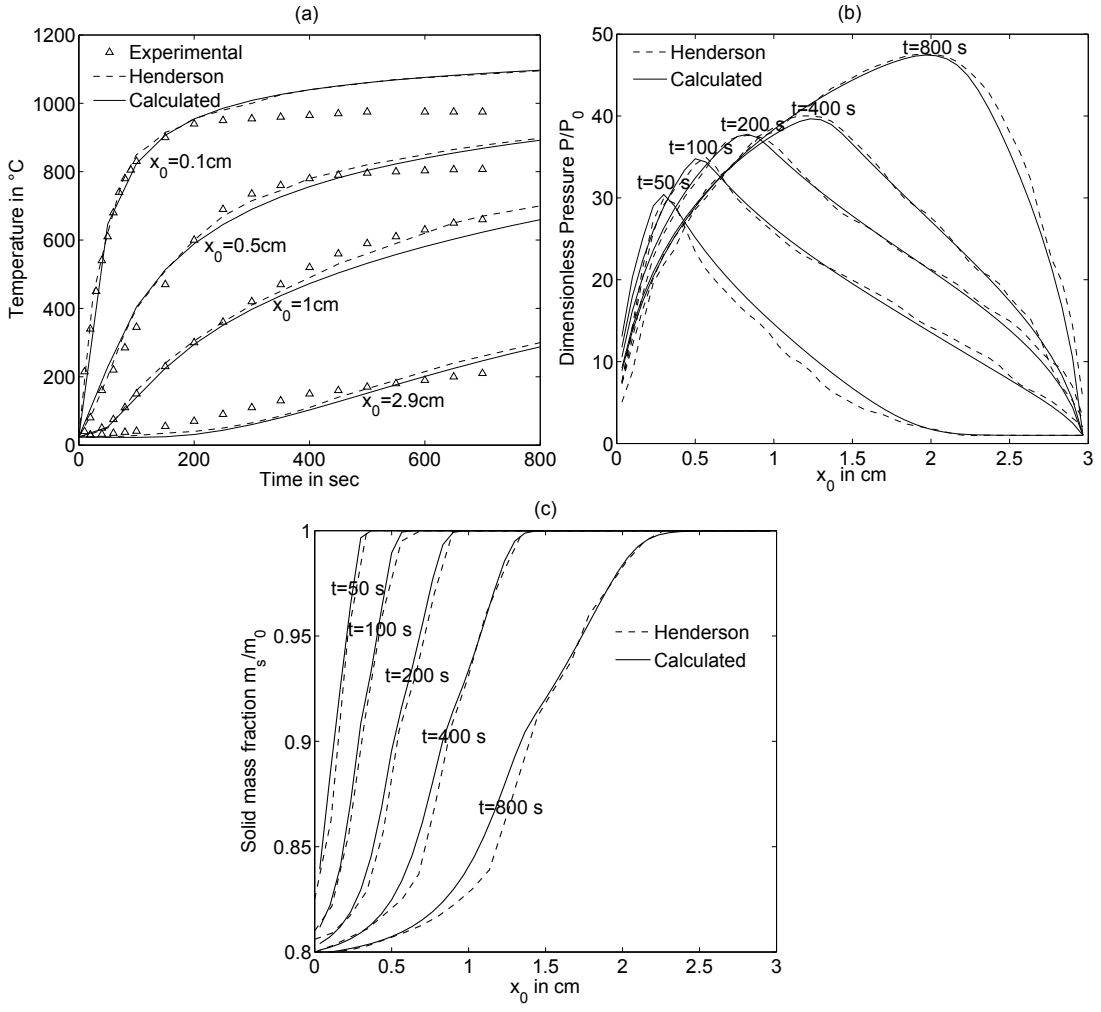

FIGURE 2.4: Figure (a) shows the temperature evolution for various initial positions, figure (b) shows pressure profile in the domain at various times and figure (c) shows the solid mass fraction profile in the domain at various times. We observe good agreement between our numerical results and Henderson and Wiecek's experimental and numerical simulation results.

2.4 Identification of dimensionless numbers by Inspectional Analysis (IA)

We used Inspectional Analysis (IA) to determine the set of dimensionless numbers that fully describe our mathematical model. IA is a well-known scaling method first described by Ruark [72]. It has previously been applied to various mathematical models including immiscible water-flooding in oil reservoirs [78], miscible displacements in heterogeneous permeable media [31] and miscible displacements in soil columns [79]. IA has not been applied to a system with the boundary conditions implemented here, where the input is not an injected velocity but a heat flux or a fixed temperature.

The procedure introduces two arbitrary scaling factors for each of the variables in the equations. These scaling factors are linear (affine) transformations from dimensional to dimensionless space. They are then grouped into dimensionless scaling groups. Finally, the values of the scaling factors are selected to minimize the number of groups. The details of the procedure are presented in Appendix A. As the IA method is based on the existing differential equations and boundary conditions, the grouping and elimination of translation factors is physically meaningful provided the equations are complete for the process we are modelling. An important step in the method is the introduction of a reference time scale τ, which is chosen here to be the time scale of the heat conduction in the inert solid:

$$\tau = \frac{(1-\phi)\,\rho_I \gamma_I L^2}{\kappa_s} \tag{2.24}$$

This implies that the dimensionless rate of heat transfer by conduction in the inert solid is set to unity at initial conditions (see Equation A.19). We made this choice as there is no natural time scale for mass flow in the systems of interest since there is zero flow initially; moreover, both the thermal degradation and the ISU problems are controlled by the rate of reaction, which in turn depends upon the temperature and thus the rate of heat transfer. It is therefore natural to compare the efficiency of these processes by comparing the time taken for heat to conduct at initial (low temperature) conditions.

By employing the method presented, we obtain a minimal form of the dimensionless groups [78]. The groups are summarized in Table 2.2 and the values of the scaling groups for Henderson and Wiecek experiment are given in Table 2.3. Since we have two sets of values for the pre-exponential factor and the order of reaction depending on the

degree of decomposition, we obtain two Damköhler numbers and two reaction orders for each material.

TABLE 2.2: Summary of scaling groups.

Name	Notation	Definition	Description
Damköhler number	D_K	$\frac{A(1-\phi)\rho_I\gamma_I L^2}{\kappa_s}$	$\frac{\text{reaction rate at } \infty \text{ temp}}{\text{heat diffusion rate}}$
Arrhenius number	N_a	$\frac{E_a}{R\Delta T}$	$\frac{\text{activation energy}}{\text{potential energy}}$
Reduced reaction enthalpy	Δh_r^*	$-\frac{\Delta h_r}{\gamma_R \Delta T}$	$\frac{\text{energy consumed}}{\text{energy stored}}$
Reduced initial temperature	T_0^*	$\frac{T_0}{\Delta T}$	$\frac{\text{initial temperature}}{\text{variation of temperature}}$
Pressure Lewis number	L_e	$\frac{\phi\mu_{g,0}\kappa_s}{K_0 P_0(1-\phi)\rho_I\gamma_I}$	$\frac{\text{heat diffusivity}}{\text{pressure diffusivity}}$
Reduced charred density	ρ_C^*	$\frac{\rho_C}{\rho_R}$	$\frac{\text{charred density}}{\text{reactant density}}$
Reduced gas density	ρ_G^*	$\frac{m_{wG}P_0}{\rho_R R T_0}$	$\frac{\text{initial gas density}}{\text{solid density}}$
Reduced reactant volumetric heat capacity	Γ_R^*	$\frac{\phi\rho_R\gamma_R}{(1-\phi)\rho_I\gamma_I}$	$\frac{\text{reactant volumetric heat capacity}}{\text{inert solid heat capacity}}$
Reduced charred specific heat capacity	γ_C^*	$\frac{\gamma_C}{\gamma_R}$	$\frac{\text{charred specific heat capacity}}{\text{reactant specific heat capacity}}$
Reduced gas specific heat capacity	γ_G^*	$\frac{\gamma_G}{\gamma_R}$	$\frac{\text{gas specific heat capacity}}{\text{reactant specific heat capacity}}$
Reduced gas viscosity variation	$\delta\mu_g^*$	$\frac{\delta\mu_g\Delta T}{\mu_{g,0}}$	$\frac{\text{maximal variation of gas viscosity}}{\text{initial gas viscosity}}$
Gas heat conductivity reduction factor	$\Delta\kappa_g^*$	$\frac{\phi\left(\kappa_g-\kappa_s\right)}{\kappa_s}$	$\frac{\text{variation of total heat conductivity}}{\text{solid heat conductivity}}$
Reduced radiative heat loss	ϵ^*	$\frac{\epsilon_s\sigma\Delta T^3 L}{\kappa_s}$	$\frac{\text{radiative heat loss}}{\text{heat flux by conduction}}$
Reaction order	n		
Gas stoichiometric coefficients	a_G		
Permeability function parameter	α		
Initial solid saturation	$S_{s,0}$		

TABLE 2.3: Values of dimensionless groups for Henderson and Wiecek's experiment.

Groups	Material	
	H41N	MXBE-350
D_{K1}	1.85×10^{21}	4.30×10^{21}
D_{K2}	2.98×10^{18}	2.81×10^{18}
N_a	26.2	22.2
T_0^*	0.25	0.25
ρ_G^*	3.2×10^{-4}	2.3×10^{-4}
ρ_C^*	1	1
γ_G^*	1.31	1.15
$\Delta\kappa_g^*$	0.24	0.19
α	6.4	5.7
a_G	1	1

Groups	Material	
	H41N	MXBE-350
n_1	17.33	50.64
n_2	6.3	4.2
Δh_r^*	0.09	0.18
L_e	9.0	0.05
Γ_R^*	0.64	1.18
γ_C^*	1	1
$\delta\mu_g^*$	1.94	1.94
ϵ^*	2.0	2.9
$S_{s,0}$	0.5876	0.6970

We applied the same analysis to the model for thermal conversion of kerogen. We considered two sets of data (Table 2.4). The first used typical values from the Green River Oil Shale Formation [24, 52, 53, 56]. The second is adapted from [93]. The corresponding dimensionless numbers are reported in Table 2.5.

TABLE 2.4: Summary of parameters for thermal conversion of kerogen (test cases 1 and 2).

Property	Test case 1	Test case 2
Length L (m)	15.0	10.0
Porosity ϕ	0.2	0.1
Initial reactant saturation $S_{s,0}$	0.85	0.9
Initial Permeability K (mD)	2	7
Permeability function parameter α	6.28	7.6
Inert solid density ρ_I (kg/m^3)	2000	2200
Kerogen density ρ_R (kg/m^3)	1200	1200
Charred density ρ_C (kg/m^3)	1380	1200
Inert solid specific heat capacity γ_I $(J/(kgK))$	915	1335
Reactant solid specific heat capacity γ_R $(J/(kgK))$	1000	1335
Charred specific heat capacity γ_C $(kJ/(kgK))$	1000	1335
Solid thermal conductivity κ_s $(W/(mK))$	2.0	1.2
Activation energy E_a $(kJ/kmol)$	1.62×10^5	2.26×10^5
Pre-exponential factor A $(1/s)$	4.33×10^7	3.0×10^{13}
Order of reaction n	1	1
Charred residual stoichiometric coefficient a_C	0.466	0.555
Heat of decomposition Δh_r (kJ/kg)	0.0	-50.0
Gas molecular weight m_{wG} $(kg/kmol)$	30	44.1
Gas initial viscosity $\mu_{g,0}$ $(Pa.s)$	1.94×10^{-5}	0.79×10^{-5}
Gas viscosity derivative $\delta\mu_g$ $(Pa.s/K)$	2.7×10^{-8}	1.2×10^{-8}
Gas specific heat capacity γ_G $(J/(kgK))$	2000	2500
Initial pressure P_0 (MPa)	0.69	10
Initial temperature T_0 $(^K)$	289.85	313.15
Heater temperature T_H (KC)	623.15	573.15

TABLE 2.5: Value of dimensionless groups for thermal conversion of kerogen (Test cases 1 and 2).

Groups	Test case 1	Test case 2
D_K	7.1×10^{15}	6.6×10^{21}
N_a	58	104
T_0^*	0.87	1.2
ρ_G^*	7.2×10^{-3}	0.14
ρ_C^*	1.15	1
γ_G^*	2	1.9
$\Delta\kappa_g^*$	0.0	0.0
α	6.28	7.6
a_G	0.534	0.455

Groups	Test case 1	Test case 2
n	1	1
Δh_r^*	0.0	0.14
L_e	3.9×10^{-3}	5.2×10^{-6}
Γ_R^*	0.16	0.06
γ_C^*	1.0	1.0
$\delta\mu_g^*$	0.46	0.39
ϵ^*	0.0	0.0
$S_{s,0}$	0.85	0.9

The Lewis number obtained through our analysis is actually a pressure Lewis number. It represents the ratio of thermal diffusivity D_T and pressure diffusivity D_P [83].

$$L_e = \frac{D_T}{D_P} = \frac{\phi\mu_{g,0}\kappa_s}{K_0 P_0 (1-\phi)\rho_I\gamma_I} \tag{2.25}$$

The Lewis number can be used to calculate a Péclet heat transfer number [43] which is defined here as:

$$P_e = \frac{\rho_g v_g \gamma_g L}{\kappa_s} \tag{2.26}$$

and describes the ratio of heat driven by convection to thermal diffusion. As no fluid is injected, the fluid velocity is generated by the pressure gradients induced by heating. Hence, the Péclet number is local and varies with the dimensionless pressure and temperature:

$$P_e = \frac{\rho_g^* \Gamma_R^* \gamma_G^*}{L_e} \rho_{gD} v_{gD} \gamma_{gD} \tag{2.27}$$

The Damköhler number characterises the ratio of the reaction rate and the heat diffusion rate at infinite temperature. The Damköhler number we define here is a variation of Damköhler's second number, representing the ratio of the reaction rate and the diffusion rate [43]. Because of the Arrhenius law, the chemical reaction constant is defined by D_K, the Arrhenius number N_a and the initial temperature T_0^*. The Arrhenius number represents an energy barrier to the chemical reaction.

2.5 Calculation of Reaction Temperature

The Arrhenius number quantifies the impact of temperature on the chemical reaction rate but there is no obvious way of determining how hot the system needs to be before the reaction becomes important. The temperature at which the reaction appears will depend upon the time scale considered. This is a natural consequence of the exponential nature of the Arrhenius law (Equation 2.8). Nonetheless it would be very useful to know what this "reaction temperature" is for any given system.

One useful consequence of the choice of reference time scale for our dimensionless analysis is the possibility to define this "reaction temperature". We chose the time scale for thermal diffusion in the inert solid to be our reference time scale (Equation 2.24). The dimensionless reaction rate can be defined in terms of the Damköhler number, the Arrhenius number and the reduced initial temperature as

$$D_K \exp\left(-N_a \left(\frac{1}{T_D + T_0^*}\right)\right) = \frac{\text{time scale thermal diffusion}}{\text{time scale chemical reaction}} \tag{2.28}$$

where the dimensionless temperature T_D is defined as:

$$\begin{aligned} T_D &= \frac{T}{\Delta T} \\ \Delta T &= T_H - T_0 \end{aligned} \tag{2.29}$$

The Damköhler number represents the dimensionless reaction rate at infinite temperature and the exponential term represents an energy barrier to the reaction. This energy barrier is associated with a barrier or threshold temperature defined as:

$$T_B = \frac{E_a}{R} = N_a \Delta T \tag{2.30}$$

Thus the dimensionless reaction rate at the initial temperature T_0 is defined by the Damköhler number and the ratio of the threshold temperature to the initial temperature:

$$\frac{T_B}{T_0} = \frac{N_a}{T_0^*} \tag{2.31}$$

Similarly the dimensionless reaction rate at the heater temperature T_H is defined by the Damköhler number (discussed above) and the ratio of the threshold temperature to the heater temperature:

$$\frac{T_B}{T_H} = \frac{N_a}{1 + T_0^*} \tag{2.32}$$

As noted in our discussion of dimensionless time, for both of the applications examined here we are interested in evaluating how the reaction rate increases when the system is heated, because the reaction rate is insignificant at initial conditions. As the temperature increases in the domain, the reaction rate increases. The time scale of the chemical reaction and heat diffusion are equivalent when the chemical reaction becomes significant:

$$D_K \exp\left(-\frac{N_a}{T_D + T_0^*}\right) = 1 \tag{2.33}$$

We can therefore calculate a reaction temperature from the Arrhenius and Damköhler numbers as

$$T_{R1} = \Delta T \frac{Na}{\log D_K} \tag{2.34}$$

Applying this to Henderson and Wiecek's experiment for the composite material denoted H41N , we obtain a reaction temperature $T_{R1} = 638.15\ K$ ($365\ ^oC$). Figure 2.5a shows the solid mass profile for Henderson and Wiecek's experiment at different times.

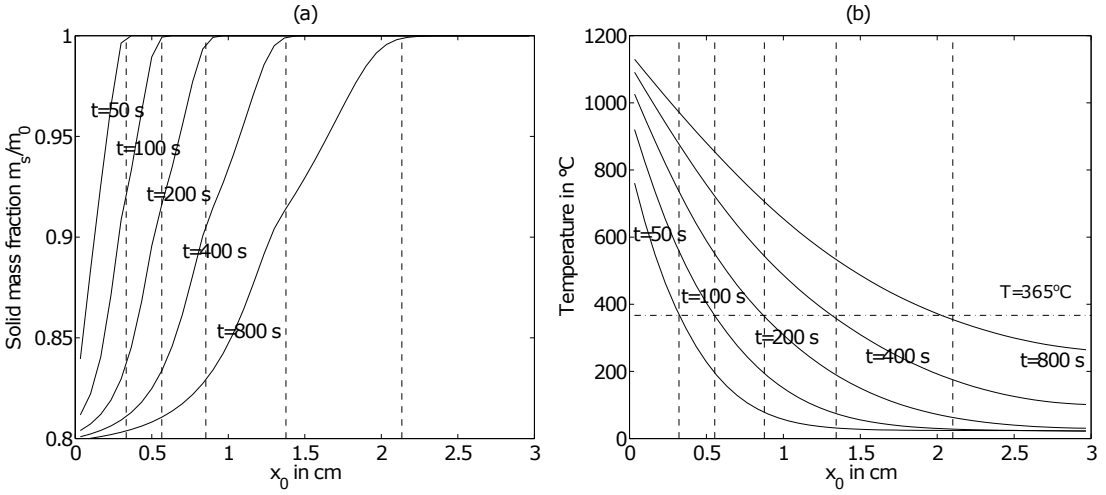

FIGURE 2.5: Comparison of reaction temperatures predicted by Equation 2.34 and obtained by numerical simulation for Henderson and Wiecek's experiment. Figure (a) shows in plain line the solid mass fraction profile at various times and in dashed line the position where the reaction appears. This position is then reported on (b) which shows the temperature profile at various times and compares the results with the predicted temperature $T_{R1} = 638.15\ K\ (365^oC)$. We observe good agreement between Equation 2.34 and the numerical result.

The dashed lines indicate the position at which the reaction appears. We report these positions on the temperature profiles (Figure 2.5b). Thus, the intersection between the dashed lines and the temperature profiles shows the temperature at the position where the chemical reaction appears. We observe that there is very good agreement between the reaction temperature calculated (Equation 2.34) and the one observed, especially near the heat source. The solid mass fraction starts decreasing significantly when the temperature reaches T_{R1}, for which the chemical reaction and heat diffusion have the same rate. This validates the choice of the time scale of the heat conduction in the inert solid as a reference time scale for the process.

Therefore, an important dimensionless quantity describing the process is the ratio of chemical rate to heat conduction rate at the heater temperature, defined as the extended Damköhler number:

$$\tilde{D_K} = D_K \exp\left(-\frac{N_a}{1+T_0^*}\right) = \frac{A\,(1-\phi)\,\rho_I \gamma_I L^2}{\kappa_s} \exp\left(-\frac{E_a}{RT_H}\right) \tag{2.35}$$

In other words, it represents the maximum possible chemical reaction rate in the domain. When $\tilde{D_K} < 1$, one has $T_H < T_{R1}$ and the temperature in the reservoir never reaches the reaction temperature defined previously. In this case, the chemical reactions are

slow and the process is not very efficient. Thus, the extended Damköhler number could be used as a simple measure of performance for the process.

2.6 Summary

In this chapter, we developed a simplified model where a solid reactant decomposes into non-reactive gas. This model enabled us to draw a parallel between ISU and thermal decomposition of polymer composite when used as heat-shielding for spacecraft re-entry. We validated our numerical model by comparison with experimental result obtained by Henderson and Wiecek [34], where a thin slab formed of polymer composite material was subjected to a pure radiant heat flux. Our simplified model was able to reproduce with good agreement the coupling between heat propagation, chemical reaction and gas flow for this test case.

We then used Inspectional Analysis to determine the minimum number of dimensionless groups that can be used to describe both processes. To define these numbers, we chose the time scale of the heat conduction in the inert solid as a reference time scale for the process. We showed that the processes can be described by seventeen dimensionless groups. We then computed the values of this groups for the two test cases described in Henderson and Wiecek's experiment [34] and for two test cases describing thermal conversion of kerogen [24, 93].

Finally, we showed that the dimensionless chemical rate at any temperature can be calculated with the Damköhler number D_K, which describes the ratio of chemical reaction rate to heat conduction rate at infinite temperature, and the Arrhenius number N_a, which quantifies the ratio of activation energy of the reaction to potential energy. We observed that the chemical reaction became significant at T_{R1}, the temperature for which this dimensionless chemical rate was equal to 1. This validated the choice of the time scale of heat conduction in the inert solid as a reference time scale for the process.

This analysis allowed us to identify a new dimensionless number, called the extended Damköhler number $\tilde{D_K}$ which is a combination of D_K and N_a and quantifies the chemical reaction rate at heater temperature. When $\tilde{D_K} < 1$, the temperature in the reservoir never reached T_{R1}. In this case the chemical reaction was always slow compared to the

heat conduction and the process was not very efficient. Therefore, $\tilde{D_K}$ could be used as a simple measure of performance of the process.

However, since the model is extremely non-linear, we need to perform a sensitivity analysis to study the process in more detail. In the next chapter, we use Design of Experiment (DOE) to perform such an analysis.

Chapter 3

Sensitivity analysis using Design of Experiment (DOE)

Some of the mechanisms that are involved in the model described in the previous chapter can be influenced by several dimensionless groups. For example, the chemical reaction rate is quantified by the Damköhler number, the Arrhenius number and the reduced initial temperature. Moreover, one dimensionless number can impact several physical mechanisms. For example, the reduced initial temperature influences the chemical reaction and the radiative part of the boundary conditions, and the reduced gas specific heat capacity impacts heat accumulation in the fluid and heat flow by convection. It is therefore challenging to identify which dimensionless groups have a large impact on the process applications using trial and error methods. Instead, a Design of Experiment (DOE) technique can be used to identify primary factors in an efficient manner.

The main objective of this chapter is to identify the primary dimensionless numbers for the performance of the two processes described in Chapter 2: the thermal conversion of kerogen into non-reactive gas and the thermal decomposition of polymer composite when used as heat-shielding for spacecraft re-entry and for rocket nozzle protection. We used DOE to investigate the sensitivity of the two processes to the different dimensionless numbers for different measure of performance in order to determine which ones are the key dimensionless numbers in each case. We first describe a procedure which combines the use of a two-level factorial design with a response surface methodology. We then apply the procedure to the thermal conversion of kerogen. We define two measures of

performance: the Energy Return On Investment (EROI) of the process, and the mechanical stress in the domain. This study is then used to identify an optimal heater temperature, which can be defined using dimensionless numbers. We apply the same procedure to the thermal decomposition of polymer composite. We choose the dimensionless right-end temperature as a measure of performance for this process. This allows us to predict the protection time of the material.

3.1 Two-level factorial design

Factorial designs are widely used in experiments involving a large number of factors [64]. This class of design is characterized by the fact that the effect of changing one variable can be assessed independently of the others. The factorial experiment where all combinations of the levels of the factors are run is referred to as a full factorial design. A two-level factorial design is a design where each of the k factors of interest has only two levels (denoted as "-1" and "1"). For two levels, the full factorial design has exactly 2^k experimental trials or runs. The full factorial experiment with three factors is represented in figure 3.1.

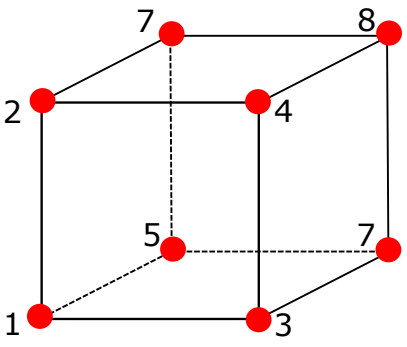

Trial	Factor levels A	B	C
1	-1	-1	-1
2	1	-1	-1
3	-1	1	-1
4	1	1	-1
5	-1	-1	1
6	1	-1	1
7	-1	1	1
8	1	1	1

FIGURE 3.1: Three-factor two-level full factorial design

For experiments in which a large number of factors are being considered, a two-level full-factorial design would result in an extremely large number of combinations to test. In this case, a fractional factorial design where a carefully selected subset of the full design is used can be applied. It can be generated from the full factorial design by choosing an alias structure. The alias structure determines which effects are confounded with each other. For example, for an experiment with three factors A, B and C, a 2^2 fractional design can be generated by considering a full two factor experiment involving A and B

and confounding the factor C with the two-factor interaction $C = A * B$. This design is represented in figure 3.2.

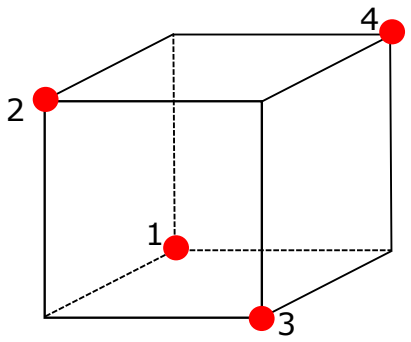

Factor levels

Trial	A	B	C
1	-1	-1	1
2	1	-1	-1
3	-1	1	-1
4	1	1	1

FIGURE 3.2: 2^2 fractional factorial design with three factors. This design is of resolution III, since C and AB are confounded.

The resolution of a design describes how much the effects in a fractional factorial experiment are aliased with other effects. A design is of resolution R if no p-factor effect $(0 < p < R)$ is aliased with another effect containing less than $R - p$ factors. For example, the design represented in figure 3.2 is of resolution III, since C and AB are confounded. Resolution III, IV, and V designs are most common:

- Resolution III: No main effects are aliased with any other main effect, but main effects are aliased with 2-factor interactions.
- Resolution IV: No main effects are aliased with any other main effect or 2-factor interactions, but some 2-factor interactions are aliased with other 2-factor interactions and main effects are aliased with 3-factor interactions.
- Resolution V: No main effects or 2-factor interactions are aliased with any other main effect or 2-factor interactions, but 2-factor interactions are aliased with 3-factor interactions and main effects are aliased with 4-factor interactions.

In this study, we will use fractional factorial designs of resolution V so that main and interaction effects can be quantified without aliasing between each other. Algorithms to generate a design of resolution V are described in Myers et al. [65]. The results of the sensitivity analysis depend only on the resolution of the design and not on the choice of the generators. Figure 3.3 shows the available factorial design resolutions for various number of factors and number of runs.

	Factors													
Run	2	3	4	5	6	7	8	9	10	11	12	13	14	15
4	Full	III												
8		Full	IV	III	III	III								
16			Full	V	IV	IV	IV	III	III	III	III	III	III	III
32				Full	VI	IV	IV	IV	IV	IV	IV	IV	IV	IV
64					Full	VII	V	IV	IV	IV	IV	IV	IV	IV
128						Full	VIII	VI	V	V	IV	IV	IV	IV
256							Full	IX	VIII	VI	VI	V	V	V

FIGURE 3.3: Available factorial design resolutions for various numbers of factors and numbers of runs.

The results of a factorial experiment can be analysed using a tool called response surface methodology, in which a model or "surface" is fitted to the experimental results.

3.2 Response surface methodology

Response Surface Methodology (RSM) was introduced by Box and Wilson [11] to study the relationship between the response of an experiment and its independent variables. Hill and Hunter [39] studied the applications of RSM in different processing areas. The evolution of RSM in experimental design has been reviewed by Myers et al. [65].

Fundamentally, the response surface problem centres around a response y which is a function of k independent variables x_1, x_2,... x_k, that is:

$$y = f(x_1, x_2, ..., x_k) \tag{3.1}$$

The form of the function f is unknown but it is assumed that it can be approximated by a polynomial function of low order, for example a first-order model:

$$y = \beta_0 + \sum \beta_j x_j + \epsilon \tag{3.2}$$

or a first-order model with interaction

$$y = \beta_0 + \sum \beta_j x_j + \sum_{i,j,i \neq j} \beta_{ij} x_i x_j + \epsilon \tag{3.3}$$

Here, the coefficients β are constant. The β_i terms are called main factor effects and the β_{ij} terms the two-factors interaction effects. The error of the model is denoted as ϵ. We define p as the number of factors taken into account in the model ($p = k$ for first-order, $p = k(k+1)/2$ for first-order with interaction). Higher order models, for example a second-order model

$$y = \beta_0 + \sum \beta_j x_j + \sum_{i,j,i \neq j} \beta_{ij} x_i x_j + \sum_j \beta_{jj} x_j^2 + \epsilon \tag{3.4}$$

can be applied but the estimation of the various effects β is only possible with higher level factorial designs (for example three level for order 2). They are computed using the least squares method.

3.2.1 Least squares estimator

Suppose that the function f in equation 3.1 is approximated by a first-order model (equation 3.2). Suppose that n experimental runs are taken on various combinations of the parameters x_1, x_2,... x_k, $n > k$. For example, for a two-level full factorial design, $n = 2^k$. Then, if we defined y_1, y_2,... y_n as the results of the n experimental runs, the model can be written as:

$$y_j = \beta_0 + \sum \beta_j x_{ji} + \epsilon_j \tag{3.5}$$

where x_{ji} is the value of the parameter j for the run i. It is assumed that ϵ_j are independent from run to run with zero mean and a variance σ^2. The model can be written in the form:

$$y = X\beta + \epsilon \tag{3.6}$$

where:

$$y = \begin{bmatrix} y_1 \\ y_2 \\ \vdots \\ y_n \end{bmatrix}, \quad \beta = \begin{bmatrix} \beta_1 \\ \beta_2 \\ \vdots \\ \beta_n \end{bmatrix} \quad \text{and} \quad X = \begin{bmatrix} 1 & x_{11} & x_{21} & \dots & x_{k1} \\ 1 & x_{12} & x_{22} & \dots & x_{k2} \\ \vdots & \vdots & \vdots & \vdots & \vdots \\ 1 & x_{1n} & x_{2n} & \dots & x_{kn} \end{bmatrix} \tag{3.7}$$

For a first-order model with interactions, the matrix X is given by:

$$X = \begin{bmatrix} 1 & x_{11} & x_{21} & \dots & x_{k1} & x_{11}x_{21} & \dots \\ 1 & x_{12} & x_{22} & \dots & x_{k2} & x_{12}x_{22} & \dots \\ \vdots & \vdots & \vdots & \vdots & \vdots & \vdots & \vdots \\ 1 & x_{1n} & x_{2n} & \dots & x_{kn} & x_{1n}x_{2n} & \dots \end{bmatrix} \tag{3.8}$$

We use the method of least squares [65] as an estimation procedure for the coefficient β. This method gives a vector $\hat{\beta}$ which results in a minimum value for the sum of squares of the errors:

$$SS_E = \sum_{i=1}^{n} \epsilon_i^2 \tag{3.9}$$

Assuming that $X'X$ is non-singular (rank= p), we have the following least squares estimator:

$$\hat{\beta} = \left(X'X\right)^{-1} X'y \tag{3.10}$$

Then, the sum of squares of the errors can be simplified as:

$$\begin{aligned} SS_E &= \left(y - X\hat{\beta}\right)' \left(y - X\hat{\beta}\right) \\ &= y'y - 2\hat{\beta}X'y + \hat{\beta}'X'X\hat{\beta} \\ &= y'y - \hat{\beta}X'y \end{aligned} \tag{3.11}$$

and the sum of squares of the regression model SS_R can be obtained from the estimators as:

$$\begin{aligned} SS_R &= \left(X\hat{\beta}\right)' \left(X\hat{\beta}\right) \\ &= \hat{\beta}'X'X \left(X'X\right)^{-1} X'y \\ &= \hat{\beta}'X'y \end{aligned} \tag{3.12}$$

The regression model has p degrees of freedom and the error $n - p$. The mean square of the regression model and error are defined by:

$$MS_R = \frac{SS_R}{p}, \quad MS_E = \frac{SS_E}{n-p} \tag{3.13}$$

It can be shown [65] that:

$$E\left[SS_E\right] = \sigma^2(n-p) \tag{3.14}$$

Therefore, MS_E is an unbiased estimator of σ^2. Table 3.1 summarizes these results.

TABLE 3.1: Sum of squares and degrees of freedom for regression model and error

Source	Sum of squares	Degree of freedom	Mean square
regression	$\hat{\beta}'X'y$	p	$\hat{\beta}'X'y/p$
error	$y'y - \hat{\beta}'X'y$	$n-p$	$\left(y'y - \hat{\beta}'X'y\right)/(n-p)$
total	$y'y$	n	

We also observe that $E\left(\hat{\beta}\right)$, the expectation of $\hat{\beta}$, is equal to β. Indeed, equation 3.10 implies:

$$\begin{aligned} E\left(\hat{\beta}\right) &= E\left[\left(X'X\right)X'\left(X\beta+\epsilon\right)\right] \\ &= \beta + E\left[\left(X'X\right)X'\epsilon\right] \end{aligned} \tag{3.15}$$

Since $E(\epsilon) = 0$,

$$E\left[\left(X'X\right)X'\epsilon\right] = 0 \tag{3.16}$$

and hence the desired result. Then, $\hat{\beta}$ is an unbiased estimator of β. Moreover, the variance-covariance of $\hat{\beta}$ is given by:

$$\begin{aligned} \operatorname{cov}\left(\hat{\beta}\right) &= E\left[\hat{\beta}-\beta\right]\left[\hat{\beta}-\beta\right]' \\ &= E\left[\left(X'X\right)^{-1}X'y-\beta\right]\left[\left(X'X\right)^{-1}X'y-\beta\right]' \\ &= E\left[\left(X'X\right)^{-1}X'\left(y-X\beta\right)\right]\left[\left(X'X\right)^{-1}X'\left(y-X\beta\right)\right]' \\ &= \left[\left(X'X\right)^{-1}X'\right]E\left[y-X\beta\right]\left[y-X\beta\right]'\left[\left(X'X\right)^{-1}X'\right]' \\ &= \left[\left(X'X\right)^{-1}X'\right]\operatorname{cov}(\epsilon)\left[\left(X'X\right)^{-1}X'\right]' \\ &= \sigma^2\left[\left(X'X\right)^{-1}X'\right]\left[\left(X'X\right)^{-1}X'\right]' \\ &= \sigma^2\left(X'X\right)^{-1} \end{aligned} \tag{3.17}$$

This implies that the variances of the estimators $\hat{\beta}$ are given by the diagonal elements of $(X'X)^{-1}$, each multiplied by σ^2, the variance of y. These results are essential for response surface methodology with DOE, where the estimators β are compared with the variance of y.

3.2.2 Normal probability plot and Pareto chart

In the previous section, we assumed that the true error ϵ is normally distributed with a mean of zero and a variance of σ^2. Therefore, effects that follow a normal distribution

with 0 mean and $\sigma^2/2^k$ variance are not representative of the model because they cannot be distinguished from random variability. On a normal probability plot, where the value of the effect are plotted against the cumulative probability of the normal distribution, these effects are expected to fall near a fitted line, with intercept 0 and slope $\sigma/\sqrt{2^k}$, called the near-zero line. Effect coefficients that show large deviations from the distribution will be significant since they do not come from this normal distribution. Figure 3.5 and 3.7 give examples of a half-normal plot, where the effects are converted to absolute values and plotted on the positive half of the normal curve.

Significant effects can also be identified by comparing individual effect values to a threshold value using the Pareto chart, which is useful for showing the relative size of effects. It is plotted with the t-values of the effects, which are computed by simply dividing the numerical effect by the associated standard error, which is obtained using the diagonal element of the variance-covariance matrix (equation 3.17). For a two-level factorial experiment, the t-value of an effect is given by:

$$t\text{-value} = \frac{\text{Effect}}{\sqrt{MS_E\left(\frac{1}{n^+} + \frac{1}{n^-}\right)}} \tag{3.18}$$

where "n^+" is the number of trials with a value of "1" for the effect and "n^-" the number of trials with a value of "-1". For the threshold value, Lenth [55] uses the critical value $t_{\nu,d}$ of a student t-distribution with d degrees of freedom and a confidence limit $1-\nu$. Student distributions are generally used when estimating confidence intervals for normally distributed statistics where the standard deviation is unknown [65]. The t-distribution is similar to the normal distribution. Both of these distributions are symmetric and centred on zero. However, the t-distribution has higher probability in the tails. As the degrees of freedom d approach infinity, the t-distribution approaches the standard normal distribution. Figure 3.4 shows the t-distribution for $d = 5$, 25 and 50.

The threshold defined by Lenth [55] is referred to as Lenth's limit, or l-limit. For a confidence of 95%, we obtain:

$$l\text{-limit} = t_{0.05,d} \tag{3.19}$$

A more conservative approach takes the number of estimated effects into account by dividing it into the desired probability for the risk value ν [2]. We refer to this as the

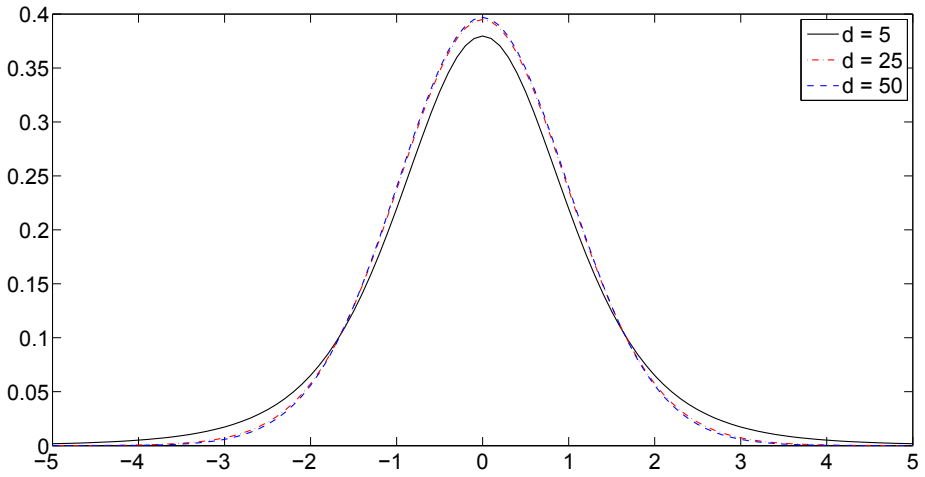

FIGURE 3.4: t-distribution for various degrees of freedom d. As d approaches infinity, the t-distribution approaches the standard normal distribution

Bonferroni (its inventor) corrected t-limit, or simply the t-limit:

$$t\text{-limit} = t_{0.05/k,d} \tag{3.20}$$

Examples of Pareto charts are given in figures 3.6 and 3.8. This analysis allows us to classify the dimensionless numbers into three categories:

- the primary numbers: these are the numbers which have their main effect or at least one of their interaction effects greater than the t-limit.
- the secondary numbers: these are the numbers which have no main effect or any interaction effect greater than the t-limit but their main effect or at least one of their interaction effects is greater than the l-limit.
- the insignificant numbers: these are the numbers which have no main effect or interaction effect greater than the l-limit.

The response can now be analysed as a function of the primary numbers. A better approximation can be obtained in a more detailed study with both the primary and secondary numbers. Next, this method is successively applied to the thermal conversion of kerogen and the thermal protection system using polymer composite with various measures of performance.

3.3 Application to the performance of thermal conversion of kerogen

As shown in Chapter 2, the thermal conversion of kerogen by electrical heating (Figure 2.1a) can be represented by the seventeen dimensionless groups defined in Table 2.2. However, for this particular process, there is no incident heat flux and no heat loss by radiation ($\epsilon^* = 0$). Moreover, we assume for consistency with previous work that the order of the decomposition reaction is always one and we consider the thermal conductivity of the domain as constant ($\Delta\kappa_g^* = 0$) [12, 24, 30, 52]. Thus, our model of thermal conversion of kerogen depends upon fourteen dimensionless groups. Minimum and maximum values for each dimensionless number are obtained by combining minimum and maximal values for each dimensional parameter. Table 3.2 gives the range for each parameter used in this study. They have been selected from a careful literature review. For the rock and initial properties, we used papers describing numerical simulation of ISU of oil shale [24, 52, 93]. For the chemical reaction properties, we reviewed Braun et al. [12] and Phillips et al. [67]. Finally, we used Perry's Handbook [66] for the thermodynamic properties of the components.

TABLE 3.2: Range of values for the various dimensional parameters of the thermal conversion of kerogen.

Property	min	max	Property	min	max
L (m)	10	15	ϕ	0.1	0.3
K_0 (mD)	1	10	α	5	10
ρ_I (kg/m^3)	2000	2200	γ_I $(J/(kgK))$	900	1500
κ_s $(W/(mK))$	1	3	S_{s0}	0.8	0.9
ρ_R (kg/m^3)	1000	1500	γ_R $(J/(kgK))$	1000	1500
ρ_C (kg/m^3)	1000	1500	γ_C $(J/(kgK))$	1000	1500
A (s^{-1})	4×10^7	3×10^{13}	E_a(J/mol)	1.60×10^5	2.3×10^5
Δh_r (J/kg)	-1×10^5	0	a_G	0.4	0.6
m_{wG} (kg/mol)	0.03	0.044	γ_G $(J/(kgK))$	2000	2500
μ_g $(Pa.s)$	0.75×10^{-5}	2×10^{-5}	$\delta\mu_g$ $(Pa.s/K)$	10^{-8}	3×10^{-8}
T_H (^0C)	300	400	T_0 (^0C)	10	40
P_0 (Pa)	5×10^5	1×10^7			

In reality, data for properties such as molecular mass, heat capacity and viscosity of the gas or activation energy and pre-exponential factor are not independent, but here they are assumed to be for the purpose of the sensitivity analysis. Dependencies between parameters should be explored in future work as this may reduce the set of primary

numbers obtained from the analysis. Assuming they are independent, we obtain a range for our fourteen dimensionless groups (Table 3.3).

TABLE 3.3: Range of values obtained for the various scaling groups obtained for thermal conversion of kerogen. We observe that several numbers, such as D_K and L_e, vary over a large range, whereas other numbers, such as T_0^* vary over a much smaller range.

Groups	min	max	Groups	min	max
D_K	1.7×10^{15}	2×10^{22}	N_a	49.3	106.4
T_0^*	0.73	1.2	Δh_r^*	0.0	0.38
L_e	$2.6. \times 10^{-6}$	0.029	ρ_G^*	3.8×10^{-3}	0.19
ρ_C^*	0.67	1.5	Γ_R^*	0.04	0.54
γ_C^*	0.67	1.5	γ_G^*	1.33	2.5
$\delta\mu_g^*$	0.13	1.56	α	5	10
S_{s0}	0.8	0.9	a_G	0.4	0.6

3.3.1 Study of EROI

In reservoir engineering, the performance of heavy oil recovery processes are generally measured by the EROI ratio, which is defined by the ratio of the energy content of the produced hydrocarbons and the energy supplied to the reservoir. If we define E_c as the energy content of 1 kg of gas, the recovered energy E_R is given by:

$$E_R = f \times m_G \times E_c \tag{3.21}$$

where $m_G = a_G m_{R,0}$ is the mass of gas generated by reactant decomposition and f is the fraction of gas recovered. The invested energy E_I is equal to the sum of the energy used to heat up the system plus the energy consumed by the decomposition. We approximate it by:

$$E_I = (1-\phi)\,\rho_I \gamma_I V \Delta T + \gamma_R m_{R,0} \Delta T - \left(\Delta h_r + \left(\gamma_R - a_G\gamma_G - a_C\gamma_C\right)\Delta T\right) m_{R,0} \tag{3.22}$$

We express the EROI ratio in terms of our dimensionless groups and variables using Inspectional Analysis (see Appendix A). This gives:

$$\text{EROI} = f \frac{a_G S_{s,0} \Gamma_R^* E_c^*}{1 + \left(a_G\gamma_G^* + a_c\gamma_C^* - \Delta h_r^*\right)\Gamma_R^* S_{s,0}} \tag{3.23}$$

where E_c^* is the reduced energy content of the gas:

$$E_c^* = \frac{E_c}{\gamma_R \Delta T} \tag{3.24}$$

Note that our definition of EROI only takes into account the energy invested in the recovery process, deliberately omitting the energy spend in the transport and additional refining of the product. Also, the heater efficiency can have a large impact on the overall EROI of the production processs.

Equation 3.23 shows that the EROI can be expressed as the product of the fraction of recovered gas f and a well-defined function of the dimensionless groups a_G, a_C $S_{s,0}$, Γ_R^*, γ_G^*, γ_C^*, Δh_r^* and E_c^*. The fraction of recovered gas depends on the 14 dimensionless numbers present in Table 3.3 and on the production time.

In order to produce all the kerogen in the shortest time possible, the domain has to be brought to a high temperature, generally close to the heater temperature. The analytical solution for the temperature of a sealed system heated by a source at a constant temperature shows that the heater will take approximately twice the time scale of the heat conduction in the domain τ (Equation 2.24) to provide 90% of the heat energy needed to completely heat the domain at the heater temperature. Therefore, we consider a production time:

$$t_{\text{prod}} = 2 \times \tau \tag{3.25}$$

Some of the dimensionless numbers can have a large impact on f while others will have an insignificant impact. A priori, D_K should have a large impact as it described the rate of chemical reaction while the impact of $\delta\mu_g^*$ should be small since the flow is monophasic. In order to verify these assumptions and identify which are the most important parameters for the energy efficiency of the process, we use DOE with f as a measure of performance.

We use a two-level fractional factorial design of resolution V (section 3.1) and a first-order model with interaction. The response f for the corresponding values of the dimensionless numbers (Table 3.3) is obtained by numerical simulation, using the method described in Chapter 2 (section 2.2) and detailed in Appendix B. In particular, we use a constant dimensionless time-step $\Delta t = 10^{-3}$ and a $50 \times 1 \times 1$ grid (figure 2.3).

Figure 3.5 shows the half-normal plot of effects. We observe that six effects show a large deviation from the half-normal distribution. Figure 3.6 shows a Pareto chart including the ten most important effects.

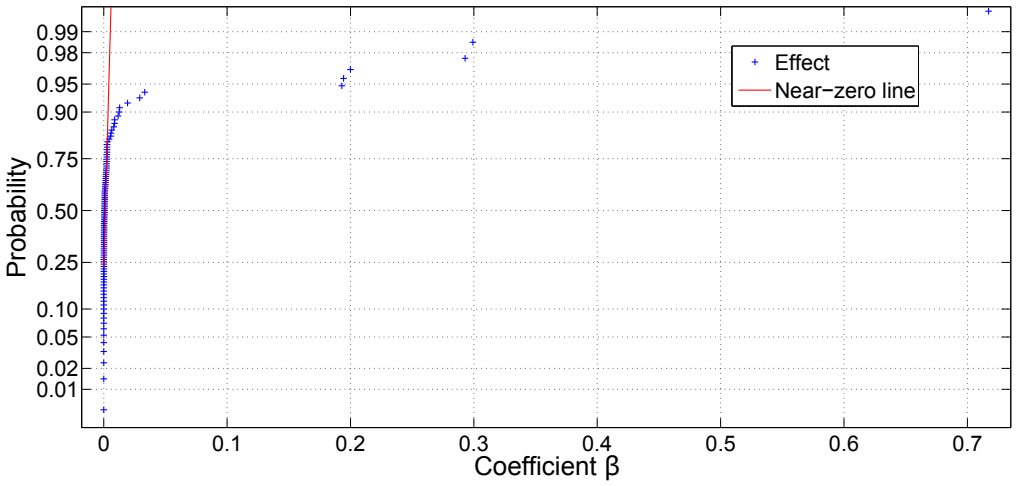

FIGURE 3.5: Half-normal plot of the effects for the fraction of gas recovered during thermal conversion of kerogen. We observe that six effects show a large deviation from the half-normal distribution.

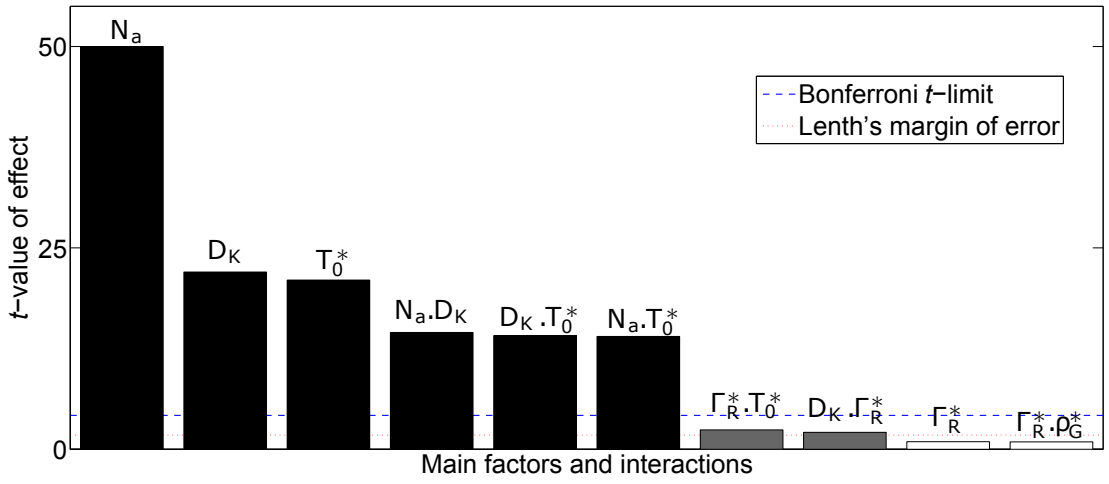

FIGURE 3.6: Pareto chart of the effects for the fraction of gas recovered during thermal conversion of kerogen. The t-values are computed with the residual obtained with the model formed of the six selected effects defined by Figure 3.5. Primary effects are represented in black, secondary in grey and insignificant effect in white.

The t-values are computed with the residual obtained with the model formed of the six selected effects (Figure 3.5). Therefore, we obtain the following classification of the dimensionless groups:

- primary numbers: N_a, D_K, T_0^*
- secondary numbers: Γ_R^*

- insignificant numbers: γ_G^*, γ_C^*, $S_{s,0}$, a_G, Δh_r^*, ρ_G^*, ρ_C^*, α, L_e and $\delta\mu_g^*$

The Arrhenius number N_a is the most important parameter for the EROI of the process. It represents an energy barrier to the chemical reactions. A small number implies fast decomposition therefore more hydrocarbons produced. The Damköhler number D_K and the initial temperature T_0^* also have an impact on the decomposition rate, although less important than the Arrhenius number.

As mentioned previously, the activation energy E_a and the pre-exponential factor A are not independent since they describe the same chemical reaction. Therefore the Arrhenius and Damköhler numbers are not independent in reality. To better represent this dependency, we replace D_K in our sensitivity analysis by the extended Damköhler number $\tilde{D_K}$ defined by Equation 2.35. Our literature review [12, 24, 52, 93] defined the following range for $\tilde{D_K}$:

$$0.1 < \tilde{D_K} < 10000 \tag{3.26}$$

Figure 3.7 shows the half-normal plot in this case. We observe that only one effect shows a large deviation from the half-normal distribution. Figure 3.8 shows a Pareto chart including the ten most important effects and we observe the following classification:

- primary number: $\tilde{D_K}$
- secondary numbers: Γ_R^*
- insignificant numbers: N_a, T_0^*, γ_G^*, γ_C^*, $S_{s,0}$, a_G, Δh_r^*, ρ_G^*, ρ_C^*, α, L_e and $\Delta\mu_g^*$

The extended Damköhler number $\tilde{D_K}$ is the most important parameter, while the Arrhenius number N_a and the reduced initial temperature T_0^* are now insignificant numbers. This shows that the impact of the chemical reaction rate on the fraction of gas recovered can be described using only $\tilde{D_K}$. A plot of f after $t = 2 \times \tau$ as a function of $\tilde{D_K}$ is given in Figure 3.9.

We observe that for $\tilde{D_K} << 10$, the fraction of recovered gas is small and the process is not efficient. In this case, the chemical reaction is slow and only a small part of the reactant has been converted after $t_{\text{prod}} = 2 \times \tau$. For $\tilde{D_K} \simeq 20$, 98% of the gas has been produced and the process is efficient. Therefore, when $\tilde{D_K} \geq 20$, the fraction of

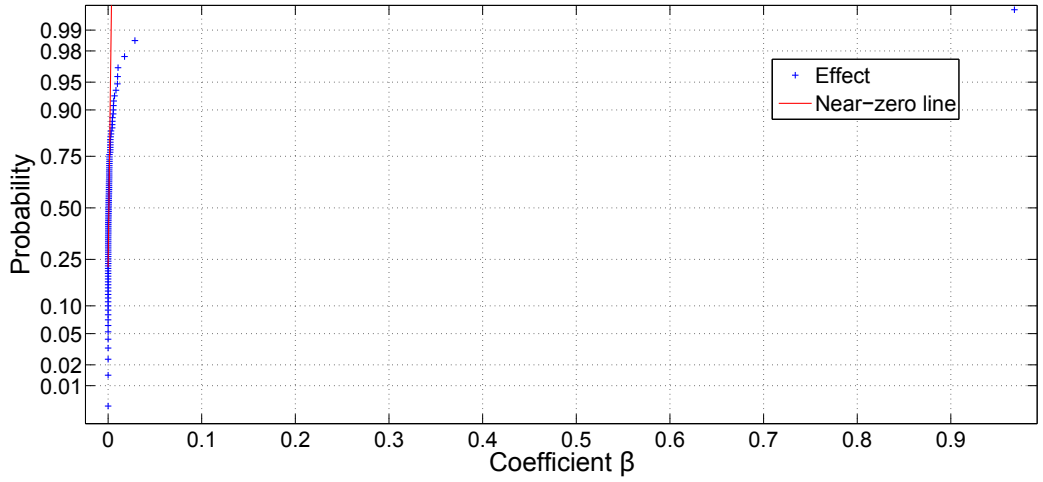

FIGURE 3.7: Half-normal plot of the effects for the fraction of gas recovered during thermal conversion of kerogen with extended Damköhler number. We observe that only one effect shows a large deviation from the half-normal distribution (the effect of $\tilde{D_K}$).

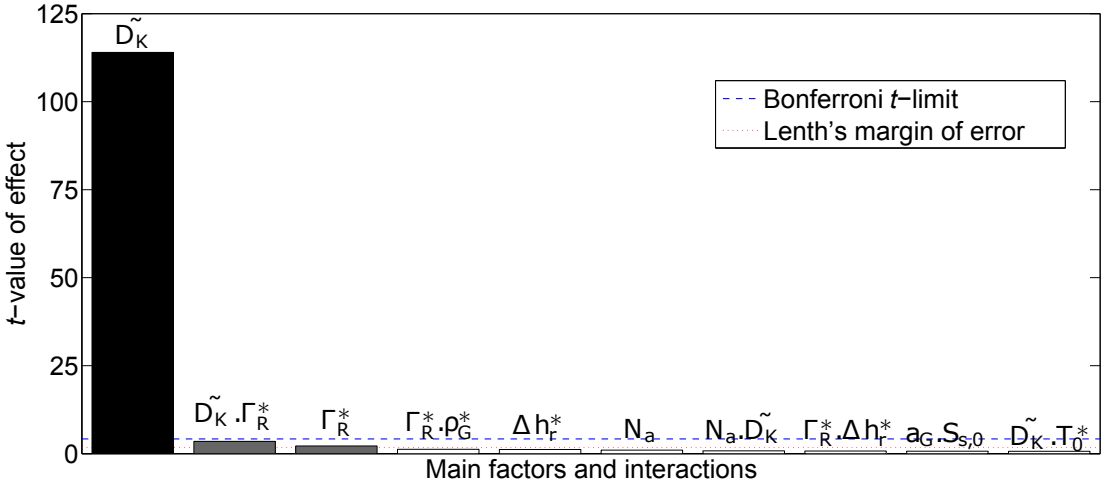

FIGURE 3.8: Pareto chart of the effects for the fraction of gas recovered during thermal conversion of kerogen with extended Damköhler number. The t-values are computed with the residual obtained with the model formed of the one most important effect defined by Figure 3.7. Primary effects are represented in black, secondary in grey and insignificant in white.

recovered gas is not much improved but more energy has been given to the domain to bring it to a larger temperature.

Figure 3.10 shows the temperature and solid saturation for test case 1 (Table 2.4) after $t_{\text{prod}} = 2 \times \tau$ for different values of $\tilde{D_K}$. We observe that for $\tilde{D_K}$=0.2 and 2, the chemical reaction is too slow and only a small amount of reactant has been converted. For $\tilde{D_K} = 20$, most of the reactant has been converted. The reaction front reaches the producer well at the same time as the temperature reaches a minimum of $0.95T_D$ in the whole domain. For $\tilde{D_K} = 200$, all reactant has been converted but the energy

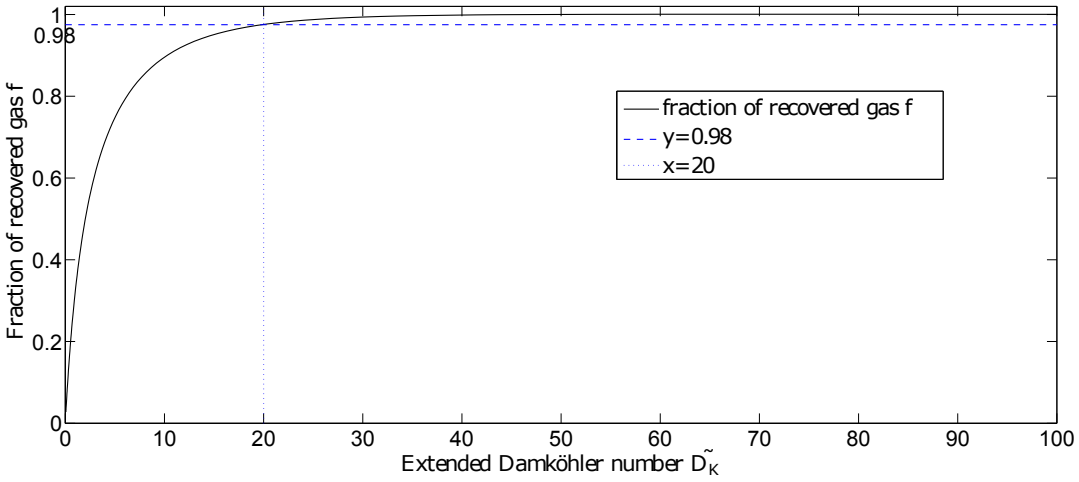

FIGURE 3.9: Fraction of recovered gas after $t_{\text{prod}} = 2 \times \tau$ as a function of $\tilde{D_K}$. We observe that 98% of the gas has been produced when $\tilde{D_K} \simeq 20$.

invested in the process is significantly larger. The reaction front is not much faster as it needs to wait for the heat conduction to propagate in the domain. During that time, an important part of the heating is used only to heat-up the rock. Thus, the optimal heater temperature of the process should be close to the one for which $\tilde{D_K} = 20$:

$$T_{opt} \approx T_{R20} = \frac{T_B}{\log D_K - \log(20)} \tag{3.27}$$

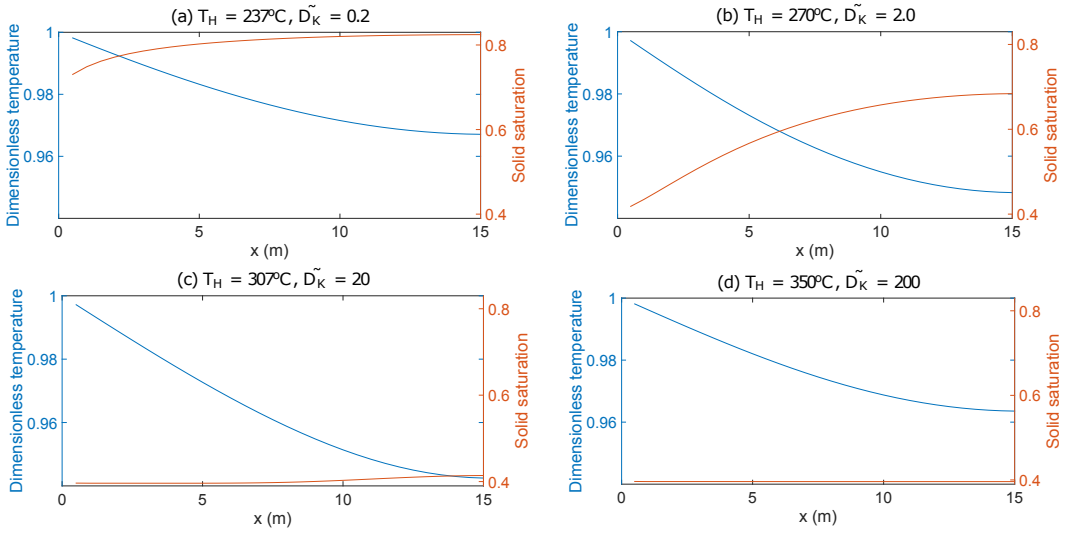

FIGURE 3.10: Temperature and solid saturation for test case 1 (Table 2.4) after $t_{\text{prod}} = 2 \times \tau$ for different values of $\tilde{D_K}$. We observe that for $\tilde{D_K}$=0.2 and 2, the chemical reaction is too slow and only a small amount of reactant has been converted. For $\tilde{D_K} = 20$, most of the reactant has been converted. For $\tilde{D_K} = 200$, all reactant has been converted but the energy invested in the process is significantly larger.

Figure 3.11 shows the EROI as a function of the heater temperature for test cases 1 and 2 (Table 2.4). The optimal heater temperature given by equation 3.27 is 306 ^oC for test case 1 and 302 ^oC for test case 2. We observe good agreement between the results and the predictions.

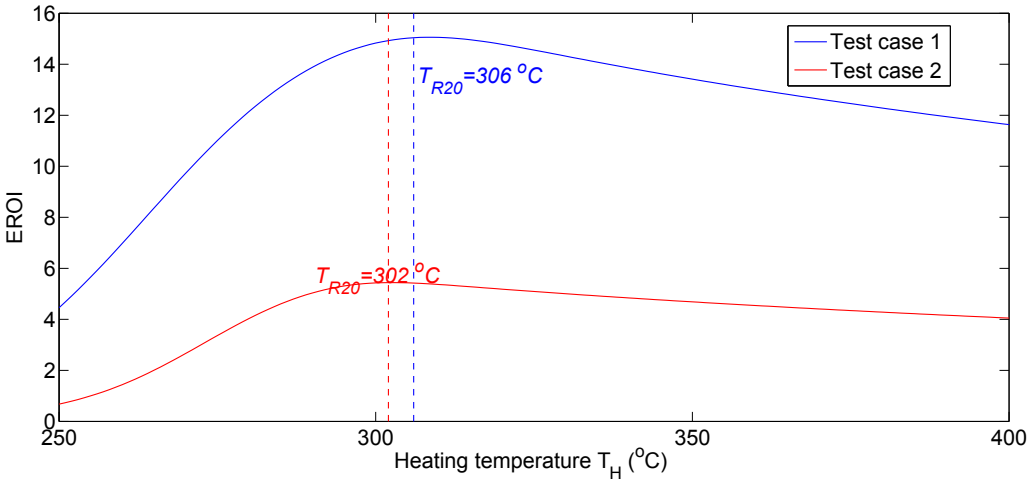

FIGURE 3.11: EROI as a function of the heater temperature for test cases 1 and 2(Table 2.4). The optimal heater temperature given by equation 3.27 is 320 ^oC for test case 1 and 305 ^oC for test case 2. We observe good agreement between the results and the predictions.

Equations 3.25 and 3.27 give a relationship between the production time t_{prod}, the distance between a heater and a producer L and the heater temperature T_H in order to maximize the EROI. Consider that we would like to have a production time of 10 years. This means that $\tau = 5$ years. For test case 1, this gives us a distance $L = 14.67$ m. In this case the Damköhler number has a value $D_K = 6.83 \times 10^{15}$ and the optimal heater temperature $T_{R20} = 310$ ^oC. Alternatively, we consider a production scenario where the heater temperature is limited by $T_H = 350$ ^oC. To maximize the EROI while minimizing the production time, we define the distance L such as $D_K = 20 \exp\left(\frac{T_B}{T_H}\right)$. For test case 1, we obtain $D_K = 7.0 \times 10^{14}$ and $L = 4.71$ m. The production time is then equal to 0.52 years.

In reality, kerogen decomposition is modelled by a set of parallel reactions with intermediate liquid and gas components. The decomposition of these intermediate components generally happens at temperature higher than 300 ^oC. In Chapter 5, we consider such a model with three reactions and observe that the same results apply when considering the minimum of the Damköhler numbers for the three reactions.

3.3.2 Level of mechanical stress

Another important response of the process is the level of mechanical stress in the domain. In our simplified model, the variation of the permeability of the rock generated by kerogen decomposition is simply modelled by an exponential function, which only depends on the saturation of the solid phase in the pore-space. In reality, the creation of large volumes of gas and liquid generates important mechanical stresses that could deform the rock or even lead to the formation of fractures [48]. The stress tensor σ can be related to the fluid pressure by:

$$\sigma = \sigma_0 - n_B \left(P - P_0\right) I \tag{3.28}$$

where σ_0 is the initial stress tensor, n_B the Biot's constant [10] and I the identity tensor. We define S the level of pressure mechanical forces in the domain by:

$$S = \max_{0 \leq x \leq L} \left(\frac{P(x) - P_0}{P_0} \right) \tag{3.29}$$

To study the impact of the 14 dimensionless groups on the function S, we perform a sensitivity analysis using DOE. Again, we use a two-level fractional factorial design of resolution V (section 3.1) and a first-order model with interaction. The response S for the corresponding values of the dimensionless numbers (Table 3.3) is obtained by numerical simulation, using the method described in Chapter 2 (section 2.2). In particular, we use a constant dimensionless time-step $\Delta t = 10^{-3}$ and a $50 \times 1 \times 1$ grid (figure 2.3).

Figure 3.12 shows the half-normal plot of effects for the sensitivity of function S. We observe that this model has more deviation from the half-normal distribution than the previous one. Fourteen effects have a large deviation from the normal distribution. Figure 3.13 shows the Pareto chart in this case. The t-values are computed with the residual obtained with the model formed of the fourteen most important effects defined by Figure 3.12.

We obtain the following classification:

- primary numbers: L_e, ρ_G^*, $\tilde{D_K}$, N_a, and T_0^*

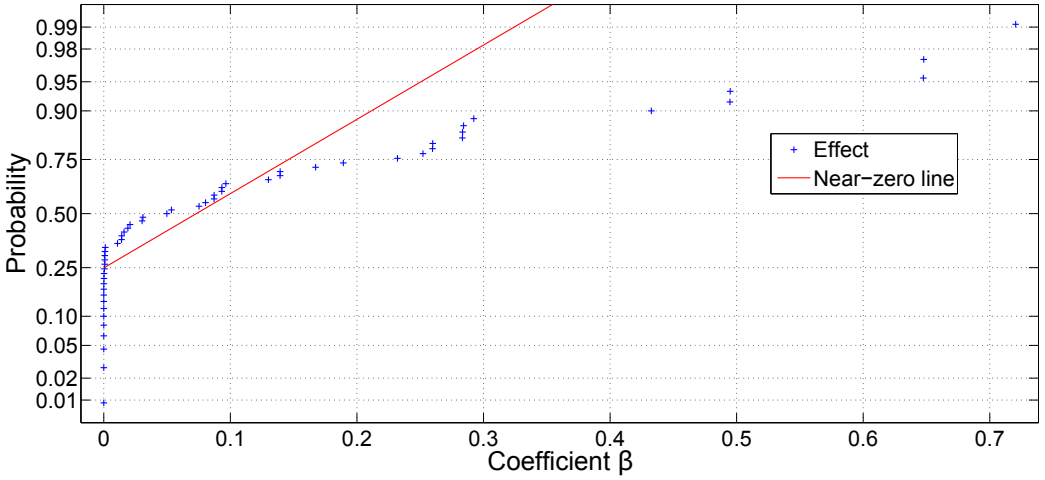

FIGURE 3.12: Half-normal plot for level of pressure mechanical forces of thermal conversion of kerogen. We observe fourteen effects that have a large deviation from the normal distribution.

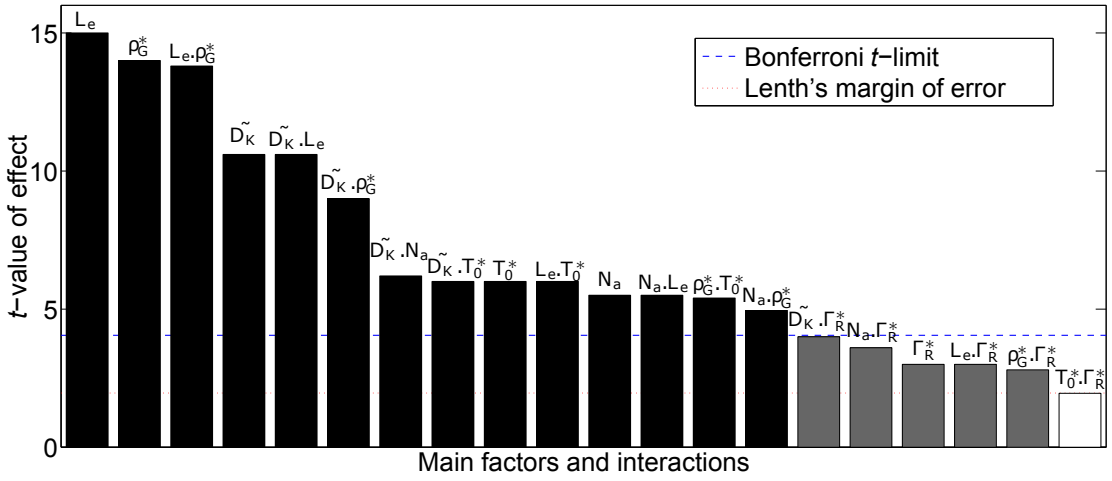

FIGURE 3.13: Pareto chart for level of pressure mechanical forces of thermal conversion of kerogen. The t-values are computed with the residual obtained with the model formed of the fourteen most important effects defined by Figure 3.12.

- secondary number: Γ_R^*
- insignificant numbers: γ_G^*, γ_C^*, $S_{s,0}$, a_G, Δh_r^*, ρ_C^*, α and $\delta\mu_g^*$

The Lewis number L_e is the most important number controlling the level of mechanical stress in the domain. The higher it is, the smaller the fluid mobilities and the higher the mechanical stress. The reduced gas density ρ_g^* and the extended Damköhler number quantify the volume of gas generated by the chemical reactions. Small ρ_g^* means a large volume of gas generated so large mechanical stress. We would like to define an upper-bound for the mechanical stress using L_e and ρ_G^*. For this, we perform 200 numerical experiments, with values for the dimensionless numbers randomly chosen in the range

defined by Table 3.3. Figure 3.14 shows the distribution of S as a function of the ratio L_e/ρ_G^*.

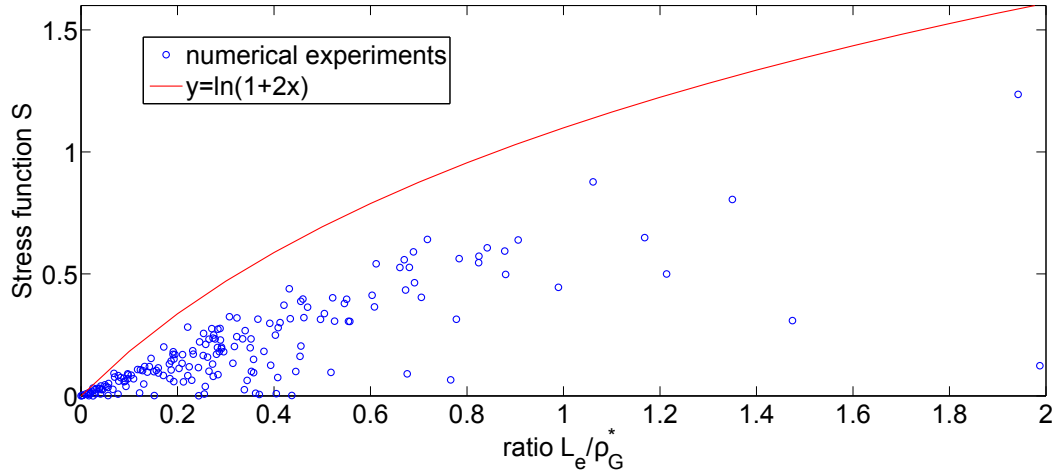

FIGURE 3.14: Distribution of mechanical stress S as a function of the ratio L_e/ρ_G^* for 200 runs with random values for the dimensionless numbers. We observe that S can be bounded by a logarithmic function.

The envelope of the experimental data points suggests an upper bound by a logarithmic function. We observe that:

$$S \leq \ln\left(1 + 2\frac{L_e}{\rho_G^*}\right) \tag{3.30}$$

Equation 3.30 can be used to define an upper bound on the mechanical stress in the domain. This bound tends to overestimate the pressure mechanical forces. To obtain a better estimate, one should include in the bound function the next primary numbers, namely $\tilde{D_K}$, N_a and T_0^*.

3.4 Application to the performance of a thermal protection system using polymer composite

We consider a thin slab of polymer material used as a thermal protection system for space-shuttle and rocket nozzles. The model is identical to the one defined by Henderson and Wiecek [34] and represented in figure 2.1b, except that the right boundary is insulated [77] (no heat loss by radiation). The performance of the thermal protection system is defined by the temperature in the protected area, on the right end of the domain. We define the thermal protection level as one minus the dimensionless right

end temperature after a dimensionless time equal to one:

$$TP = 1 - T_D\left(x_D = 1, t_D = 1\right) \tag{3.31}$$

As shown in Chapter 2, the process of thermal decomposition of polymer composite submitted to a radiative incident heat flux can be represented by the seventeen dimensionless groups defined in Table 2.2. However, we assume for consistency with previous work that the mass stoichiometric coefficient $a_G = 1$ [27, 34]. Thus, ρ_c^* and γ_C^* have no impact on the system and the model depends on 14 dimensionless groups. Minimum and maximum values for each dimensionless number are obtained by combining minimum and maximal values for each dimensional parameter. Table 3.4 gives the range for each parameter for this study. These were obtained from an extensive literature study [27, 34, 77, 94].

TABLE 3.4: Range of values for the various dimensional parameters of thermal decomposition of polymer composite submitted to a radiative incident heat flux.

Property	min	max	Property	min	max
L (m)	0.02	0.04	ϕ	0.2	0.3
K_0 (m^2)	2×10^{-18}	5×10^{-16}	α	5	10
ρ_I (kg/m^3)	1500	2000	γ_I $(J/(kgK))$	1300	1600
κ_s $(W/(mK))$	0.9	1.2	S_{s0}	0.5	0.7
ρ_R (kg/m^3)	2200	3200	γ_R $(J/(kgK))$	2200	2600
A (s^{-1})	1.5×10^{15}	3×10^{18}	E_a(J/mol)	2.2×10^5	2.6×10^5
Δh_r (J/kg)	-2×10^6	-2×10^5	n	1	50
ϵ	0.8	0.9	κ_g $(W/(mK))$	0.13	0.15
m_{wG} (kg/mol)	0.01835	0.03	γ_G $(J/(kgK))$	2600	3000
μ_g $(Pa.s)$	1.4×10^{-5}	1.6×10^{-5}	$\delta\mu_g$ $(Pa.s/K)$	2.3×10^{-8}	2.6×10^{-8}
T_H (K)	1400	1500	T_0 (K)	283.15	313.15
P_0 (Pa)	1×10^5	5×10^5			

As for thermal conversion of kerogen, data for properties such as molecular mass, heat capacity and viscosity of the gas or activation energy and pre-exponential factor are not independent in reality, but again they are assumed to be for the purpose of the sensitivity analysis. Table 3.5 gives the resulting ranges for the fourteen dimensionless groups.

To study the impact of the 14 dimensionless groups on the function TP, we perform a sensitivity analysis using DOE. Again, we use a two-level fractional factorial design of resolution V (section 3.1) and a first-order model with interaction. The response TP for the corresponding values of the dimensionless numbers (Table 3.5) is obtained

TABLE 3.5: Range of values obtained for the various scaling groups obtained for thermal decomposition of polymer composite submitted to a radiative incident heat flux. We observe that several numbers, such as D_K and L_e, vary over a large range, whereas other numbers, such as T_0^* vary over a much smaller range.

Groups	min	max	Groups	min	max
D_K	6.8×10^{17}	1.4×10^{22}	N_a	21.7	28.8
T_0^*	0.23	0.29	Δh_r^*	0.06	0.84
n	1	50	ϵ^*	1	4
L_e	3.9×10^{-3}	21.1	ρ_G^*	2×10^{-4}	3×10^{-3}
Γ_R^*	0.38	1.83	γ_G^*	1.	1.36
$\delta\mu_g^*$	1.6	2.3	α	5	10
S_{s0}	0.5	0.7	$\Delta\kappa_g^*$	0.17	0.27

by numerical simulation, using the method described in Chapter 2 (section 2.2). In particular, we use a constant dimensionless time-step $\Delta t = 10^{-3}$ and a $50 \times 1 \times 1$ grid (figure 2.3).

Figure 3.15 shows the half-normal plot of effects for the sensitivity of thermal protection level. We observe eleven effects that show a large deviation from the half-normal distribution. Figure 3.16 shows a Pareto chart including the twenty most important effects and we observe the following classification:

- primary numbers: Γ_R^*, Δh_r^*, ϵ^*, $S_{s,0}$, γ_G^*, N_a and D_K
- secondary number: T_0^*
- insignificant numbers: n, κ_g^*, ρ_G^*, α, L_e and $\Delta\mu_g^*$

The primary numbers influence the heat conduction, the radiative flux or the chemical reaction. In particular, we observe that the reduced reaction enthalpy Δh_r^* is a primary parameter. Figure 3.17 compares the temperature and solid saturation for the decomposition of material H41N (Table 2.1) after $t = 0.2\tau$ for different reduced reaction enthalpies.

We observe that for $\Delta h_r^* = 0.06$, the temperature profile is very similar to the one when the chemical reaction is ignored. In this case, the reaction has little impact on the heat propagation. However, for $\Delta h_r^* = 0.84$, the temperature is significantly reduced through the domain. Near the reaction front (two peaks since two different values for D_K), a significant part of energy is consumed by the decomposition. Therefore, the temperature is reduced only when the chemical reaction is important. Before the chemical reaction

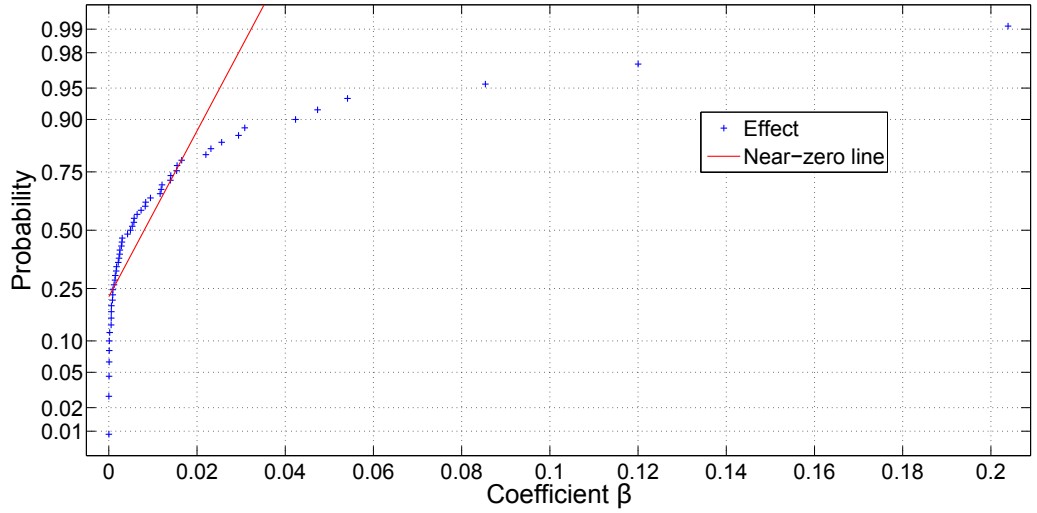

FIGURE 3.15: Half-normal plot of the effects for the thermal protection level of polymer composite. We observe eleven effects that show a large deviation from the half-normal distribution.

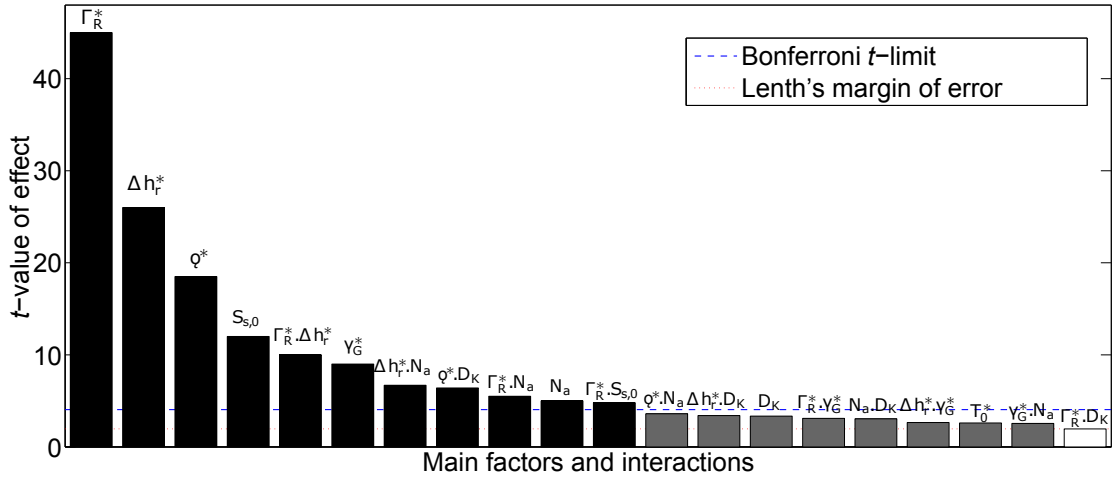

FIGURE 3.16: Pareto chart of the effects for the level of thermal protection of polymer composite. The t-values are computed with the residual obtained with the model formed of the eleven most important effects defined by Figure 3.15. Primary effects are represented in black, secondary in grey and insignificant in white.

becomes significant, the temperature increases in the domain simply by heat conduction in the rock and pores and the right end reaches a temperature $T < T_{R1}$, when T_{R1} is the reaction temperature defined by Equation 2.34, after the approximate time:

$$t = t_{cond}\left(T\right) = T_D\left(1 + \Gamma_R^* S_{s,0}\right)\tau < \tau \tag{3.32}$$

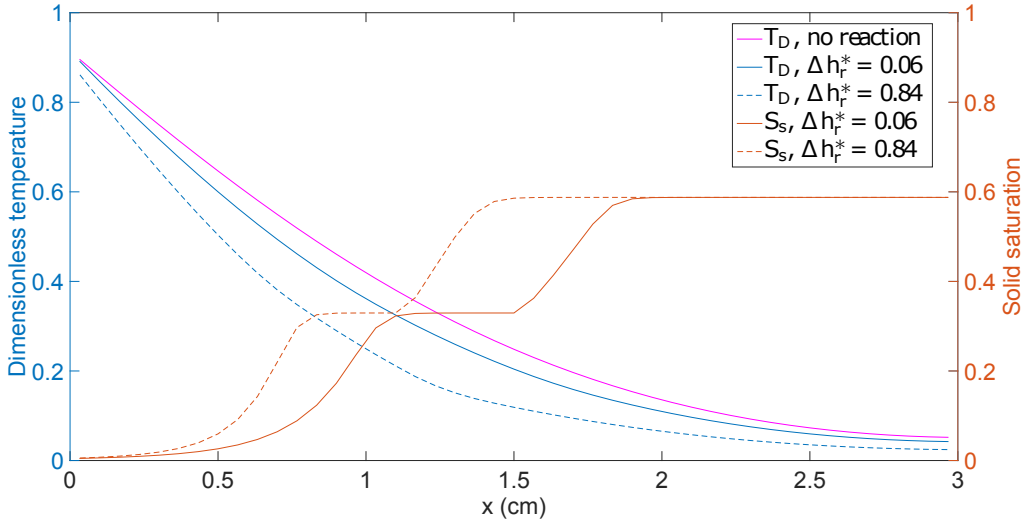

FIGURE 3.17: Temperature and saturation for decomposition of material H41N (Table 2.1) after $t = 0.2\tau$ with different value of reaction enthalpy. We observe that large Δh_r^* delays the heat propagation in the domain.

where τ is the time scale of heat conduction in the domain (Equation 2.24). Therefore, the level of thermal protection satisfies:

$$TP < 1 - T_{R1,D} = \frac{T_H - T_{R1}}{\Delta T} \tag{3.33}$$

So the system is inefficient when protecting from temperature smaller than T_{R1}. However, when the domain reaches a temperature higher than T_{R1}, the chemical reaction acts as a barrier for the heat conduction. As the reactant is consumed, the temperature increases slowly as the system requires energy for the decomposition. Thus, T remains smaller than T_{R100}, defined as the temperature for which the dimensionless reaction rate is equal to 100:

$$T_{R100} = \frac{T_B}{\ln(D_K) - \ln(100)} \tag{3.34}$$

For $T > T_{R100}$, the chemical reaction is almost instantaneous and the energy barrier is overcome. Thus, the time for which $T < T_{R100}$ can be approximated by the sum of $t_{cond}(T_{R100})$ and $t_{\Delta H}(T_{R100})$, where $t_{\Delta H}$ is the time necessary for the system to receive from the radiative source enough energy to consume all reactant:

$$t_{\Delta H}(T) = \frac{\Gamma_r^* S_{s,0}}{\epsilon^*} \left(-\Delta h_r^* + (\gamma_G^* - 1) T_D\right) \tau \tag{3.35}$$

To verify this approximation, we perform 200 numerical experiments, with values for the dimensionless numbers randomly chosen in the range defined by Table 3.5. Figure

3.18 shows the distribution of $t\,(T < T_{R100})$ as a function of $t_{cond}\,(T_{R100}) + t_{\Delta H}\,(T_{R100})$. We observe good agreement between the two, so:

$$t_{T<T_{R100}} \approx t_{cond}\,(T_{R100}) + t_{\Delta H}\,(T_{R100}) \tag{3.36}$$

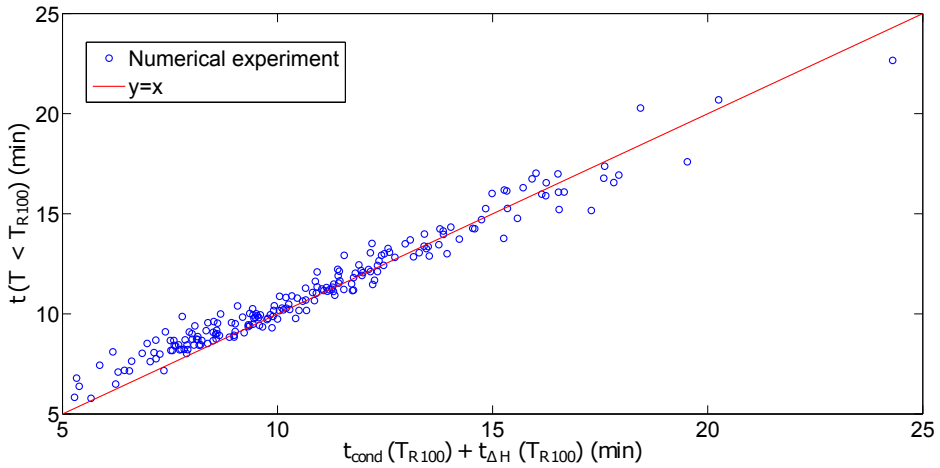

FIGURE 3.18: Distribution of protection time $t_{T<T_{R100}}$ as a function of the sum of $t_{cond}\,(T_{R100})$ and $t_{\Delta H}\,(T_{R100})$ for 200 runs with random values for the dimensionless numbers .

For the material denoted H41N (Table 2.1), a thickness of 3 cm gives temperatures $T^1_{R100} = 431\ ^oC$ and $T^2_{R100} = 550\ ^oC$ and a protection time $t\,(T < 550^oC)$ of ≈ 18.1 min. For the material denoted MXBE-350 (Table 2.1), a thickness of 3 cm gives $T^1_{R100} = 312\ ^oC$ and $T^2_{R100} = 425\ ^oC$ and a protection time $t\,(T < 425^oC)$ of ≈ 17.9 min. Therefore, MXBE-350 gives a more efficient thermal protection than H41N with a very similar protection time.

3.5 Summary

In this chapter, we used DOE to identify the primary parameters for two processes of interest: the thermal conversion of kerogen into non-reactive gas, and the thermal decomposition of polymer composite when used as heat-shielding for space-craft re-entry. We used a two-level factorial design [2] combined with Response Surface Methodology (RSM) [65] to classify the dimensionless numbers into primary parameters, secondary parameters and insignificant parameters.

The methodology was first applied to study the energy efficiency of thermal conversion of kerogen into gas. The extended Damköhler number $\tilde{D_K}$ was found to be the most important parameter of the process. When $\tilde{D_K}$ was small, the reaction was slow and the process was inefficient. However, when $\tilde{D_K}$ was very large, the reaction was very fast, but since the heat conduction was the primary mechanism defining the time scale of the process, a significant part of the energy given to the system was simply used to heat the rock. This analysis allowed us to identify an optimal heater temperature for the performance of the process (Equation 3.27).

Then, we studied the level of mechanical stress in the domain. The two most important dimensionless groups for this case were the pressure Lewis number L_e, which quantifies the ratio of heat diffusivity to pressure diffusivity, and the reduced initial gas density ρ_g^*, which is equal to the ratio of initial gas density to solid density. Our analysis led to an estimation of the maximum pressure in the domain during the process (Equation 3.30).

Finally, we used DOE to measure the performance of polymer thermal protection systems. We observed that the most important numbers for this case are the reduced volumetric heat capacity of the reactant Γ_R^* and the reduced heat of decomposition Δh_r^*. The temperature increased slowly when the chemical reaction was important as the system required enough energy for the decomposition. This analysis allowed us to identify a protection temperature (Equation 3.34) and a protection time (Equation 3.36).

We conclude that for both processes, the main interactions are the ones between the heat conduction and the chemical reaction and the ones between the chemical reaction and the mass convection. The heat conduction induced the chemical reaction which induced the mass convection. The other interactions are secondary or insignificant compared to those. In the next chapter, we evaluate the use of decoupling methods, or so-called Operator Splitting for solving numerically the equations. The challenge is to identify a method that is computationally attractive but preserve the main interaction between operators to limit the discretization error. Our dimensionless analysis showed that the main interactions would be conserved for a decoupling method where the heat conduction is performed first, followed by the chemical reaction and finally the heat and mass convection step. This method is presented in the next chapter and compared with the most common Operator Splitting methods from the literature.

Chapter 4

Evaluation of Operator Splitting (OS) methods for the thermal decomposition of solid reactant into non-reactive gas

Operator Splitting (OS) methods have been previously applied to a wide range of problems, including groundwater transport simulations [6], air pollution modelling [51] and combustion-reaction problems [68]. They provide a framework to deal separately with the transport and the chemical reaction steps and therefore simplify the numerical simulation of the system. However, decoupling the equations introduces an additional source of error [88]. The convergence and precision of OS methods have been extensively studied for linear or quasi-linear operators [26, 88].

The objective of this chapter is to identify the best splitting technique for a highly non-linear system: the thermal decomposition of solid reactant into non-reactive gas. We describe the most common methods from the literature and evaluate their precision and performance on two test cases describing kerogen decomposition (Table 2.4). To simplify the notation, we describe the various splitting methods on a Cauchy problem of the form:

$$\begin{cases} \dfrac{\partial u}{\partial t} = A.u + K.u, \quad t \in (0, T]\,. \\ u(0) = u_0 \end{cases} \tag{4.1}$$

where A represents the advection and thermal conduction operator and K the chemical reaction operator. In the general case, A and K are non-linear operators. A splitting method is said to be k-order accurate or to have a splitting error of order k if:

$$\underline{u}\left(t^{n+1}\right) - u^{n+1} = \mathcal{O}\left(\Delta t^n\right)^k \tag{4.2}$$

where $\underline{u}$ is the exact solution of Equation 4.1 and Δt^n the time-step of the splitting betwenn t^n and t^{n+1}.

4.1 Operator splitting methods

Operator splitting methods offer two distinct approaches. In a Sequential Non-Iterative Approach (SNIA), each operator is applied once sequentially. In this section, we describe two of these methods, namely the Sequential Split Operator (SSO) [18] and the Strang-Marchuk Split Operator (SMSO). The second category of operator splitting methods is the Sequential Iterative Approach (SIA), which attempts to eliminate or control the splitting error through an iterative process. Details of the implementation of the methods are given in Appendix B.

4.1.1 Sequential Non Iterative Approach

The simplest and most common of SNIA methods is the Sequential Split Operator (SSO) [18], which is a sequence of one transport step followed by one chemical step:

$$\begin{cases} \dfrac{\partial u^*}{\partial t} = A.u^*, & t \in \left[t^n, t^{n+1}\right], u^*(t^n) = u(t^n) \\ \dfrac{\partial u^{n+1}}{\partial t} = K.u^{n+1}, & t \in \left[t^n, t^{n+1}\right], u^{n+1}(t^n) = u^*(t^{n+1}) \end{cases} \tag{4.3}$$

which will be denoted SSO-AK to indicate the sequence of operator used. SSO can be done the opposite way with one chemical step followed by one transport step (SSO-KA):

$$\begin{cases} \dfrac{\partial u^*}{\partial t} = K.u^*, & t \in \left[t^n, t^{n+1}\right], u^*(t^n) = u(t^n) \\ \dfrac{\partial u^{n+1}}{\partial t} = A.u^{n+1}, & t \in \left[t^n, t^{n+1}\right], u^{n+1}(t^n) = u^*(t^{n+1}) \end{cases} \tag{4.4}$$

For SSO-AK and SSO-KA, the splitting error arising from decoupling the governing equations is of order 1 [88]. For linear operators, this error can be related to the asymmetry of the decoupling. The classical SSO can be modified by using two time-steps and alternating the operators in an effort to cancel the splitting error of order 1, as is done in the Strang-Marchuk Split Operator (SMSO) (sometimes called the Alternate Split Operator (ASO)) [18, 44, 84]:

$$\begin{cases} \dfrac{\partial u^*}{\partial t} = A.u^*, & t \in \left[t^n, t^{n+1/2}\right], u^*(t^n) = u(t^n) \\ \dfrac{\partial u^{**}}{\partial t} = K.u^{**}, & t \in \left[t^n, t^{n+1}\right], u^{**}(t^n) = u^*(t^{n+1/2}) \\ \dfrac{\partial u^{n+1}}{\partial t} = A.u^{n+1}, & t \in \left[t^{n+1/2}, t^{n+1}\right], u^{n+1}(t^n) = u^{**}(t^{n+1}) \end{cases} \tag{4.5}$$

For linear operators, SMSO cancels the splitting error of order 1 [88] and so is of order 2. However, these findings do not necessarily apply to systems where the coupling between transport and chemical reactions is strongly non-linear.

4.1.2 A New Splitting Method: SSO-CKA

When the operator K is performed before A, as in SSO-KA and in a half step of SMSO, the chemical reactions are computed with the temperature calculated at the previous time-step. In Chapter 3, we observed that thermal conduction is the primary mechanism controlling the thermal decomposition of solid reactant into non-reactive gas. Therefore, we try to reduce the discretization error of SSO by using a splitting scheme where the thermal conduction is performed first (operator C), followed by a chemical reaction step (operator K) and finally the advection part with no thermal conduction (operator A$'$). This method is defined as SSO-CKA:

$$\begin{cases} \dfrac{\partial u^*}{\partial t} = C.u^*, & t \in \left[t^n, t^{n+1}\right], u^*(t^n) = u(t^n) \\ \dfrac{\partial u^{**}}{\partial t} = K.u^{**}, & t \in \left[t^n, t^{n+1}\right], u^{**}(t^n) = u^*(t^{n+1}) \\ \dfrac{\partial u^{n+1}}{\partial t} = A'.u^{n+1}, & t \in \left[t^n, t^{n+1}\right], u^{n+1}(t^n) = u^{**}(t^{n+1}) \end{cases} \tag{4.6}$$

SSO-CKA tries to take advantage of the fact that most of the effect of advection-diffusion on the chemical reaction comes from heat conduction if (1) reactants are transported slowly in the domain and (2) reaction enthalpies are small. Condition (1) implies that the heat and mass advection operator A' has only a small effect on the operator K.

It is true if only a small proportion of the reactant exists in the gas phase. For our simplified model of the thermal decomposition of kerogen, all reactant is in the solid phase. Condition (2) implies that K has a small effect on C. Reaction enthalpies are generally neglected in the modelling of In-Situ Upgrading of oil shale [24, 52]. However, we noted in Chapter 3 that they could have a large impact on the processes and we will see in this chapter how it can affect the precision of SSO-CKA.

4.1.3 Sequential Iterative Approach

Unlike SNIA, each sub-step of an iterative scheme solves an approximation to the fully coupled PDE system. The simplest of these methods is the Iterative Split Operator (ISO) [26]:

$$\begin{aligned}
&\frac{\partial u^*_{2i+1}}{\partial t} = A.u^*_{2i+1} + K.u^*_{2i} \qquad t \in \left[t^n, t^{n+1}\right].\\
&u^*_{2i+1}(t^n) = u_n(t^n)\\
&\frac{\partial u^*_{2i+2}}{\partial t} = A.u^*_{2i+1} + K.u^*_{2i+2} \quad t \in \left[t^n, t^{n+1}\right].\\
&u^*_{2i+2}(t^n) = u_n(t^n)
\end{aligned} \tag{4.7}$$

for $i = 0, 1, ..., m$ or until convergence. The function u^*_0 is an arbitrarily chosen initial guess on the interval $[t^n, t^{n+1}]$ and

$$u_{n+1}(t) = u^*_{2m+1}(t) \quad t \in \left[t^n, t^{n+1}\right]. \tag{4.8}$$

ISO is stable and converges for linear operators [26]. Note that each of the sub-steps is not necessarily stable. For example, if the chemical constants in K are larger than 1, the first step is obviously unstable. It is the iterations over the splitting scheme and the alternating between implicit and explicit treatment for each operators that stabilise the method in linear systems. However, we do not have such a result for non-linear operators.

4.2 Numerical simulations

The various methods presented have been developed inside EXTEND (EXtended Thermal simulator for Evaluating new Numerical Discretization). The source code of EXTEND is provided in the CD-ROM attached to this thesis. We use the Finite Volume

Method (FVM) for the discretization with an overall molar composition formulation. The resulting discretized non-linear equations are solved using Newton's method. The numerical methods used in the software are detailed in Appendix B.

We consider the 1D simplified model describing the thermal conversion of kerogen represented in figure 2.1a. We use the $50 \times 1 \times 1$ grid shown in figure 2.3. The heater well is located on the left of the grid and the producer well on the right. The focus of this work is entirely on the time integration so we always consider the same grid.

Initially, we use a constant dimensionless time step Δt. In section 4.3, we compare the precision of FIM and SNIA methods for test cases 1 and 2 (Table 2.4) for different values of Δt between 0.001 and 0.01 . Then, in section 4.4, we compare the convergence of FIM and ISO for test cases 1 and 2 (Table 2.4) for $\Delta t = 0.01$. Finally, in section 4.5, we compared the precision of FIM and SSO-CKA for a time-step strategy based on the time truncation error and perform a sensitivity analysis.

4.3 Comparison of FIM and SNIA

We compare the precision of FIM, SSO-AK, SSO-KA, SMSO and SSO-CKA on two test cases describing thermal conversion of kerogen (Table 2.4). For each test case, we define a reference solution by solving the full system of equations with FIM with a dimensionless time-step $\Delta t_D = 10^{-4}$ and a $50 \times 1 \times 1$ mesh. The reference solution is denoted by $\overline{P}$ for pressure, $\overline{T}$ for temperature, $\overline{S_p}$ for saturations.

We then study the evolution of the relative error with the reference solution for FIM, SSO-AK, SSO-KA, SMSO and SSO-CKA as a function of the time-step for a $50 \times 1 \times 1$ mesh. We use the following definitions for the normalized error L_1 for each variable:

$$\begin{aligned} e_P &= \max_n \left(\frac{1}{n_d} \sum_{x_j} \frac{|P(t^n, x_j) - \overline{P}(t^n, x_j)|}{P_0} \right), \\ e_T &= \max_n \left(\frac{1}{n_d} \sum_{x_j} \frac{|T(t^n, x_j) - \overline{T}(t^n, x_j)|}{\Delta T} \right) \\ e_S &= \max_p \max_n \left(\frac{1}{n_d} \sum_{x_j} |S_p(t^n, x_j) - \overline{S_p}(t^n, x_j)| \right) \end{aligned} \tag{4.9}$$

and the total L_1 error is defined as:

$$e_{L_1} = \frac{e_P + e_T + e_S}{3} \tag{4.10}$$

Note than all numerical simulation are done with the same grid size. Grid refinement study should be done in the future especially as the size of the grid could impact greatly the chemical reactions.

For SMSO, we use two time-steps to solve the chemical reactions. This way, the four methods perform the same number of transport steps and the same number of chemical reaction steps. For SSO-CKA, we perform one additional heat conduction step. However, since the heat conduction has been extracted from the operator A, the temperature can be treated explicitly in the transport step [59]. This way, the computational effort is roughly the same for the four SNIA methods.

Figure 4.1 shows the evolution of the normalized errors with time-step for test case 1 (Table 2.4). The time-steps represented in the x-axis are Δt_D for SSO and $\Delta t_D/2$ for SMSO, so that the four SNIA methods perform the same number of transport steps and the same number of chemical reaction steps. We observe that SSO-AK gives a large pressure error. The pressure rises during the chemical reaction step and could reach non-physical values if not relaxed by a transport step afterwards. However, we obtain a small saturation error. On the other hand, SSO-KA has a limited pressure error but the saturation and composition errors are large. SMSO gives a compromise between the two methods but the pressure and saturation errors are still too large. Figure 4.3a compares the L_1 error for FIM, SSO-KA and SSO-CKA. Since SSO-AK and SMSO have a very large pressure error, their errors L_1 are also very large and are not shown here. We observe that SSO-CKA gives the lowest error of the four SNIA methods.

For test case 2 (Figure 4.2), we also observe a large pressure error for SSO-AK. SSO-KA gives a large saturation error and SMSO gives a compromise between the two but still has a larger saturation error than SSO-CKA. Figure 4.3b compares the L_1 error for FIM, SSO-KA, SMSO and SSO-CKA. Again, SSO-AK is not shown here since it has a very large pressure error, but we observe that SMSO is more precise than SSO-KA in this case. However, SSO-CKA still gives the lowest error of the four SNIA methods.

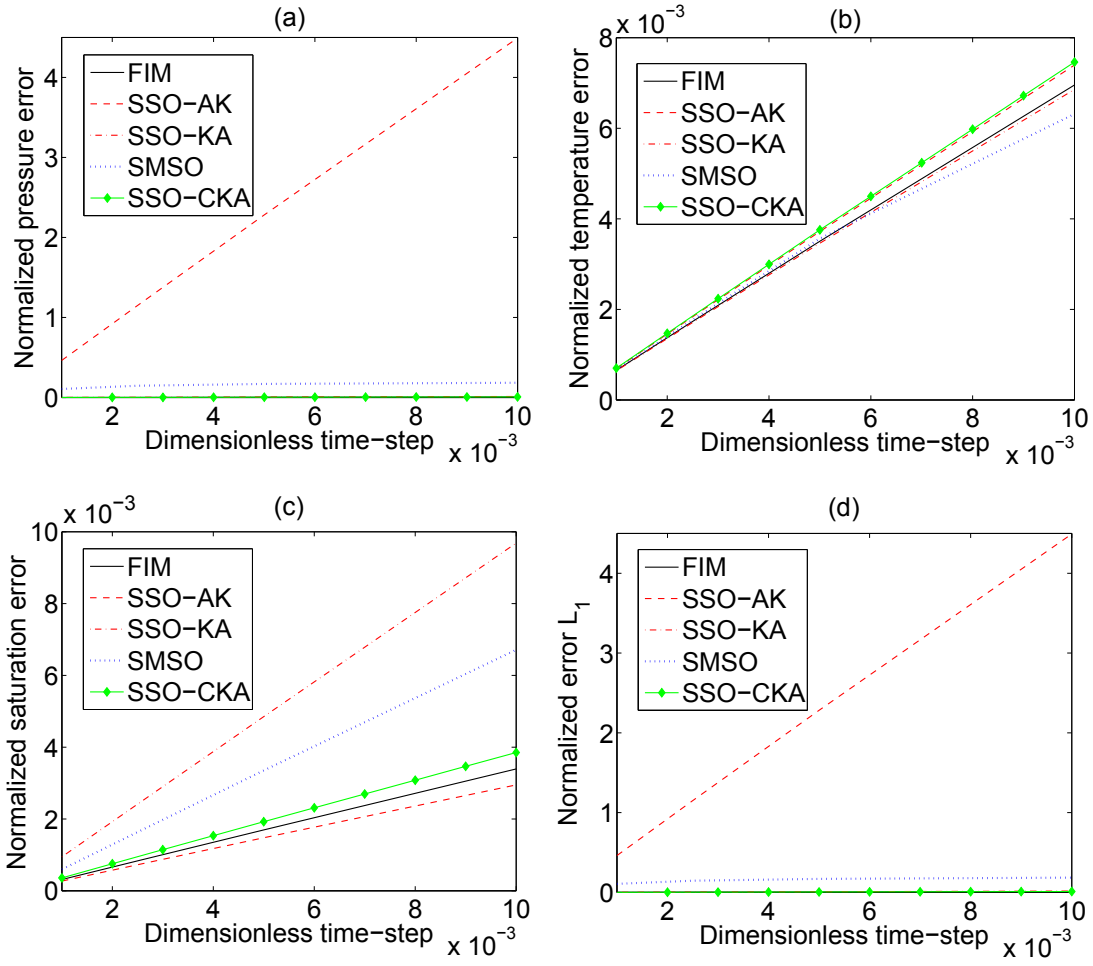

FIGURE 4.1: Evolution of the normalized errors of FIM, SSO-AK, SSOKA, SMSO and SSO-CKA with time-step for test case 1 (Table 2.4). We observe a very large pressure error for SSO-AK and SMSO, and a large saturation error for SSO-KA.

4.4 Convergence of ISO

Since the mathematical model for thermal decomposition of kerogen is non-linear, we do not have any analytical results concerning the stability and convergence of ISO. To assess its applicability, we compare the convergence behaviour with that obtained from FIM for test cases 1 and 2. Figure 4.4 shows the number of non-linear iterations used to solve the transport step for each case with a dimensionless time-step $\Delta t_D = 0.01$, using FIM and ISO. Details of our implementation of ISO are given in Appendix B. In particular, the initial guess for time-step $n+1$ was chosen as $u_0^* = u^n$.

For test case 1, ISO performs nearly five times as many non-linear iterations than FIM. This is because the stability error arising from the explicit treatment of each of the operators in each sub-step is too large and is not cancelled by alternating and iterating over

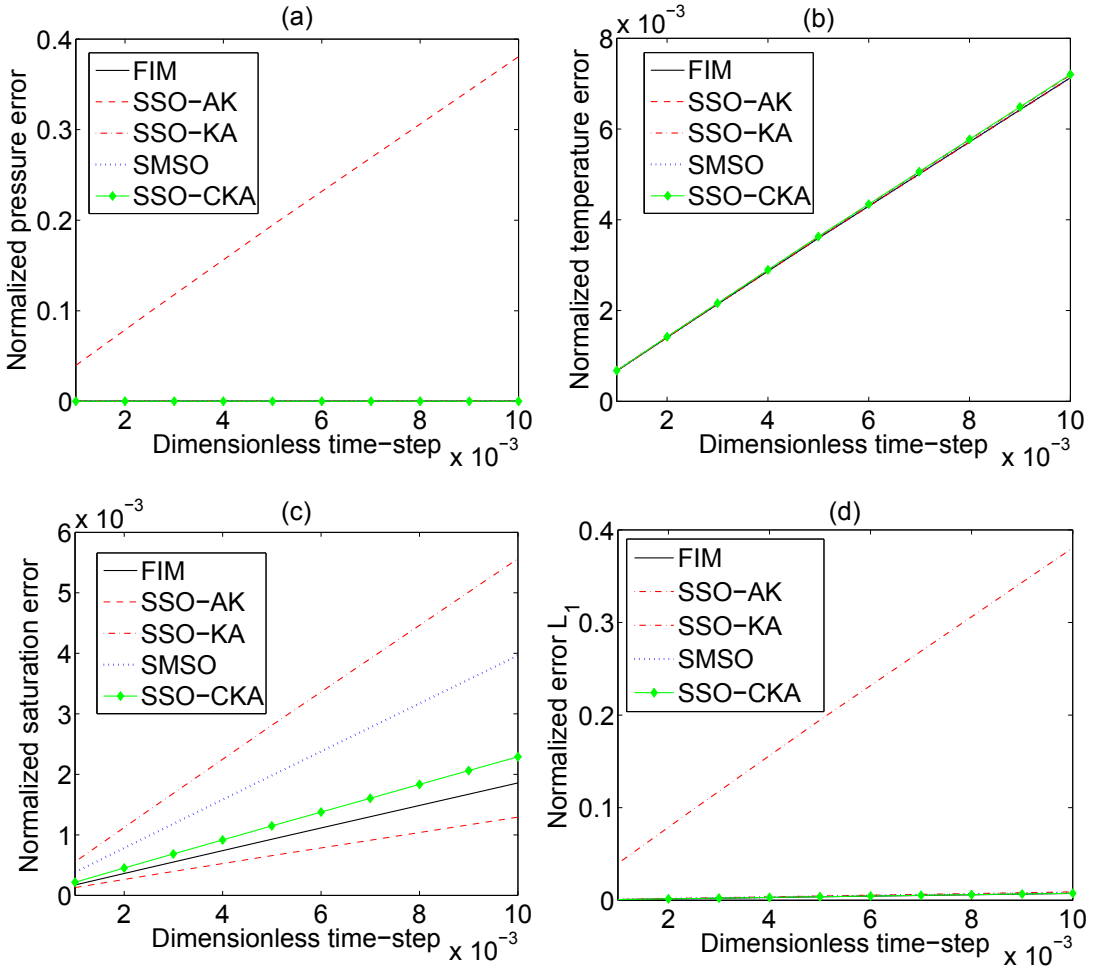

FIGURE 4.2: Evolution of the normalized errors of FIM and SSO-AK, SSO-KA, SMSO and SSO-CKA with time-step for test case 2 (Table 2.4). We observe a very large pressure error for SSO-AK and a large saturation error for SSO-AK. SMSO gives a compromise between the two but still has larger saturation error than SSO-CKA.

the splitting scheme. The difference is even larger for test case 2, with ISO performing nearly 20 times as many non-linear iterations than FIM.

It should be noted that the choice of the initial guess u_0^* can have a large impact on the performance of the method. However, we were unable to find a better choice that $u_0^* = u^n$. Finding the right guess that ensures the stability of the splitting iteration could potentially make ISO applicable for the numerical simulation of the thermal processes considered here.

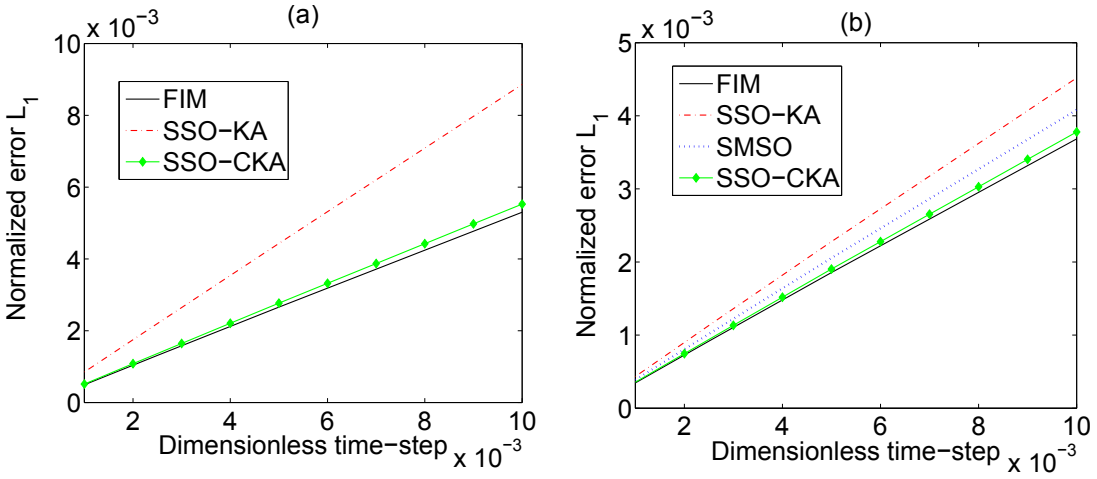

FIGURE 4.3: Evolution of normalized L_1 error of FIM and SSO-AK, SSO-KA, SMSO and SSO-CKA for (a) test case 1 and (b) test case 2. For test case 1, SSO-AK and SMSO gives very large L_1 error and are not represented here. The same is true for SSO-AK for test case 2. We observe that in both cases SSO-CKA gives the lowest error of the four SNIA methods.

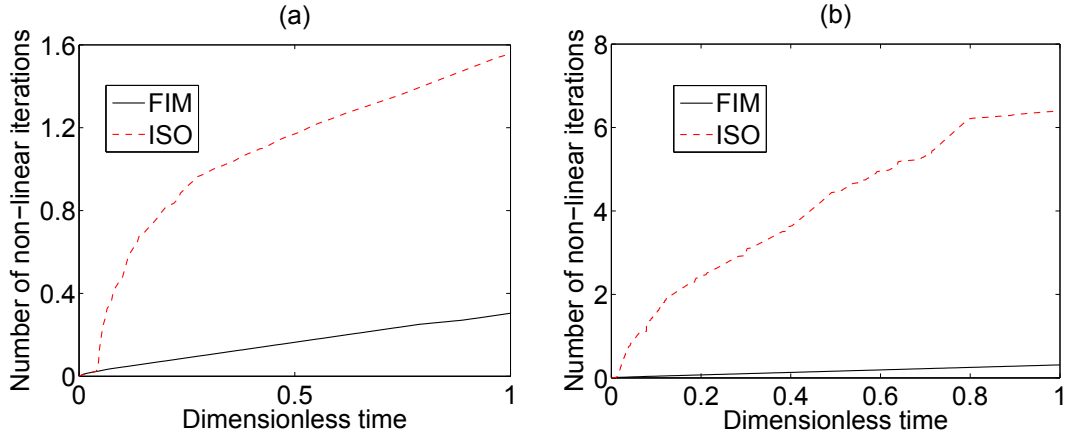

FIGURE 4.4: Number of non-linear transport iterations for (a) test case 1 and (b) test case 2 with a dimensionless time-step $\Delta t_D = 0.01$ for both FIM and ISO. We observe a large difference between the two methods, which is due to convergence failures for ISO.

4.5 Time-step strategy comparison for FIM and SSO-CKA

In section 4.3, we compared the precision of FIM and the four SNIA methods for two test cases and we showed that in both cases SSO-CKA gives the lowest discretization error of the four SNIA methods. However, this comparison was done for simulations with a constant time-step. In reservoir simulation, we generally use an adaptive time-step strategy to accelerate convergence and minimise CPU time. In this section, we present a time-step strategy based on maximum time truncation error and change in the variables

over the time. We then perform a sensitivity analysis to compare the performance of FIM and SSO-CKA using this time-step strategy for different values of the dimensionless numbers.

4.5.1 Time truncation error

The local truncation error is an a-posteriori error estimator for the solution of a PDE. Consider that we have a numerical solution of our PDE for time t_k, $0 \leq k \leq n$ with variable time-step Δt_k. An estimation $\tilde{y_{n+1}}$ of the solution y_{n+1} for the next time-step Δt_{n+1} can be obtained by:

$$\tilde{y_{n+1}} = y_n + \delta y \frac{\Delta t_{n+1}}{\Delta t_n} \tag{4.11}$$

where $\delta y = y_n - y_{n-1}$. Thus, the local time truncation error is defined by

$$tte = y_{n+1} - \tilde{y_{n+1}} \tag{4.12}$$

To limit the discretization error and the chances of convergence failure, an efficient time-stepping strategy consists of controlling the time truncation error and the maximum variable change with the evolving time-step:

$$\Delta t_{n+1} = \Delta t_n \min\left(\Theta, \frac{\eta}{\max tte}, \frac{\eta'}{\max \delta_y}\right) \tag{4.13}$$

where Θ is the maximum time-step increase factor, η is the target time truncation error and η' the target maximum variable change. In this work, we initially choose $\Theta = 2$ and $\eta = \eta' = 0.01$, which are typical values for reactive flow and are suggested by Fan et al. [24]. We verified that for test cases 1 and 2, this gives us a L_1 error of 10^{-3} for FIM and SSO-CKA. This shows that the splitting error of SSO-CKA is limited for both test cases. However, parameters such as the reaction enthalpy and specific heat capacities can have a large impact on its precision. To study this error, we perform a sensitivity analysis using DOE.

4.5.2 Sensitivity analysis

In this section, we investigate the dependency of the splitting error of SSO-CKA with the physical parameters of the problem using the dimensionless numbers defined in Chapter

2 (Table 2.2). The range of each number is given in Table 3.3 and we used the extended Damköhler number $\tilde{D_K}$ (Equation 2.35) instead of the standard Damköhler number D_K with the range defined by Equation 3.26. We study the ratio of L_1 error:

$$r = \frac{e_{L1}\,(\text{SSO-CKA})}{e_{L1}\,(\text{FIM})} \tag{4.14}$$

We use a first order model with interaction (Chapter 3, Equation 3.3). The results are interpreted using a half-normal plot and a Pareto chart (Figures 4.5 and 4.6, see Chapter 3, section 3.2.2). We observe twelve effects that have a large deviation from the normal distribution. The Pareto chart is then constructed with the residual obtained from the model including these twelve effects.

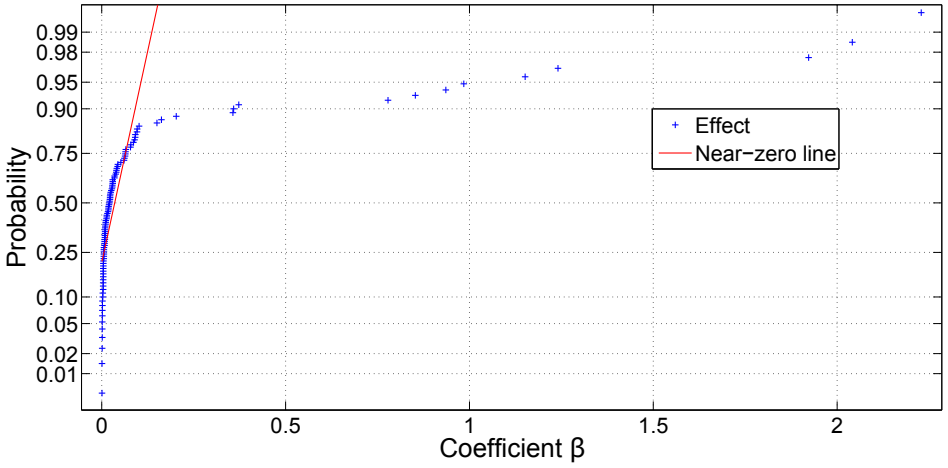

FIGURE 4.5: Half-normal plot of the effects for the ratio of L_1 error between FIM and SSO-CKA methods. We observe twelve effects that have a large deviation with the normal distribution.

We obtain the following classification:

- primary numbers: $\tilde{D_K}$, Γ_R^*, Δh_r^*, γ_G^* and a_G
- secondary numbers: L_e and ρ_G^*
- insignificant numbers: N_a, T_0^*, γ_C^*, $S_{s,0}$, ρ_C^*, η, and $\delta\mu_g^*$

We observe that the primary numbers define the chemical rate, the heat capacities ratio and the heat of decomposition. This is not surprising, since an important part of the splitting error arises from the decoupling between heat conduction and chemical reaction.

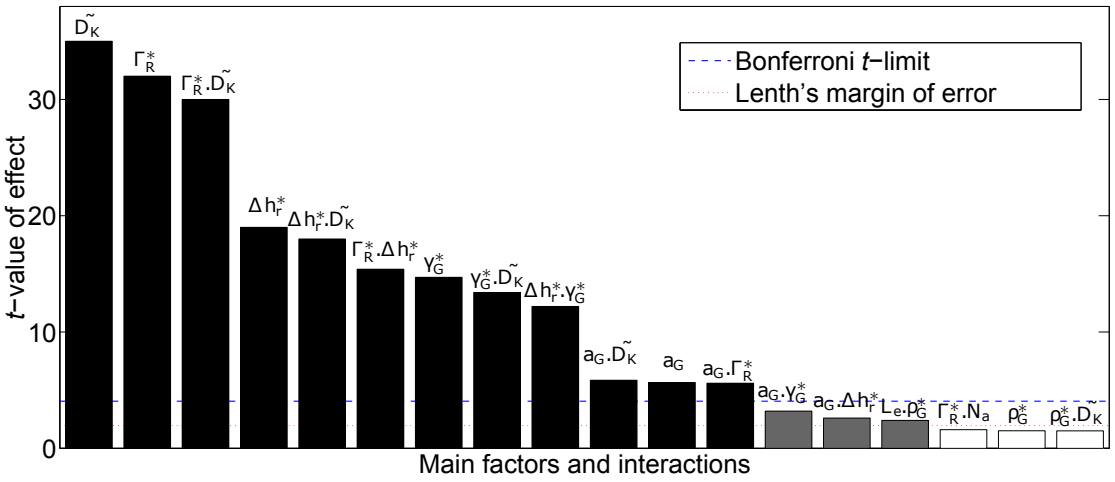

FIGURE 4.6: Pareto chart of the effects for the ratio of L_1 error between FIM and SSO-CKA. The t-values are computed with the residual obtained with the model formed of the twelve selected effects defined by Figure 4.5. Primary effects are represented in black, secondary in grey and insignificant effect in white.

This coupling is described by the heat of decomposition. Therefore, we define the total dimensionless heat of decomposition ΔH (see Equation A.10, Appendix A) by:

$$\Delta H = \Gamma_R^* \left(-\Delta h_r^* + a_G \left(\gamma_G^* - 1\right)\right) \tag{4.15}$$

and we study the evolution of the splitting error with ΔH for test cases 1 and 2 by arbitrarily increasing Δh_r^*. We first use a time-step strategy with a target time truncation error and a target maximum variable change $\eta = \eta' = 0.01$. We observe that for small ΔH, the L_1 error of SSO-CKA is only slightly larger than the one for FIM. However, for large ΔH, the ratio between the two errors can reach 2 for test case 1 and 4 for test case 2. To limit this error, we decrease η and η' to 0.05 for SSO-CKA. We observe that in both cases, the L_1 errors for SSO-CKA and FIM are now equivalent. SSO-CKA is particularly accurate for cases with small ΔH.

In conclusion, SSO-CKA generates a splitting error that is limited but in the general case, we need to reduce the target maximum time truncation error to obtain a discretization error of the same order as the one obtained for FIM, for example from 0.01 to 0.005.

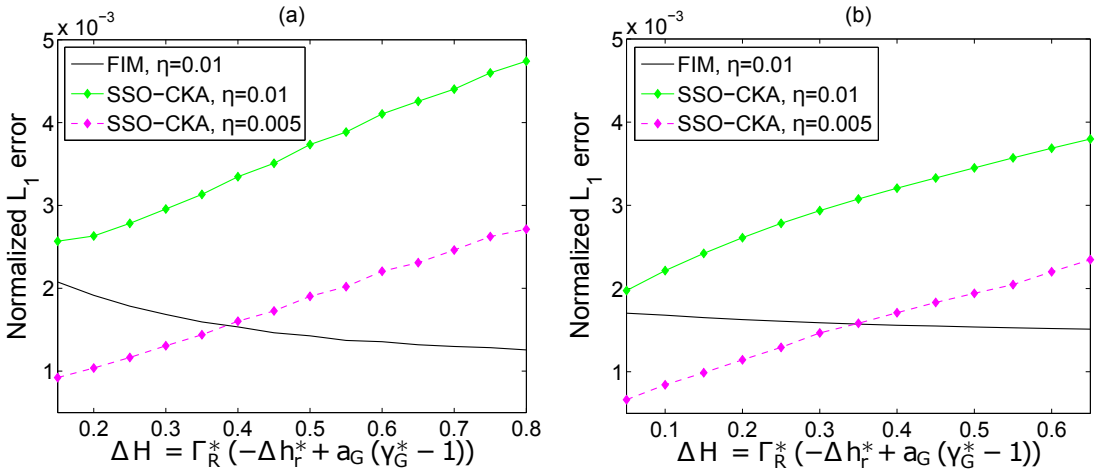

FIGURE 4.7: Evolution of L_1 error with total dimensionless heat of decomposition ΔH for (a) test case 1 and (b) test case 2 using FIM and SSO-CKA methods. We observe that the L_1 error for SSO-CKA is larger than the one for FIM, with a factor between 2 and 4. We then decreased η and η' from 0.01 to 0.005 for SSO-CKA and we obtain a L_1 error of the same order.

4.6 Summary

In this chapter, we evaluated the use of Operator Splitting (OS) method for the numerical simulation of a highly non-linear system: the thermal decomposition of solid reactant into non-reactive gas. We described the most common OS methods used in the literature and compared their convergence and precision for two test cases describing the conversion of kerogen. We observed that the Iterative Split Operator (ISO) failed to converge. The standard Sequential Split Operator (SSO) applied with first the advection operator followed by the chemical reaction (SSO-AK) provided a converged solution but gave a large pressure error. In the other direction (SSO-KA), it gave a large saturation error. The Strang-Marchuk Split Operator (SMSO) did not improve the result significantly.

To limit the splitting error of SSO, we developed a method that conserved the main interactions. First, the heat was transported by conduction (operator C). Then, the chemical reaction was solved (operator K). Finally the mass and heat convection were performed (operator A'). This method, defined as SSO-CKA, provided a converged solution for both test cases and generated less discretization error than the standard SSO and the SMSO method. However, the splitting error still needed to be controlled to avoid large discretization errors and instability.

We used DOE to study the precision of the method when applied to a large range of physical parameters. A time-stepping strategy based on time truncation error was applied to both FIM and SSO-CKA. We observed that the most important parameters for the precision of SSO-CKA were the extended Damköhler number $\tilde{D_K}$, the reduced volumetric heat capacity of the reactant Γ_R^* and the reduced heat of decomposition Δh_r^*. We defined the total dimensionless heat of decomposition ΔH (Equation 4.15) and we observed that for $\Delta H > 0.5$, the discretization error obtained with SSO-CKA could be four time larger than the discretization error obtained with FIM. To reduce the splitting error, we could divide the target time truncation error by a factor 2.0, but this strategy involved roughly twice as much computation.

The results of this chapter were obtained for a 1D model with one reaction where a solid reactant decomposes into gas. In Chapter 5, we develop a more complete mathematical model for the ISU of heavy oil and oil shale, and in Chapter 6, we verify that SSO-CKA is still the best splitting strategy for this model. We then explore the use of Runge-Kutta methods to reduce the discretization error without major additional computation.

Chapter 5

Scaling analysis of In-Situ Upgrading of bitumen and oil shale

This chapter investigates the In-Situ Upgrading of bitumen and oil shale by dimensionless analysis. The results of Chapters 2, 3 and 4 have been obtained for a simplified model where one solid component decomposes into non-reactive gas. However, kinetic models describing kerogen or bitumen decomposition can include a large number of reactions and a large number of components. These components can partition between solid, liquid and gas phases. Behar et al. [8] describes such a model for the heavy components of Safanya heavy oil (Saudi Arabia) and Al Darouich et al. [1] gives a similar model for the decomposition of the light components of the same oil. Regrouped together, we obtain a full kinetic model with 28 reactions and 26 components. For the decomposition of oil shale, Braun and Burnham [12] developed a model containing 83 species and 100 reactions.

This chapter has four objectives. First, we extend the model developed in Chapter 2 to a more complete mathematical model describing the ISU of heavy oil. The model is adapted from Fan et al. [24] and can describe ISU of both bitumen and oil shale. Secondly, we identify the full set of dimensionless numbers required to represent the process and compute their values for two test cases. Test case 1 describes the ISU of Athabasca bitumen and test case 2 describes the ISU of Green River oil shale. Thirdly,

we establish a range of values for each dimensionless group by first identifying a range of values for each dimensional parameter of the process from a thorough literature review. Finally, we use DOE to determine their effect on the energy efficiency of the process and extend the optimal heater temperature correlation obtained in Chapter 3 to the more complete mathematical model.

5.1 Mathematical model

The model contains an inert rock (I), with the pore-space occupied by n hydrocarbon components regrouped into three phases: gas (g), liquid (l) and solid (s). The solid phase is formed of kerogen and/or coke. We assume that the model contains k thermally unstable chemical entities which decompose with first-order kinetics. The decomposition of an entity X_i, $i = 1...k$, can be accounted for by one chemical reaction with one reactant:

$$X_i \xrightarrow{r_i} a_{i,1}X_1 + \ldots + a_{i,h}X_h + \ldots + a_{i,n}X_n \tag{5.1}$$

where r_i is the rate of reaction i and $a_{i,j}$ the mass stoichiometric coefficient for component j as a product ($a_{i,j} > 0$) or a reactant ($a_{i,j} < 0$). The rate of reaction is described using an Arrhenius law of order 1 [30]:

$$r_i = A_i \exp\left(-\frac{E_{ai}}{RT}\right) C_i \tag{5.2}$$

where A_i and E_{ai} are the frequency factor and the activation energy of reaction i, R is the universal gas constant and C_i is the mass concentration of the reactant X_i of reaction i.

The mass-balance equation for compositional simulation for each hydrocarbon component $j = 1...n$ can be expressed as follows [89]:

$$\frac{\partial}{\partial t}\left(\phi \sum_p \omega_{p,j}\rho_p S_p\right) = -\nabla\left(\sum_p \omega_{p,j}\rho_p v_p\right) + \sum_i a_{i,j} r_i \tag{5.3}$$

where ϕ is the rock porosity, S_p, ρ_p and v_p the saturation, mass density and velocity of phase p, $\omega_{p,j}$ the mass fraction of component j in phase p. The porosity of the rock

change with pressure due to compressibility:

$$\phi = \phi_0 \left(1 + c_{pv} \left(P - P_0\right)\right) \tag{5.4}$$

where ϕ_0 is the initial rock porosity and c_{pv} the pore volume compressibility. The density of the gas phase is given by the ideal gas law (Equation 2.12) with the total gas molecular weight:

$$m_{wg} = \sum_j \omega_{g,j} m_{wj} \tag{5.5}$$

The density of the liquid phase is given by:

$$\begin{aligned} \frac{1}{\rho_o} &= \sum_j \frac{\omega_{o,j}}{\rho_{o,j}} \\ \rho_{o,j} &= \rho_{o,j,0} \left(1 + c_j \left(P - P_0\right)\right) \left(1 - e_j \left(T - T_0\right)\right) \end{aligned} \tag{5.6}$$

where $\rho_{o,j,0}$, c_j and e_j are the component initial density, compressibility and thermal expansion in the liquid phase, respectively. We neglect the solid phase compressibility and thermal expansion, so that the solid density only depends on the phase composition:

$$\frac{1}{\rho_s} = \sum_j \frac{\omega_{s,j}}{\rho_{s,j}} \tag{5.7}$$

where $\rho_{s,j}$ is the component density in the solid phase. The velocity of phase p is given by Darcy's law:

$$v_p = -K \frac{k_{rp}}{\mu_p} \nabla \left(P - \rho_p g D\right) \tag{5.8}$$

where P is the pressure, g the gravitational constant, D the depth, K the rock permeability and $k_{r,p}$ and μ_p are the relative permeability and viscosity of phase p. The solid phase is immobile ($k_{rs} = 0$) and the gas-oil relative permeability is described by a Corey-type correlation [21] with a critical gas saturation of $S_{gc} = 0.05$, a residual oil saturation of $S_{or} = 0.2$ and Corey exponents equal to 2 for both oil and gas phases.

$$\begin{aligned} k_{ro} &= \left(\frac{S_o - S_{or}}{1 - S_{or} - S_{gc}}\right)^2 \\ k_{rg} &= \left(\frac{S_g - S_{gc}}{1 - S_{or} - S_{gc}}\right)^2 \end{aligned} \tag{5.9}$$

The impact of the solid saturation ($S_s = 1 - S_g - S_o$) on the permeability is given by a simple exponential relationship:

$$K = K_0 \exp\left(-\alpha \left(S_s - S_{s,0}\right)\right) \tag{5.10}$$

where K_0 is the initial permeability. The coefficient α determines how strongly the permeability varies with a change in solid saturation. Typically, α has a value between 5 and 10 [56]. Phase equilibrium is modelled using Wilson K-values [90]:

$$\begin{aligned} \xi_{g,j} &= K_j\left(P,T\right)\xi_{o,j} \\ K_j\left(P,T\right) &= \exp\left(5.373\left(1+A_{cj}\right)\left(1-\frac{T_{cj}}{T}\right)\right)\frac{P_{cj}}{P} \end{aligned} \tag{5.11}$$

where $\xi_{p,j}$ is the molar fraction of component j in phase p, A_{cj}, P_{cj} and T_{cj} are the component acentric factor, critical pressure and critical temperature, respectively. Heat transfer is accounted for in the overall energy balance equation [63]:

$$\frac{\partial}{\partial t}\left(\left(1-\phi\right)\rho_I u_I + \phi\sum_p \rho_p u_p S_p\right) = \nabla\left(\kappa\nabla T\right) - \nabla\left(\sum_p \rho_p v_p h_p\right) + \sum_i \Delta h_{ri} r_i \tag{5.12}$$

where ρ_I and u_I are the rock density and internal energy, u_p and h_p are the phase internal energy and enthalpy, κ is the thermal conductivity of the system and Δh_{ri} is the enthalpy of reaction i.

5.2 Test cases

We consider two test cases, one representing the ISU of Athabasca tar-sand (test case 1), and one representing the ISU of Green River oil shale (test case 2). These test cases are similar in the sense that they describe the decomposition of one primary reactant R (bitumen compound NSO for test case 1 and kerogen K for test case 2) into heavy, medium and light hydrocarbon components, with secondary decomposition for the heavy and medium components. Apart from different values for the reaction parameters, the main difference is in the initial phase saturations. For tar-sand, the pore-space is initially filled with very viscous liquid. The rock permeability is high but the initial mobility of the fluid is low. However, when the temperature increases, the viscosity decreases rapidly leading to a small oil production rate. For oil shale, the pore-space is initially

85% filled with a solid phase and remains like this until the chemical reactions become important. There is no initial oil production. The initial permeability is very low and most of the hydrocarbon is immobile. Therefore, these two test cases have similar kinetic models but very different flow behaviour.

For both test cases, we consider a 3D reservoir represented by a cube with a simplified heater pattern formed by four heaters, one on each vertical side of the cube, and one producer well at the centre (Fig. 5.1). Each side of the cube is 10 m long. The heaters operate at a constant temperature of 350^oC and the producer at a constant Bottom Hole Pressure (BHP) equal to the initial pressure of the reservoir. To solve the system of equations, we developed a C++ simulator called EXTEND (EXtended Thermal simulator for Evaluating new Numerical Discretization). The source code of EXTEND is provided in the CD-ROM attached to this thesis. The numerical methods used in the software are detailed in Appendix B. In this chapter, we use the Fully Implicit method with a $11 \times 11 \times 1$ grid.

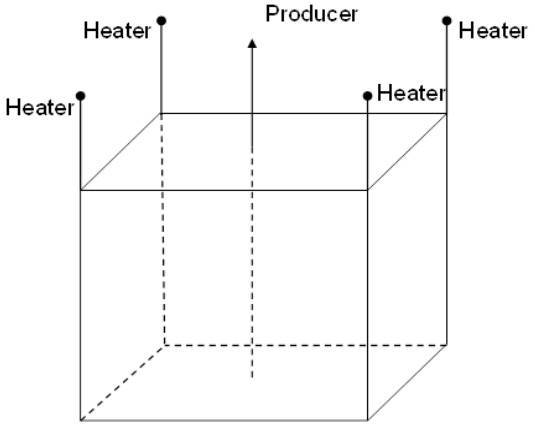

FIGURE 5.1: Reservoir geometries and wells

5.2.1 Athabasca bitumen test case

For this case, the pore space is initially filled with very viscous bitumen. The rock and initial properties are summarized in Table 5.1. The porosity and permeability are high (0.36 and 4158 mD respectively) but the initial viscosity of the liquid phase is also large (150000 cp). As the temperature increases inside the reservoir, the viscosity of the oil decreases following the correlation [3]:

$$\ln\left(\ln \mu_o\right) = -3.5912 \ln T + 22.976 \tag{5.13}$$

where μ_o is the oil viscosity in centipoise (cp). For the viscosity of the gas, we use the same simple correlation as the one used in CMG STARS [19]:

$$\mu_g = 0.0136 + 3.8 \times 10^{-5} (T - 273.15) \tag{5.14}$$

where μ_g is in cp, and T is in K. The bitumen decomposition is modelled using a kinetic scheme adapted from Behar et al. [8] and Al Darouich et al. [1]. The reactions and components are lumped into a model with $k = 3$ reactions and $n = 6$ components. The reaction enthalpies have been neglected here. The thermodynamic properties of the components are summarized in Table 5.3

	Test case 1
Initial Porosity	0.36
Initial Permeability	4158 mD
Coefficient α	6.28
Initial reactant saturation	0.9
Rock volumetric heat capacity	1800 $kJ/m^3/K$
Heat conductivity	1.7 $W/(mK)$
Rock compressibility	5×10^{-3} $1/MPa$
Initial pressure	1.5 MPa
Initial temperature	28 ^oC

TABLE 5.1: Rock and initial properties for test case 1. These data are adapted from [49].

Reaction	A (s^{-1})	E_a (kJ/mol)	Δh_r (kJ/kg)
NSO $\longrightarrow$ 0.170 C_{14+} + 0.105 C_{6-13} + 0.079 C_1-C_4+0.051 H_2S-CO_2 + 0.595 PreChar	7.82×10^{12}	209.2	0
$C_{14+} \longrightarrow$ 0.48 C_{6-13} + 0.248 C_1-C_4 +0.272 PreChar	3.85×10^{16}	259.4	0
$C_{6-13} \longrightarrow$ 0.767 C_1-C_4 +0.233 PreChar	3.85×10^{16}	276.1	0

TABLE 5.2: Chemical reactions for test case 1. These data are adapted from [8].

5.2.2 Green river oil shale test case

For this case, the pore space is initially filled with solid kerogen (S_s=0.85) and CO_2 gas (S_g=0.15). The rock properties are summarized in Table 5.4. The rock porosity is equal to 0.2 but as the solid is immobile, the apparent porosity for the fluid is equal to

	NSO	C_{14+}	C_{6-13}	C_1-C_4	H_2S-CO_2	PreChar
Molecular weight $(kg/kmol)$	515	500	160.0	40	80	12.72
Critical pressure (MPa)	0.6	0.6	2.1	4.2	4.0	NA
Critical temperature (K)	1200	950	670	370	350	NA
Acentric factor (no unit)	1.6	1.5	0.53	0.151	0.1	NA
Liquid density at standard condition (kg/m^3)	1070	940	800	400	400	NA
Liquid compressibility $(1/MPa \times 10^{-3})$	5.4	5.4	5.4	5.4	5.4	NA
Liquid thermal expansion $(1/K \times 10^{-4})$	6.3	6.3	6.3	6.3	6.3	NA
Solid density (kg/m^3)	NA	NA	NA	NA	NA	1200
Specific heat capacity $(kJ/kg/K)$	1.5	1.5	2.0	2.5	2.5	1.0
Initial mass composition	0.57	0.41	0.02	0	0	0

TABLE 5.3: Component thermodynamic properties for test case 1.

$0.2 \times (1 - 0.85) = 0.03$. The initial permeability is also very low (2 mD). The viscosity of the gas is given by Equation 5.14 and the viscosity of the liquid phase is given by [62]:

$$\log_{10} \mu_o(T) = \frac{4.1228}{\left(1 + \frac{T-303.15}{303.15}\right)^{3.564}} - 0.002 \tag{5.15}$$

where μ_o is in cp and T in K. As the temperature increases, the kerogen decomposes into liquid and gas products and the apparent porosity and permeability increase. We used a simplified kinetic model adapted from Braun and Burnham [12] and described in Fan et al. [24]. This model includes $k = 3$ reactions and $n = 6$ components. The thermodynamic properties of the components are summarized in Table 5.6.

	Test case 1
Initial Porosity	0.2
Initial Permeability	2 mD
Coefficient α	6.28
Initial solid saturation	0.85
Rock volumetric heat capacity	1800 $kJ/m^3/K$
Heat conductivity	2 $W/(mK)$
Rock compressibility	4.35×10^{-4} $1/MPa$
Initial pressure	0.69 MPa
Initial temperature	16.7 ^oC

TABLE 5.4: Rock and initial properties for test case 2. These data are adapted from [24] and [56].

Reaction	A (s^{-1})	E_a (kJ/mol)	Δh_r (kJ/kg)
$K \longrightarrow 0.280\ IC_{37} + 0.200\ IC_{13}$ $+ 0.090\ IC_2 0.015\ CO_2 +$ $+ 0.415$ PreChar	4.33×10^7	161.6	0
$IC_{37} \longrightarrow 0.090\ IC_{13} + 0.170\ IC_2$ $+0.740$ PreChar	7.23×10^{11}	206.0	0
$IC_{13} \longrightarrow 0.200\ IC_2 + 0.800$ PreChar	1.14×10^{12}	219.3	0

TABLE 5.5: Chemical reactions for test case 2. These data are adapted from [24].

	IC_{37}	IC_{13}	IC_2	CO_2	K	Prechar
Molecular weight $(kg/kmol)$	465.83	169.52	30.07	44.01	15	12.72
Critical pressure (MPa)	0.94	2.4	4.6	7.4	NA	NA
Critical temperature (K)	962.28	715.36	288.74	298.53	NA	NA
Acentric factor (no unit)	0.818	0.365	0.008	0.239	NA	NA
Liquid density at standard condition (kg/m^3)	1013	760	400	400	NA	NA
Liquid compressibility $(1/MPa \times 10^{-3})$	5.4	5.4	5.4	5.4	NA	NA
Liquid thermal expansion $(1/K \times 10^{-4})$	6.3	6.3	6.3	6.3	NA	NA
Solid density (kg/m^3)	NA	NA	NA	NA	1200	1200
Specific heat capacity $(kJ/kg/K)$	1.5	2.0	2.5	2.5	1.0	1.0
Initial mass composition	0	0	0	0.001	0.999	0

TABLE 5.6: Component thermodynamic properties for test case 2.

5.3 Dimensionless Analysis

5.3.1 Identification of the dimensionless numbers

We use Inspectional Analysis to identify the set of dimensionless numbers that fully represent our mathematical model. This technique is described in Appendix A and has been applied to a simplified model describing the thermal decomposition of solid reactant into non-reactive gas in Chapter 2. As for the simplified model, the reference time scale of the process is the time scale of heat conduction in the rock τ (Equation 2.24).

Table 5.7 shows the numbers describing the heat and mass flow. The pressure Lewis number L_e, the reduced volumetric capacity of the primary reactant Γ_R^*, the reduced initial temperature T_0^*, the initial saturation of reactant $S_{R,0}$, the permeability function

parameter α and the reduced gas viscosity variation have been defined in Chapter 2 (Table 2.2) for a simplified model with no liquid phase.

TABLE 5.7: General heat and mass flow scaling groups for ISU.

Name	Notation	Definition	Description
Pressure Lewis number	L_e	$\frac{\phi_0 \mu_{g,0} \kappa_s}{K_0 P_0 (1-\phi_0) \rho_I \gamma_I}$	$\frac{\text{heat diffusivity}}{\text{pressure diffusivity}}$
Oil gas viscosity ratio	M	$\frac{\mu_o}{\mu_g}$	$\frac{\text{oil viscosity}}{\text{gas viscosity}}$
Reduced primary reactant volumetric heat capacity	Γ_R^*	$\frac{\phi_0 \rho_{R,0} \gamma_R}{(1-\phi_0) \rho_I \gamma_I}$	$\frac{R \text{ volumetric heat capacity}}{\text{inert solid heat capacity}}$
Reduced initial temperature	T_0^*	$\frac{T_0}{\Delta T}$	$\frac{\text{initial temperature}}{\text{variation of temperature}}$
Initial saturation of reactant (solid or liquid)	$S_{R,0}$		
Permeability function parameter	α		
Reduced gas viscosity variation	$\delta\mu_g^*$	$\frac{\delta \mu_g \Delta T}{\mu_{g,0}}$	$\frac{\text{variation of gas viscosity}}{\text{initial gas viscosity}}$
Reduced pore volume compressibility	c_{pv}^*	$c_{pv} P_0$	

L_e quantifies the ratio of heat diffusivity to pressure diffusivity in the gas phase. The ratio of heat diffusivity to pressure diffusivity in the oil phase is described by the quantity ML_e, where M is the oil gas viscosity ratio. Since M varies with temperature, we define M_0 the initial viscosity ratio and M_H the viscosity ratio at heater temperature. The last number is the reduced pore volume compressibility c_{pv}^* which describes the pore volume variation with change of pressure. Table 5.8 gives the values of these numbers for test cases 1 and 2.

TABLE 5.8: Values of general heat and mass flow scaling groups for test cases 1 and 2.

	Test case 1	Test case 2
L_e	1.3×10^{-6}	2.9×10^{-3}
Γ_R	0.5	0.17
M_0	10^7	4.8×10^6
M_H	89	77
T_0^*	0.94	0.87
$S_{R,0}$	0.9	0.85
α	6.28	6.28
$\delta\mu_g^*$	0.83	0.89
c_{pv}^*	7.5×10^{-3}	3×10^{-4}

Each reaction $i = 1...k$ is described by three dimensionless numbers: the extended Damköhler number $\tilde{D_{Ki}}$, the Arrhenius number N_{ai} and the reduced reaction enthalpy

Δh^*_{ri}, plus n stoichiometric coefficients (Table 5.9). These numbers have been described in Chapter 2 (Table 2.2 and Equation 2.35) for a model with one reaction. The Damköhler number D_K quantifies the ratio of chemical rate to heat conduction rate at infinite temperature. However, we observed in Chapter 2 that the process is better represented by the extended Damköhler numbers $\tilde{D_K}$ which considers the rate at the heater temperature. For each reaction, the Arrhenius numbers N_{ai} describes the energy barrier to the reaction and the reduced reaction enthalpy Δh^*_{ri} quantifies the ratio of heat consumed by that chemical reaction to heat stored in the reactant. Table 5.10 gives the values of these numbers for test cases 1 and 2.

TABLE 5.9: Chemical reaction scaling groups for each reaction $i = 1..k$.

Name	Notation	Definition	Description
Extended Damköhler number	$\tilde{D_{Ki}}$	$A_i \exp\left(\frac{-E_{ai}}{RT_H}\right)\tau$	$\frac{\text{reaction rate at } \infty \text{ temp}}{\text{heat diffusion rate}}$
Arrhenius number	N_{ai}	$\frac{E_{ai}}{R\Delta T}$	$\frac{\text{activation energy}}{\text{potential energy}}$
Reduced reaction enthalpy	Δh^*_{ri}	$-\frac{\Delta h_{ri}}{\gamma_R \Delta T}$	$\frac{\text{energy consumed}}{\text{energy stored}}$
Stoichiometric coefficients	$a_{i,1}...a_{i,n}$		

TABLE 5.10: Values of chemical reaction scaling groups for test cases 1 and 2.

	Test case 1			Test case 2		
Reaction	1	2	3	1	2	3
$\tilde{D_{Ki}}$	1540	470	19	90	280	34.0
N_{ai}	78.1	96.9	103.13	58.3	74.3	79.1
Δh^*_{ri}	0	0	0	0	0	0

Finally, for each component $j = 1...n$, the thermodynamic properties are described by eight dimensionless numbers for liquid and gas components and two for solid components. They are presented in Tables 5.11 and 5.12, and their values for test cases 1 and 2 are given in Tables 5.13 and 5.14, respectively

5.3.2 Range of values for the dimensionless numbers

To establish the range of values for the dimensionless numbers, we first need to establish the range of values for the various parameters of the ISU process. They have been selected from a thorough literature review. For the rock and initial properties, we used papers describing numerical simulation of oil shale or bitumen recovery process [24, 49, 52, 57]. For the chemical reaction properties, we reviewed Braun et al. [12],

TABLE 5.11: Thermodynamic properties scaling groups for each fluid component $j = 1..n_f$.

Name	Notation	Definition
Reduced gas density	$\rho^*_{g,j}$	$\frac{m_{wj}P_0}{RT_0\rho_{R,0}}$
Reduced oil density	$\rho^*_{o,j}$	$\frac{\rho_{o,j}}{\rho_{R,0}}$
Reduced compressibility	c^*_j	c_jP_0
Reduced thermal expansion	e^*_j	$e_j\Delta T$
Acentric factor	A_{cj}	
Reduced critical pressure	P^*_{cj}	$\frac{P_{cj}}{P_0}$
Reduced critical temperature	T^*_{cj}	$\frac{T_{cj}}{T_0}$
Reduced specific heat capacity	γ^*_j	$\frac{\gamma_j}{\gamma_R}$

TABLE 5.12: Thermodynamic properties scaling groups for each solid component $j = 1..n_s$.

Name	Notation	Definition
Reduced solid density	$\rho^*_{s,j}$	$\frac{\rho_{s,j}}{\rho_{R,0}}$
Reduced specific heat capacity	γ^*_j	$\frac{\gamma_j}{\gamma_R}$

TABLE 5.13: Values of thermodynamic properties scaling groups for each component for test case 1.

	NSO	C_{14+}	C_{6-13}	C_1-C_4	H_2S-CO_2	PreChar
$\rho^*_{g,j}$	0.29	0.28	0.09	0.02	0.04	NA
$\rho^*_{o,j}$	1	0.88	0.75	0.37	0.37	NA
c^*_j	0.008	0.008	0.008	0.008	0.008	NA
e^*_j	0.20	0.20	0.20	0.20	0.20	NA
$\rho^*_{s,j}$	NA	NA	NA	NA	NA	1.12
γ^*_j	1	1	1.33	1.67	1.67	0.67
A_{cj}	1.6	1.5	0.53	0.151	0.1	NA
P^*_{cj}	0.4	0.4	1.4	2.8	2.67	NA
T^*_{cj}	3.98	3.15	2.22	1.23	1.16	NA

Behar et al. [8] and Phillips et al. [67]. Finally, we used Perry's Handbook [66] for the thermodynamic properties of the components. Table 5.15 shows the range obtained for each parameter.

In reality, data for component or chemical reaction properties are not independent, but here they are assumed to be in order to define the range of dimensionless groups. Dependencies between parameters should be explored in future work as this may reduce the set of primary numbers obtained from the analysis. Assuming they are independent, we obtain a range of values for each dimensionless group. They are given in Table 5.16.

TABLE 5.14: Values of thermodynamic properties scaling groups for each component for test case 2.

	IC_{37}	IC_{13}	IC_2	CO_2	K	PreChar
$\rho^*_{g,j}$	0.111	0.040	0.007	0.011	NA	NA
$\rho^*_{o,j}$	0.84	0.63	0.33	0.33	NA	NA
c^*_j	0.004	0.004	0.004	0.004	NA	NA
e^*_j	0.21	0.21	0.21	0.21	0.21	NA
$\rho^*_{s,j}$	NA	NA	NA	NA	1	1
γ^*_j	1.5	2	2.5	2.5	1	1
A_{cj}	0.818	0.365	0.008	0.239	NA	NA
P^*_{cj}	1.36	3.48	6.67	10.7	NA	NA
T^*_{cj}	3.32	2.47	1.0	1.03	NA	NA

TABLE 5.15: Range of values for the various parameters of the ISU process.

Property	min	max	Property	min	max
L (m)	10	15	ϕ	0.1	0.4
K_0 (mD)	1	5000	α	5	10
ρ_I (kg/m^3)	2000	2200	γ_I $(J/(kgK))$	900	1500
m_{wg} (kg/mol)	0.03	0.3	m_{wo} (kg/mol)	0.1	0.515
κ_s $(W/(mK))$	1	3	$S_{R,0}$	0.8	0.9
$r_i(T_H)$ (s^{-1})	10^{-9}	3×10^{-5}	E_{ai}(J/mol)	1.60×10^5	2.8×10^5
Δh_{ri} (J/kg)	0	1×10^6	a_{ij}	0	0.8
ρ_R (kg/m^3)	1000	1500	γ_R $(J/(kgK))$	1000	1500
$\rho_{o,j}$ (kg/m^3)	400	1070	$\rho_{s,j}$ (kg/m^3)	1000	1500
c_j $(1/Pa)$	10^{-9}	6×10^{-9}	e_j $(1/K)$	4×10^{-4}	10^{-3}
γ_j $(J/(kgK))$	1000	2500	A_{cj}	0.008	1.6
P_{cj} (Pa)	6×10^5	8×10^6	T_{cj} (K)	280	1200
$\mu_{g,0}$ $(Pa.s)$	1×10^{-5}	2×10^{-5}	$\delta\mu_g$ $(Pa.s/K)$	2×10^{-8}	3×10^{-8}
$\mu_{o,0}$ $(Pa.s)$	10	1000	$\mu_{o,H}$ $(Pa.s)$	2×10^{-3}	3×10^{-3}
T_H (^0C)	300	400	T_0 (^0C)	10	40
P_0 (Pa)	5×10^5	5×10^6	c_{pv} $(1/P_a)$	4×10^{-10}	5×10^{-9}

The extended Damköhler numbers and the pressure Lewis number are the numbers that vary the most, over a range of five order of magnitude. For small $\tilde{D_{Ki}} \approx 0.04$, the chemical reaction is very slow everywhere in the reservoir, which suggests that the heater temperature is too small. For large $\tilde{D_{Ki}} \approx 2.0 \times 10^4$, the reaction is very fast when the temperature gets near the heater temperature, which suggests that T_H could have been set to a lower value. For the pressure Lewis number, small values $L_e \approx 1.4 \times 10^{-8}$ correspond to domain with large porosity (tar-sand) and large values $L_e \approx 4.5 \times 10^{-2}$ correspond to domain with a low porosity (oil shale).

TABLE 5.16: Range of values for the dimensionless numbers of the ISU process.

Group	min	max	Group	min	max
L_e	1.4×10^{-8}	4.5×10^{-2}	Γ_R^*	0.03	0.83
M_0	5×10^5	1×10^8	M_H	67	197
T_0^*	0.73	1.2	$S_{R,0}$	0.8	0.9
$\delta\mu_g^*$	0.26	1.17	α	5	10
c_{pv}	2×10^{-4}	2.5×10^{-2}	$\tilde{D_{Ki}}$	0.04	2.0×10^4
N_{ai}	50	130	Δh_{ri}^*	0	4.0
a_{ij}	0	0.8	$\rho_{g,j}^*$	4×10^{-3}	0.64
$\rho_{o,j}^*$	0.27	1.1	c_j^*	5×10^{-4}	0.03
e_j^*	0.1	0.4	$\rho_{s,j}^*$	0.67	1.5
γ_j^*	0.67	2.5	A_c	0.008	1.6
P_c^*	0.12	16	T_{cj}^*	0.89	4.2

5.4 Sensitivity analysis

In order to identify the most important parameters for the energy efficiency of the process, we perform a sensitivity analysis using DOE. The number of dimensionless groups increases rapidly with the numbers of reactions and components. For a model including k reactions, n_f fluid components and n_s solid components, each reaction gives 3 additional groups plus $n_f + n_s$ stoichiometric coefficients (Table 5.9). Since $a_{i,i} = -1$ and $\sum_j a_{ij} = 0$, the number of independent stoichiometric coefficients for each reaction is $n_f + n_s - 2$. Each fluid components gives 8 additional groups (Table 5.11) and each solid component gives 2 additional groups (Table 5.12). The model also depends on 9 general heat and mass flow numbers (Table 5.7). Therefore, the total number of dimensionless number is equal to $9 + k(3 + n_f + n_s - 2) + 8n_f + 2n_s$.

For test case 1 which includes three reactions, five fluid components and one solid component, this amounts to 72 dimensionless numbers. For test case 2 which includes three reactions, four fluid components and two solid components, this amounts to 66 dimensionless numbers. A sensitivity analysis with DOE for such a large number of parameters would result in an impractical amount of computation.

To conduct this sensitivity analysis, we first restrict ourselves to a model with one reaction and four components. Then, we study the evolution of the production profile for test cases 1 and 2 when changing the Damköhler numbers, and finally we identify the optimal heater temperature for the process as a function of these Damköhler numbers.

5.4.1 DOE

We consider a simplified model with one reaction:

$$K \longrightarrow O + G + C \tag{5.16}$$

where K is the kerogen, O an oil component, G a gas component and C the solid charred residual. This chemical reaction gives five dimensionless groups ($\tilde{D_K}$, Na, Δh_r^*, a_G and a_o). To simplify further the problem, we assume that the oil and gas components are immiscible. In this case, the component O gives four groups (ρ_O^*, c_O^*, e_O^* and γ_O^*) and the component G gives two groups (ρ_G^* and γ_G^*). The kerogen and solid residual each give two groups ($\rho_{s,j}^*$ and γ_j^*) but since K is the primary reactant, $\rho_{s,K}^* = 1$ and $\gamma_K^* = 1$. Therefore, this simplified model has 22 dimensionless groups. They are summarized in Table 5.17 with their minimum and maximum values extracted from Table 5.16.

TABLE 5.17: Range of values for the dimensionless numbers for the DOE.

Group	min	max	Group	min	max
L_e	1.4×10^{-8}	4.5×10^{-2}	Γ_R^*	0.03	0.83
M_0	5×10^5	1×10^8	M_H	67	197
T_0^*	0.73	1.2	$S_{R,0}$	0.8	0.9
$\delta\mu_g^*$	0.26	1.17	α	5	10
c_{pv}	2×10^{-4}	2.5×10^{-2}	$\tilde{D_K}$	0.04	2.0×10^4
N_a	50	130	Δh_r^*	0	4.0
a_O	0.3	0.5	a_G	0.1	0.3
$\rho_{g,j}^*$	4×10^{-3}	0.64	ρ_o^*	0.27	1.1
c_O^*	5×10^{-4}	0.03	e_O^*	0.1	0.4
ρ_C^*	0.67	1.5	γ_G^*	1.33	2.5
γ_O^*	0.67	1.5	γ_C^*	0.67	1.5

We consider the EROI after 2τ (Equation 2.24) as a response describing the energy efficiency of the process. We use a first-order model with interactions and a two-level fractional factorial design of resolution V [65]. This design has been described in Chapter 3. Figure 5.2 shows the half-normal plot of effects. We observe that nine effects show a large deviation from the half-normal distribution. Figure 5.3 shows a Pareto chart including the twenty most important effects.

The t-values are computed with the residual obtained with the model formed of the nine selected effects defined by Figure 5.2. The effects are compared with the Bonferroni

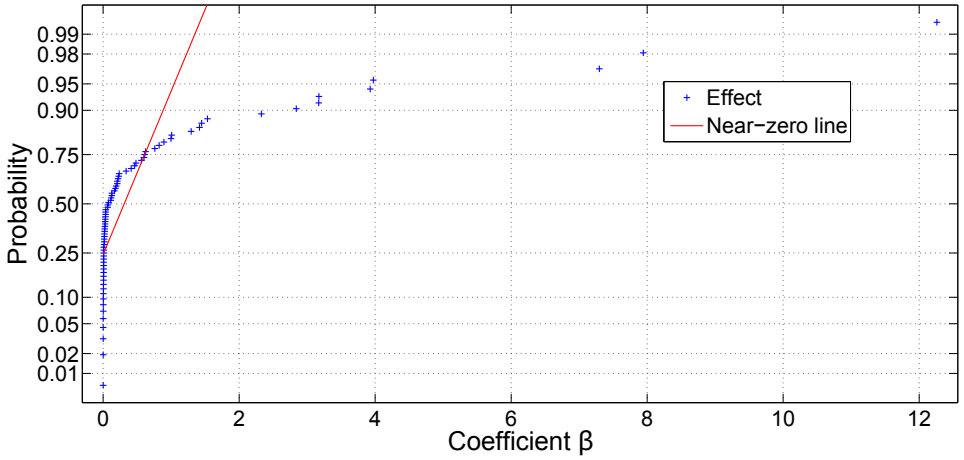

FIGURE 5.2: Half-normal plot of the effects for the EROI of the ISU process. We observe that nine effects show a large deviation from the half-normal distribution.

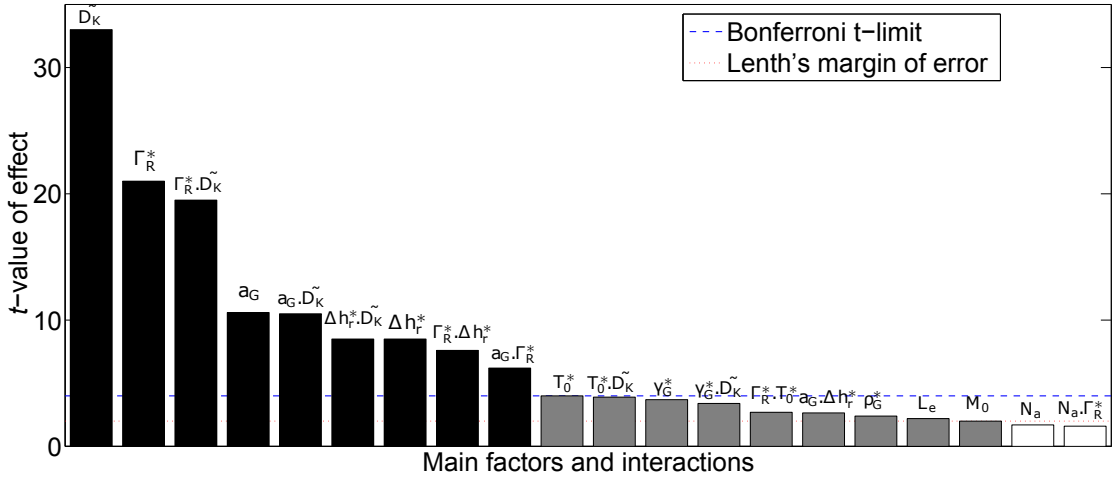

FIGURE 5.3: Pareto chart of the effects for the EROI of the ISU process. The t-values are computed with the residual obtained with the model formed of the nine selected effects defined by Figure 5.2. The effect are compared with the Bonferroni t-limit and the Lenth's margin of error. Primary effects are represented in black, secondary in grey and insignificant effect in white.

t-limit and the Lenth's margin of error (see Chapter 3, Equations 3.19 and 3.20). We obtain the following classification of the dimensionless groups:

- primary numbers: $\tilde{D_K}$, Γ_R^*, a_G and Δh_r^*
- secondary numbers: T_0^*, γ_G^*, ρ_G^*, L_e and M_0
- insignificant numbers: N_a, a_O, α, c_{pv}^*, M_1, $S_{R,0}$, ρ_O^*, c_O^*, e_O^*, γ_O^*, ρ_C^*, γ_C^* and $\delta\mu_g^*$

We observe many similarities with the results of the analysis conducted in Chapter 3, section 3.3.1. The most important numbers are the extended Damköhler number $\tilde{D_K}$,

the reduce volumetric heat capacity of the reactant Γ_R^*, the gas stoichiometric coefficient a_G and the reduced reaction enthalpies Δh_r^*. Therefore, it is essential to define these parameters accurately.

$\tilde{D_K}$ depends on the pre-exponential factor A and the activation energy E_a. For test case 1, the decomposition of NSO has a pre-exponential factor $A_1 = 7.82 \times 10^{12}\ s^{-1}$, an activation energy $E_{a1} = 209.2\ kJ/mol$, and an extended Damköhler number $\tilde{D_{K1}} = 1540$. Increasing the pre-exponential factor by 1% increases $\tilde{D_{K1}}$ by 1%. However, because of the exponential form of Arrhenius law (Equation 5.2), increasing the activation energy by 1% decreases $\tilde{D_{K1}}$ by 33%. So a special effort should be made in the laboratory to measure the activation energies accurately.

Also, the reaction enthalpies have been neglected in test cases 1 and 2, but Δh_r^* is an important parameter for the energy efficiency of the process. Therefore, the reaction enthalpies can only be neglected if $\Delta h_r^* << 1$, which correspond roughly to $\Delta h_r \lesssim 10$ kJ/kg. Phillips et al. [67] obtained values from 25 to 2500 kJ/kg. We conclude that Δh_r^* should not be neglected.

5.4.2 Variability of production profile with Damköhler numbers

For test cases 1 and 2, we have three Damköhler numbers, one for each reaction. We now study the evolution of the production profile for test cases 1 and 2 when successively changing the Damköhler numbers. Figures 5.4 and 5.5 show the reservoir temperature and saturation distribution after 800 days for test case 1 and 2, respectively. At this time, nearly half of the primary reactant has been converted. Near the heaters, the temperature is very large and light oil and gas products appear. They are transported toward the production well in the centre. We observe for Athabasca bitumen (test case 1) four zones where the gas saturation is very low. They correspond to areas of the domain where the temperature and the velocity are both small. The bitumen liquid phase is immobile in these zones and the gas does not flow through them. For Green River oil shale (test case 2), the primary reactant is solid, and liquid and gas components are products of the reaction. Their viscosity is relatively small compared to the viscosity of bitumen. Therefore, the gas saturation mostly depends on temperature and we do not observe those four low gas saturation zones.

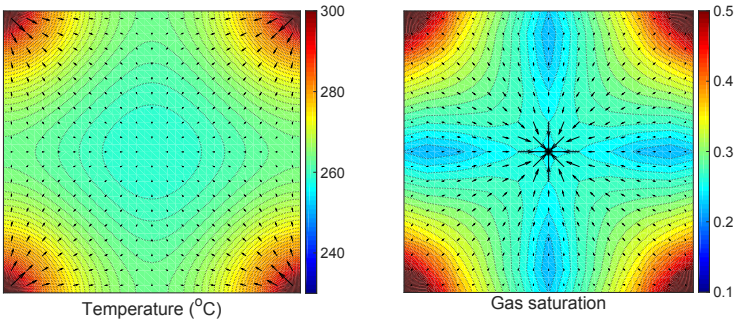

FIGURE 5.4: Top view of reservoir temperature and saturation distribution for test case 1 after 800 days. The isosurfaces are represented in dotted line. The arrows on the temperature map represent the heat conduction field and the ones on the gas saturation map represent the total velocity field. Near the heaters, the temperature is very high and light oil and gas products appear. They flow toward the producer well. Four low gas saturation zone appear where the temperature and the velocity are both small.

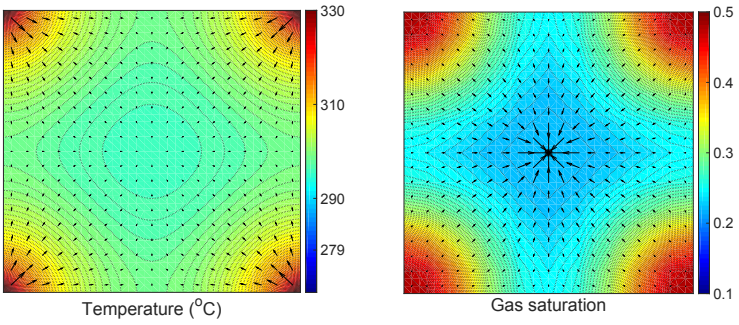

FIGURE 5.5: Top view of reservoir temperature and saturation distribution for test case 2 after 800 days. The isosurfaces are represented in dotted line. The arrows on the temperature map represent the heat conduction field and the ones on the gas saturation map represent the total velocity field. Near the heaters, the temperature is very high and light oil and gas products appear. They flow toward the producer well

For test case 1, the values of the extended Damköhler numbers for the three reactions were initially $\tilde{D_{K1}} = 1540$, $\tilde{D_{K2}} = 470$ and $\tilde{D_{K3}} = 19$ (Table 5.10). Figure 5.6 shows the hydrocarbon production profile. Initially, we produce essentially liquid oil with low API^o. As the temperature increases, the chemical reactions become important, the API^o increases and we start producing gas. Since light oil and gas are more valuable products, the EROI of the process increases significantly (Figure 5.6d).

For test case 2, the values for the three reactions were initially $\tilde{D_{K1}} = 90$, $\tilde{D_{K2}} = 280$ and $\tilde{D_{K3}} = 34$ (Table 5.10). Figure 5.7 shows the hydrocarbon production profiles. Initially, there is almost no production. As the temperature increases, the chemical reactions become significant and light components appear. The lighter components travel rapidly

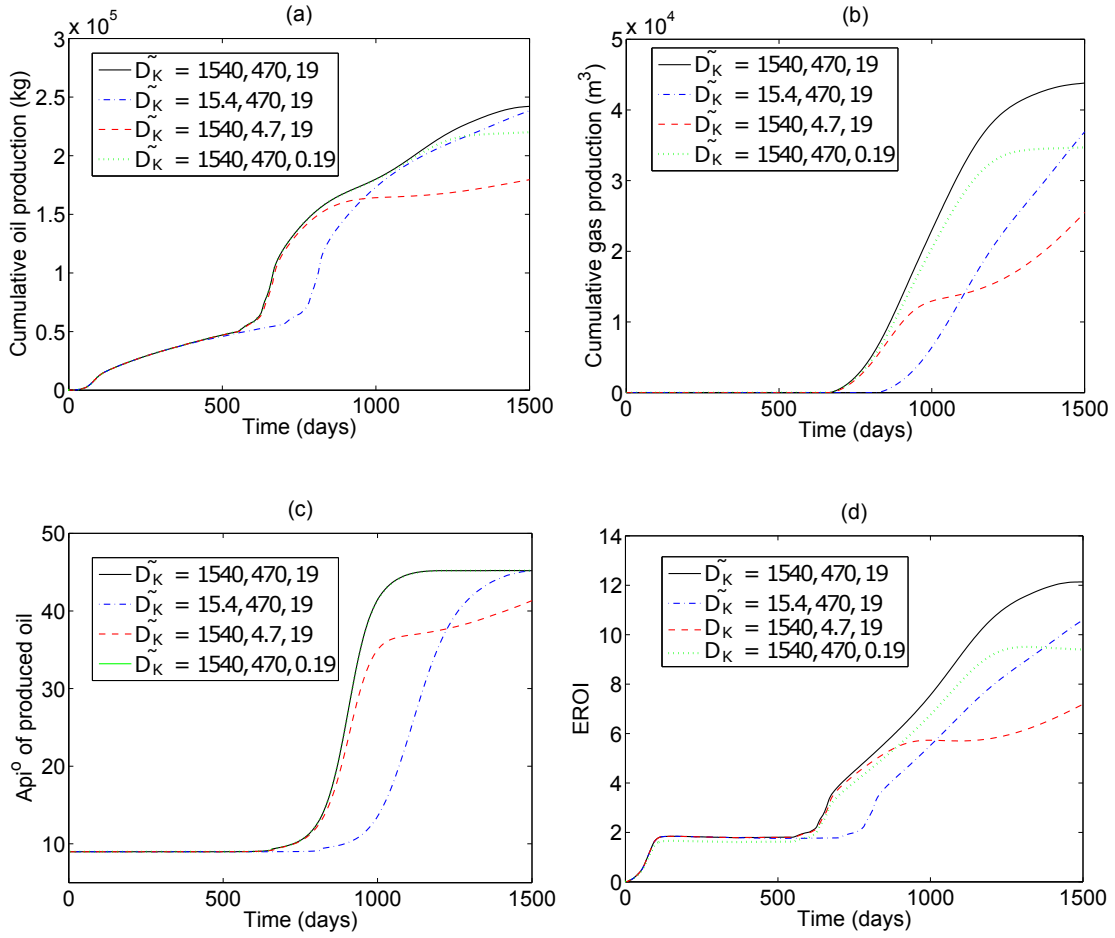

FIGURE 5.6: Variation of hydrocarbon production profile with Damköhler numbers for test case 1.

to the producer well, so we start producing gas and light oil with API$^o \approx$ 45 (Figure 5.7c). Later, some of the heavier hydrocarbon components reaches the well and the API^o decreases rapidly. Finally, as the last reaction appears, medium oil is converted to gas and the API^o increases again. Since light oil and gas are more valuable products, the EROI of the process increases significantly. (Figure 5.7d).

We then change successively the values of the extended Damköhler numbers. Since the values of the D_{Ki} for test cases 1 and 2 are in the upper part of the range defined in Table 5.16, we divide the pre-exponential factors A_i by 100. This gives low values for $\tilde{D_{Ki}}$ but still inside the range defined in Table 5.16.

For test case 1, we observe that reducing $\tilde{D_{K1}}$ delays the production of light oil and gas. However, when the second and third reactions appear, the production of oil and gas and the API ^{o} of the produced oil increase rapidly. Thus, reducing $\tilde{D_{K1}}$ from 1540 to 15.4

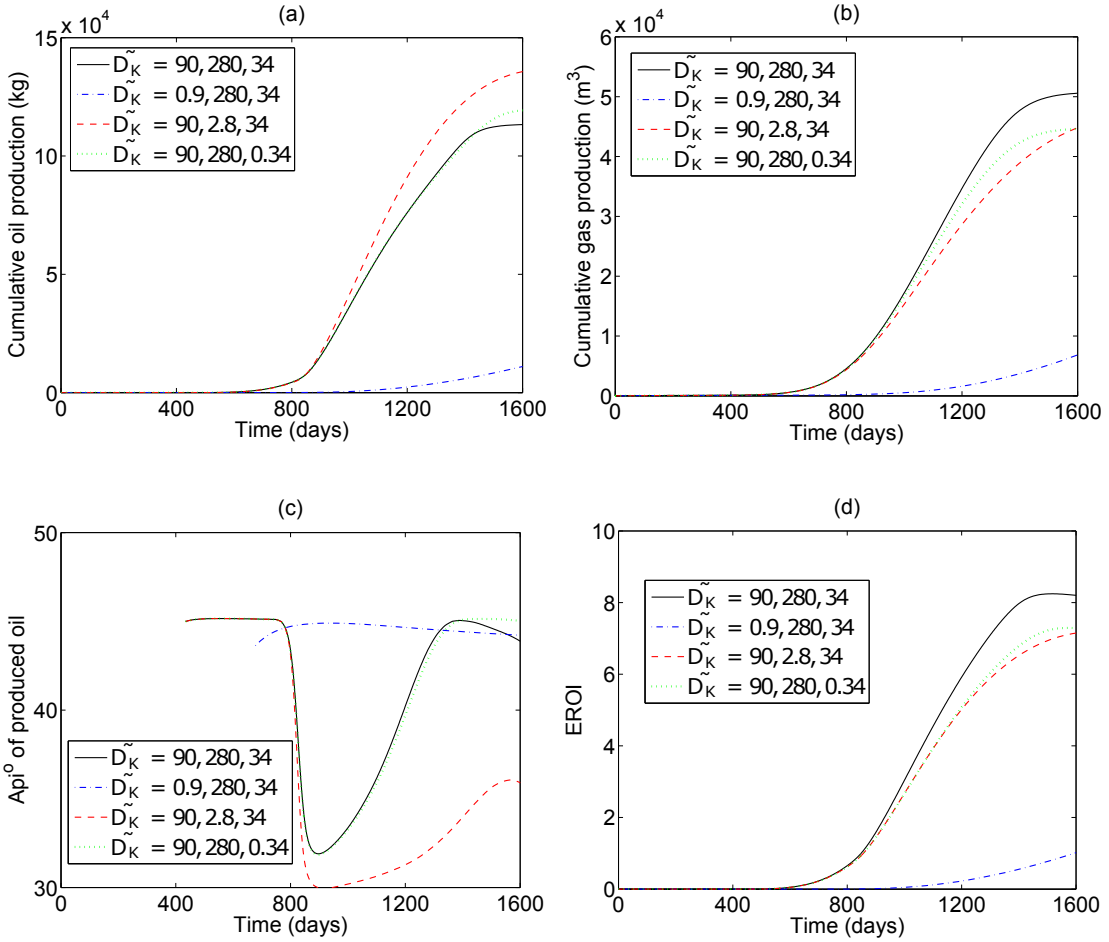

FIGURE 5.7: Variation of hydrocarbon production profile with Damköhler numbers for test case 2.

has a moderate impact on EROI for test case 1 (Figure 5.6d). Changing $\tilde{D_{K2}}$ does not affect the first half of the production profile, but changes significantly the second half. Since a lesser quantity of light component is created, the production of gas is reduced. Also, the oil production and the API ^{o} of the produced oil are lower. Changing $\tilde{D_{K3}}$ only changes the very last part of the production profile, with less production of gas and light oil.

On the contrary, the final EROI is significantly reduced when changing $\tilde{D_{K1}}$ from 90 to 0.9 for test case 2 (Figure 5.7d). In this case, the pyrolysis of kerogen is too slow and only a small amount has decomposed after 2τ. The API ^{o} remains high as heavy components created near the heaters do not have the time to reach the producer well. Changing $\tilde{D_{K2}}$ impacts significantly the oil production in the second half of the profile. We produce less light components and more heavy components. The production of gas

is also reduced. Changing $\tilde{D_{K3}}$ affects significantly the gas production in the second half of the profile.

To summarize, we observe that to obtain the best EROI, we need a large $\tilde{D_{K1}}$, at least larger than 10. We will see later that the optimal is obtained when the minimum of the three $\tilde{D_{Ki}}$ is larger than 10. Therefore, the minimum heater temperature required for efficient production verifies:

$$T_H \geq T_{R10,1} = \frac{E_{a1}}{R \log(D_{K1}/10)} \tag{5.17}$$

However, the extended Damköhler number are not independent as they describe chemical reactions of the same kinetic model and they all depend on the temperature of the heaters. Generally, $\tilde{D_{K3}}$ is smaller than $\tilde{D_{K1}}$ and $\tilde{D_{K2}}$ as it describes the decomposition of a lighter component. In the next section, we show the existence of an optimal heater temperature for both test cases 1 and 2.

5.4.3 Identification of optimal heater temperature

In this section we study the impact of the heater temperature on the EROI of the process after 2τ. We perform numerical simulations with the heater temperature varying from 250^oC to 400^oC for test cases 1 and 2. Figure 5.8 shows the evolution of the EROI for both cases.

When the heater temperature is low, the chemical reactions are too slow for the process to be efficient. When the heater temperature is very large, the decomposition is completed before the domain reaches the maximum temperature and a significant part of the energy invested is used to simply heat up the rock.

Figure 5.8a shows a maximum EROI for a temperature of 344.5^oC and Figure 5.8b shows a maximum EROI for a temperature of 338^oC. At these temperatures, the Damköhler numbers are $\tilde{D_{K1}} = 1075$, $\tilde{D_{K2}} = 300$ and $\tilde{D_{K3}} = 11.5$ for test case 1 and $\tilde{D_{K1}} = 48$, $\tilde{D_{K2}} = 128$ and $\tilde{D_{K3}} = 14.7$ for test case 2. We observe that for both test cases, the optimal energy efficiency is obtained when the lowest of the Damköhler numbers of the set of reactions included in the model is between 10 and 20. This is in accordance with an optimal temperature obtained at T_{R20} for the simplified model in Chapter 3

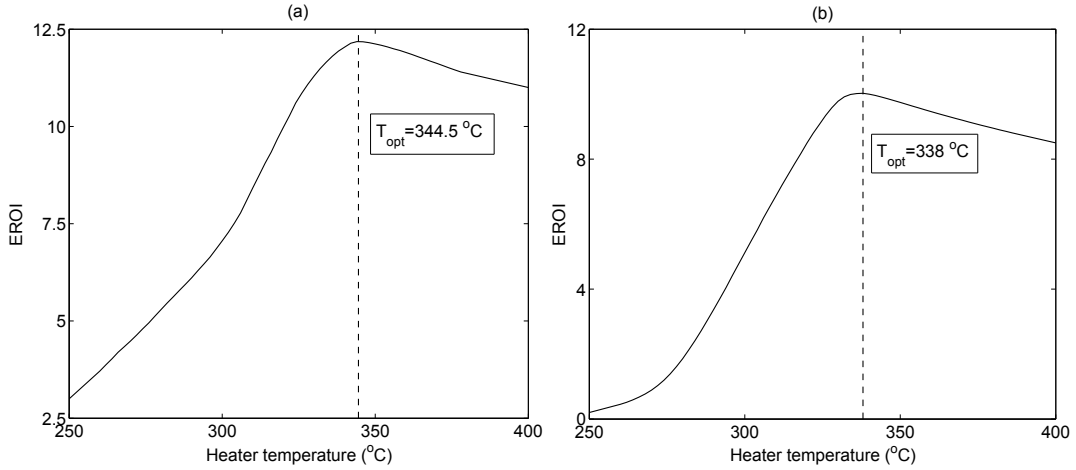

FIGURE 5.8: Evolution of EROI with heater temperature for (a) test case 1 and (b) test case 2. When the heater temperature is low, the chemical reactions are too slow and the process is not efficient. When the temperature is very large, the decomposition is completed before the domain reaches the maximum temperature and an important part of the energy invested is used to simply heat up the rock. The optimal temperature is obtain at $T = 344.5^oC$ for test case 1 and $T = 338^oC$ for test case 2.

(Equation 3.27). We conclude that the optimal temperature of the process for a model with k reactions lies within the range:

$$\max_{1\leq i\leq k} T_{R10,i} \leq T_{opt} \leq \max_{1\leq i\leq k} T_{R20,i} \tag{5.18}$$

Equation 5.18 has been obtained for a cubic geometry with four heaters, one on each vertical side of the cube. However, since the heater pattern mainly impacts the time taken to bring the formation to a large temperature, the result should held as long as the characteristic length L of the domain is correctly defined.

This correlation can be used to reduce the number of numerical experiments necessary to identify the optimal production scheme. For test case 1, $T_{R10} = 343^oC$ and $T_{R20} = 351^oC$. Therefore, we know before performing any numerical simulation that the optimal temperature is somewhere in the interval $[343^oC\ 351^oC]$. For test case 2, the corresponding interval is $[332^oC\ 342^oC]$.

Now, if the heater temperature is fixed, for example to 350^oC, Equation 5.18 gives a characteristic length interval. For test case 1, $T_{R10} = 350^oC$ correspond to $L = 7.3m$ and $T_{R20} = 350^oC$ correspond to $L = 10.4m$, so the optimal characteristic length is somewhere in the interval $[7.3m\ 10.4m]$. For test case 1, $T_{R10} = 350^oC$ correspond to

$L = 5.4m$ and $T_{R20} = 350^oC$ correspond to $L = 7.6m$, so the optimal characteristic length is somewhere in the interval $[5.4m\ 7.6m]$.

5.5 Summary and conclusions

In this chapter, we developed a more complete mathematical model to describe the In-Situ Upgrading of heavy oil and oil shale. We used Inspectional Analysis to identify the dimensionless numbers that fully described the model. For a case with k reactions, n_f fluid components and n_s solid components, the process was described by $9 + k(3 + n_f + n_s - 2) + 8n_f + 2n_s$ dimensionless groups.

Next, we computed a range of values for each dimensionless group. This range was obtained by first establishing a range of values for each dimensional parameter of the ISU of bitumen and oil shale from a thorough literature review, then computing the minimum and maximum values of the dimensionless groups.

We demonstrated that the extended Damköhler number describing the ratio of chemical rate to heat conduction rate at the heater temperature was the most important number. For this, we used DOE to identify the primary parameters for the energy efficiency of the process for a simplified model with one reaction and four components. We observed that the most important numbers were the extended Damköhler number, the reduced reactant volumetric capacity, the gas stoichiometric coefficient and the reduced reaction enthalpy. We showed that special effort should be made to measure accurately the activation energy of the reaction, and that the reaction enthalpy should not be neglected.

We obtained a correlation for finding the optimal heater temperature for the energy efficiency of the process. For test cases 1 and 2, which both included three reactions, we had three Damköhler numbers, one for each reaction. We studied the evolution of the production profile when successively changing them for test cases 1 and 2. We observed that the extended Damköhler number for the reaction describing the decomposition of primary reactant (K or NSO) needed to be at least 10 for the process to be efficient.

Finally we observed that test cases 1 and 2 were giving the best energy efficiency for a heater temperature of 344.5^oC and 338^oC, respectively. In both cases, this optimal

heater temperature was obtained when the minimum of the extended Damköhler numbers for all reactions included in the model was between 10 and 20. This result is in accordance with the one obtained in Chapter 3 (Equation 3.27) for a model with one reaction and no liquid phase, and can be used to reduce the number of numerical experiments necessary to identify the optimal production scheme.

Chapter 6

Numerical simulation of In-Situ Upgrading using Operator Splitting, Adaptive Implicit and Runge-Kutta methods

The objective of this chapter is to develop an algorithm for the numerical simulation of the ISU process that is generally more precise than the Fully Implicit Method (FIM) and potentially leads to large speed-ups. First, we evaluate the various OS methods defined in Chapter 4 on the two test cases defined in Chapter 5. We use different time-stepping strategies based on a target time truncation error and a target maximum variable change and we compare the discretization error obtained with a splitting method with the one obtained with FIM.

Numerical simulations of the ISU process are often very slow. To model accurately the chemical reactions, we generally need to use small time-steps and a large compositional model, often with more than 20 components. Solving the transport steps with such a large number of variables is computationally expensive. However, the chemical reaction operator on its own is described by a set of Ordinary Differential Equations (ODE) that can be solved locally and represents a small computational effort in comparison with the transport step. One of the advantage of Operator Splitting (OS) methods is the possibility of applying two different compositional models, an original one with a large

number of components for the chemical reaction operator, and a lumped one with only a small number of pseudo-components for the transport step. Such a method could potentially lead to large speed-ups with limited loss in accuracy.

Another advantage of OS methods is the possibility of applying dedicated solvers to each operator. In reservoir simulation, the transport step is generally solved using fully implicit backward Euler integration. This method is first-order accurate and can be accelerated by Adaptive Implicit Method (AIM) [20]. The chemical operator can be easily solved using higher order methods such as Runge-Kutta (RK) methods [58] in order to obtain a more accurate solution. This could reduce the overall discretization error of the method and potentially compensate for the additional error generated by the splitting.

In this work, we evaluate the use of the second-order trapezoidal rule and the third-order Explicit Singly Diagonally Implicit Runge-Kutta (ESDIRK) method described by Kvaerno [50]. We demonstrate how we can reduce the CPU time by (1) regrouping the components into lumped pseudo-components after the chemical reaction step and (2) applying Adaptive Implicit Method (AIM) to the transport step. We evaluate the speed-ups obtained for a test case with a full kinetic model including 26 components that can be regrouped into 6 lumped pseudo-components for the heat conduction and the heat and mass convection operators.

The algorithm described is faster and more precise than FIM for the ISU process, for which the chemical reactions depend primarily on the temperature. However, if the model includes chemical reactions of a different nature than pyrolysis, the splitting error could be more important. For example, if the phase exchange between oil and gas are slow, the system may not be at thermodynamic equilibrium. In this case, the equilibrium deviation is modelled by a non-equilibrium (or transient) reaction. The rate of the equilibrium deviation reaction mostly depends on the phase compositions. We demonstrate that for large deviation rates, the splitting method could introduce an error that cannot be compensated for by applying a higher order method to the chemical operator.

6.1 Evaluation of Operator Splitting Methods

The splitting methods considered here have been described in Chapter 4 where they were evaluated on a simplified model where a solid reactant decomposes into non-reactive gas. We observed that ISO did not perform well due to many convergence failures. The standard Sequential Split Operator (SSO) applied with first the advection operator followed by the chemical reaction (SSO-AK) provided a converged solution but gave a large pressure error. In the other direction (SSO-KA), it gave a large saturation error. The Strang-Marchuk Split Operator (SMSO) did not improve the result significantly. To limit the splitting error of SSO, we developed a method that conserved the main interactions. First, the heat was transported by conduction (operator C). Then, the chemical reaction was solved (operator K). Finally the mass and heat convection were performed (operator A with no conduction). This method, defined as SSO-CKA, provided a converged solution and generated fewer discretization errors than the standard SSO and the SMSO method. We now investigate whether these observations are also true for the ISU mathematical model defined in Chapter 5.

6.1.1 Comparison of FIM and SNIA

We evaluate the precision of FIM, SSO-AK, SSO-KA, SMSO and SSO-CKA for the ISU of Athabasca bitumen (Chapter 5, test case 1) and the ISU of Green River oil shale (Chapter 5, test case 2). For each test case, we define a reference solution by solving the full system of equations with FIM with a dimensionless time-step $\Delta t_D = 10^{-4}$. The reference solution is denoted by $\overline{P}$ for pressure, $\overline{T}$ for temperature and $\overline{z_j}$ for overall compositions.

We then study the evolution of the relative error with the reference solution for FIM, SSO-AK, SSO-KA, SMSO and SSO-CKA as a function of the time-step. We use the

following definitions for the normalized error L_1 for each variable:

$$\begin{aligned} e_P &= \max_n \left(\frac{1}{n_d} \sum_{x_i,y_i} \frac{|P(t^n,x_i,y_i) - \overline{P}(t^n,x_i,y_i)|}{P_0} \right), \\ e_T &= \max_n \left(\frac{1}{n_d} \sum_{x_i,y_i} \frac{|T(t^n,x_i,y_i) - \overline{T}(t^n,x_i,y_i)|}{\Delta T} \right) \\ e_z &= \max_j \max_n \left(\frac{1}{n_d} \sum_{x_i,y_i} |z_j(t^n,x_i,y_i) - \overline{z_j}(t^n,x_i,y_i)| \right) \end{aligned} \tag{6.1}$$

and the total L_1 error is defined as:

$$e_{L_1} = \frac{e_P + e_T + e_z}{3} \tag{6.2}$$

Here, the normalized overall composition error replaces the normalized saturation error used in Chapter 4. This is because, unlike for the simplified model, several components are mixed in the gas and oil phases, so that the overall compositions characterize the system more accurately than saturations.

For SMSO, we use two time-steps to solve the chemical reactions. This way, the four methods perform the same number of transport steps and the same number of chemical reaction steps. It has been demonstrated in Chapter 4 that the computational effort is roughly the same for the four SNIA methods.

Figures 6.1 and 6.2 show the evolution of the normalized errors with time-step for test cases 1 and 2, respectively. The time-steps shown on the x-axis are Δt_D for SSO and $\Delta t_D/2$ for SMSO, so that the four SNIA methods perform the same number of transport steps and the same number of chemical reaction steps.

We observe that SSO-AK gives a large pressure error and SSO-KA a large composition error. SMSO does not significantly improve the result. In both cases, SSO-CKA gives the lowest discretization error of the four SNIA methods.

6.1.2 Convergence of ISO

The internal iterations of ISO converge in the case of linear operators [26] but not necessarily for non-linear operators [42]. We observed in Chapter 4 that ISO had a lot of convergence failures for the simplified model describing thermal decomposition of

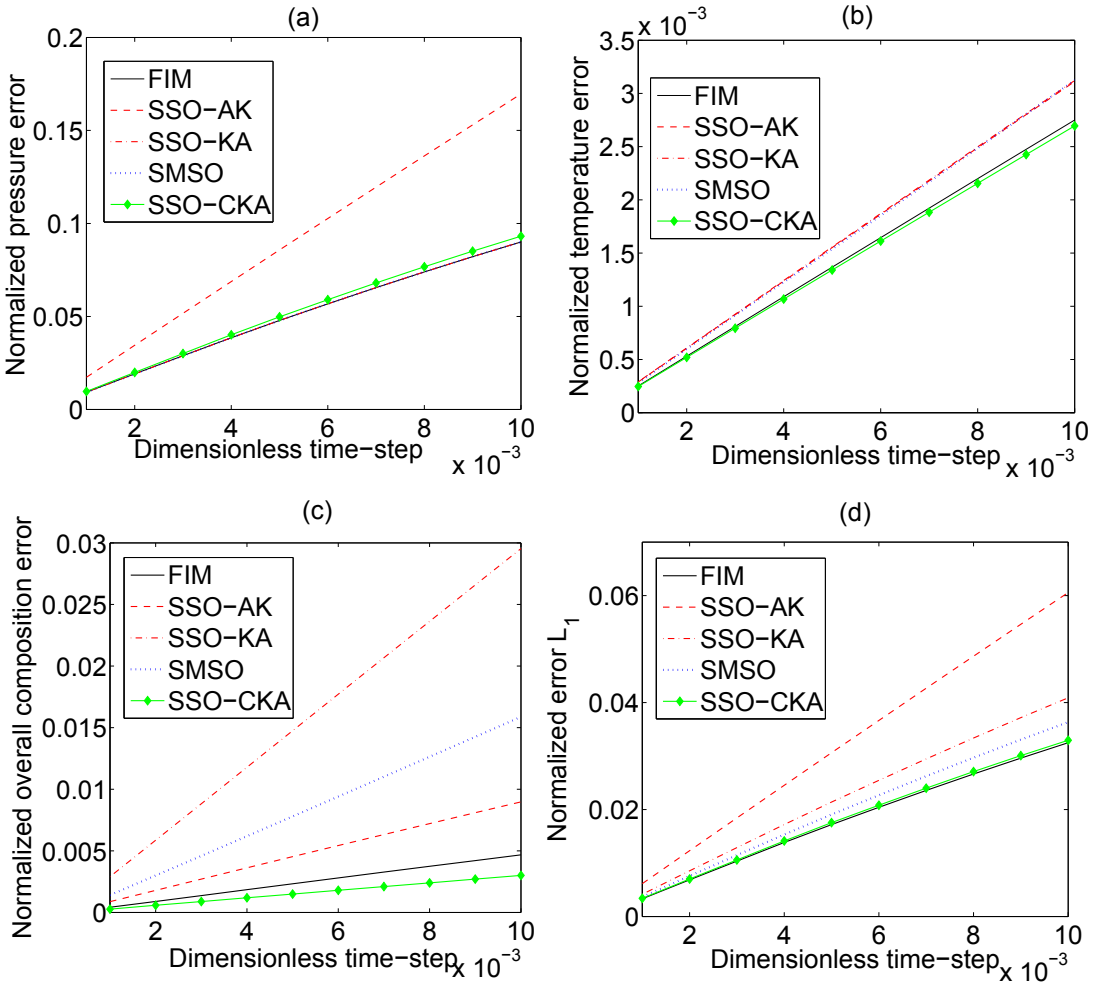

FIGURE 6.1: Evolution of the normalized errors of FIM, SSO-AK, SSO-KA, SMSO and SSO-CKA with time-step for ISU of Athabasca bitumen (test case 1). We observe a large pressure error for SSO-AK, and a large composition error for SMSO and SSO-KA. SSO-CKA gives the lowest discretization error of the four SNIA methods.

solid reactant into non-reactive gas. Now, we compare the convergence behaviour of FIM and ISO for the ISU of Athabasca bitumen (Chapter 5, test case 1) and the ISU of Green River oil shale (Chapter 5, test case 2). Details of our implementation of ISO are given in Appendix B.

Figure 6.3 shows the number of non-linear iterations used to solve the transport step for each case, using FIM and ISO with a dimensionless time-step $\Delta t_D = 0.01$. For both test cases, ISO performs a lot more iterations because of convergence failures. As for the simplified model, the stability error arising from the explicit treatment of one of the operators in each sub-step is too large and is not cancelled by alternating and iterating over the splitting scheme.

As for the simplified model, it should be noted that the choice of the initial guess u_0^* can

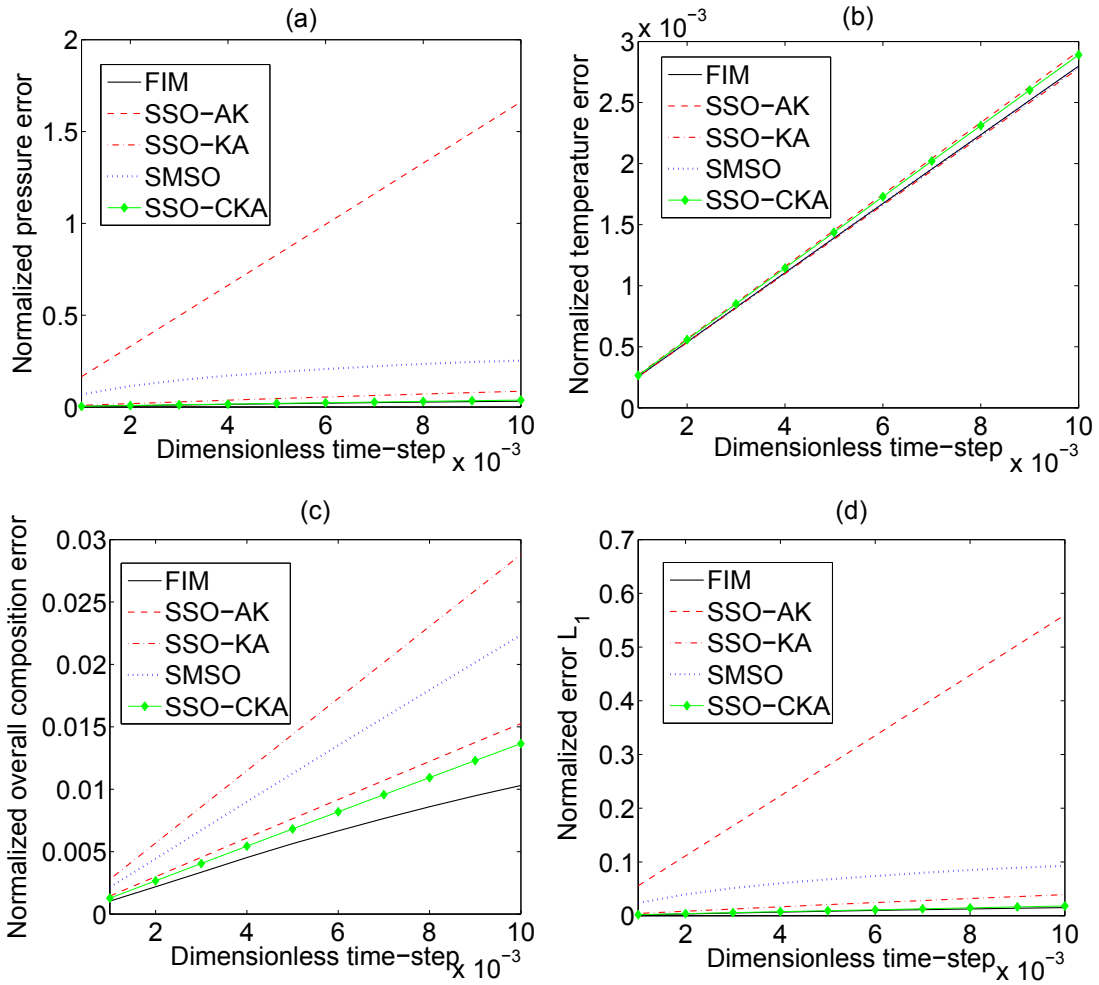

FIGURE 6.2: Evolution of the normalized errors of FIM, SSO-AK, SSO-KA, SMSO and SSO-CKA with time-step for ISU of Green River oil shale (test case 2). We observe a large pressure error for SSO-AK and SMSO, and a large composition error for SSO-KA. SSO-CKA gives the lowest discretization error of the four SNIA methods.

have a large impact on the performance of the method. However, we were unable to find a better choice that $u_0^* = u^n$. Finding the right guess that ensures the stability of the splitting iteration could potentially make ISO applicable for the numerical simulation of ISU.

6.2 Time-step selection

The results shown in Figures 6.1 and 6.2 were obtained for constant time-steps. We now compare the precision of FIM and SSO-CKA for the evolving time-step strategy based on time truncation error described in Chapter 4 (Equation 4.13).

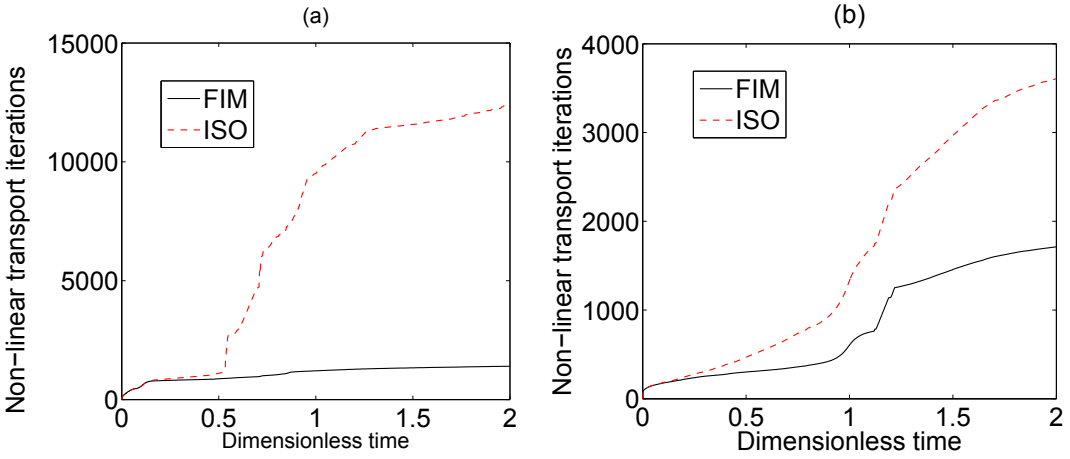

FIGURE 6.3: Number of non-linear transport iterations for (a) the ISU of Athabasca bitumen (test case 1) and (b) the ISU of Green River oil shale (test case 2) for both FIM and ISO. We observe a large difference between the two methods, which is due to convergence failures for ISO.

6.2.1 Comparison of precision with no reaction enthalpies

For test cases 1 and 2, the reaction enthalpies are initially neglected. Figure 6.4 shows the evolution of the normalized L_1 error with dimensionless time. We observe that the error has two peaks. The first one corresponds to a large pressure error generated by the thermal expansion of the reactants and the creation of large volumes of gas. The second peak corresponds to a large composition error induced by the coupling between reactions and flow in the liquid and gas phase. Table 6.1 shows the comparison of maximum and average error for both test cases. We observe that the error of FIM and SSO-CKA are of the same order.

	Test case 1 $\Delta h_r^* = 0$		Test case 2 $\Delta h_r^* = 0$	
	Max	Mean	Max	Mean
FIM $\eta = \eta' = 0.01$	1.8×10^{-3}	6.3×10^{-4}	8×10^{-3}	2×10^{-3}
SSO-CKA $\eta = \eta' = 0.01$	1.8×10^{-3}	6.3×10^{-4}	8×10^{-3}	2×10^{-3}

TABLE 6.1: Comparison of maximum and mean errors of FIM and SSO-CKA using an evolving time-stepping strategy for ISU of Athabasca bitumen (test case 1) and ISU of Green River oil shale (test case 2). We observe that for both cases, the errors of FIM and SSO-CKA are of the same order.

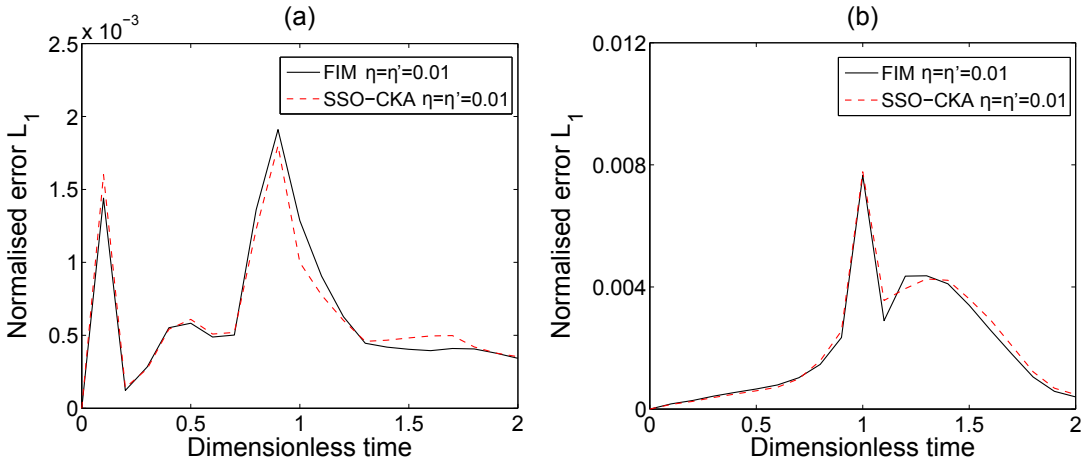

FIGURE 6.4: Comparison of discretization errors between FIM and SSO-CKA using an evolving time-stepping strategy for (a) ISU of Athabasca bitumen (test case 1) and (b) ISU of Green River oil shale (test case 2). We observe that for both cases, the error of FIM and SSO-CKA are of the same order.

6.2.2 Comparison of precision with reaction enthalpies

SSO-CKA works best when the reaction enthalpies are small so most of the effect of advection-diffusion on the chemical reactions comes from the heat conduction. The reaction enthalpies have been neglected in test cases 1 and 2, but we demonstrated in Chapter 5 that they can have an important impact on the energy efficiency of the process and should not be neglected. To assess the impact of reaction enthalpies on the precision of SSO-CKA, we modify test cases 1 and 2 with the values of reaction enthalpies defined in Table 6.2. These were obtained from Phillips et al. [67].

TABLE 6.2: Values of modified reaction enthalpies for test cases 1 and 2.

	Test case 1			Test case 2		
Reaction	1	2	3	1	2	3
Δh_{ri} (kJ/kg)	271	169	821	32	169	821
Δh^*_{ri}	0.56	0.35	1.7	0.10	0.51	2.5

We now compare the precision of FIM and SSO-CKA using an evolving time-step strategy for test cases 1 and 2 with the modified reaction enthalpies. Figure 6.5 shows the evolution of the normalized L_1 error with dimensionless time for both test cases and Table 6.3 shows the comparison of maximum and average errors for both test cases. We observe that SSO-CKA gives a larger error than FIM for the same target time truncation error and maximum variable change. To reduce the discretization error, we can reduce the target time truncation error and the target maximum variable change

($\eta = \eta' = 0.005$). We obtain smaller maximum and mean errors for SSO-CKA with this time-step strategy than for FIM with $\eta = \eta' = 0.01$. However, this strategy involves roughly twice as much computation. Another possibility is to try to compensate this error by decreasing the error inside the chemical operator. Indeed, the total discretization error can be seen as the sum of the error of each operator plus the splitting error. All these errors are of order 1, so by applying a method of order 2 or more to the chemical operator, we could cancel the effect of the splitting error.

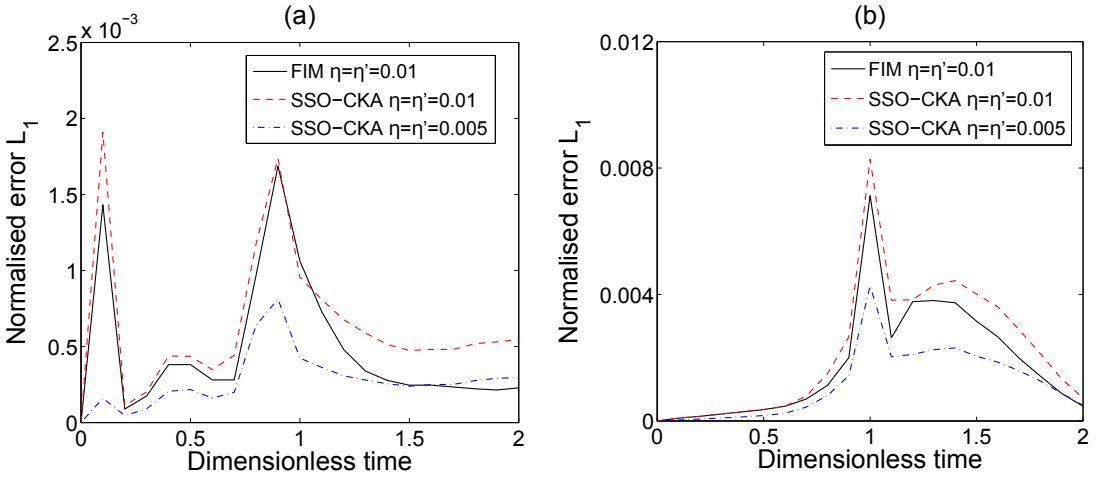

FIGURE 6.5: Comparison of discretization errors between FIM and SSO-CKA using an evolving time-stepping strategy for (a) ISU of Athabasca bitumen (test case 1) and (b) ISU of Green River oil shale (test case 2) with modified reaction enthalpies (Table 6.2). We observe that SSO-CKA gives a larger discretization error than FIM for a target time truncation error of 0.01. This error can be reduced by using $\eta = \eta' = 0.005$.

	Test case 1 Δh_r^* in Table 6.2		Test case 2 Δh_r^* in Table 6.2	
	Max	Mean	Max	Mean
FIM $\eta = \eta' = 0.01$	1.7×10^{-3}	4.7×10^{-4}	7.1×10^{-3}	1.8×10^{-3}
SSO-CKA $\eta = \eta' = 0.01$	1.9×10^{-3}	6.4×10^{-4}	8.3×10^{-3}	2.2×10^{-3}
SSO-CKA $\eta = \eta' = 0.005$	8.1×10^{-4}	2.7×10^{-4}	4.3×10^{-3}	1.2×10^{-3}

TABLE 6.3: Comparison of maximum and mean errors of FIM and SSO-CKA using an evolving time-stepping strategy for ISU of Athabasca bitumen (test case 1) and ISU of Green River oil shale (test case 2) with modified reaction enthalpies (Table 6.2). We observe that SSO-CKA gives a larger discretization error than FIM for a target time truncation error of 0.01. This error can be reduced by using $\eta = \eta' = 0.005$.

6.3 Runge-Kutta methods for the chemical reaction operator

In this section, we consider two methods, the second-order trapezoidal rule and the third-order ESDIRK method [50]. Both methods can be seen as s-stage RK methods, which will be briefly explained here using a simple illustrative ODE:

$$\frac{\partial u}{\partial t} = f\left(t, u\right) \tag{6.3}$$

An s-stage RK method is defined by:

$$\begin{aligned}
U^1 &= u^n + \Delta t^n \sum_{j=1}^{s} a_{1j} f\left(t^n + c_j \Delta t^n, U^j\right) \\
&\vdots \quad\quad \vdots \quad\quad \vdots \\
U^s &= u^n + \Delta t^n \sum_{j=1}^{s} a_{sj} f\left(t^n + c_j \Delta t^n, U^j\right) \\
u^{n+1} &= u^n + \Delta t^n \sum_{i=1}^{s} b_i f\left(t^n + c_i \Delta t^n, U^i\right)
\end{aligned} \tag{6.4}$$

where U^i denotes the solution at the i-th integration stage and Δt^n the time-step length. These methods are often described by a table called the *Butcher tableau* (named after John C. Butcher [13]):

$$\begin{array}{c|cccc}
c_1 & a_{11} & a_{12} & \dots & a_{1s} \\
c_2 & a_{21} & a_{22} & \dots & a_{2s} \\
\vdots & \vdots & \vdots & \ddots & \vdots \\
c_s & a_{s1} & a_{s2} & \dots & a_{ss} \\
\hline
 & b_1 & b_2 & \dots & b_s
\end{array} = \begin{array}{c|c} c & A \\ \hline & b^T \end{array} \tag{6.5}$$

RK methods are called stiffly accurate if $b_j = a_{sj}$, $\forall j = 1, 2, ..., s$. Stiffly accurate methods avoid the order reduction phenomenon observed for stiff ODEs [69].

6.3.1 Trapezoidal Rule

The Trapezoidal Rule (TR) is an integration method of order 2 [58], which can be defined as a two-stage RK method with Butcher tableau:

$$\begin{array}{c|cc} 0 & 0 & 0 \\ 1 & \frac{1}{2} & \frac{1}{2} \\ \hline & \frac{1}{2} & \frac{1}{2} \end{array} \tag{6.6}$$

It can also be seen as a one-step θ-method:

$$\frac{u^{n+1} - u^n}{\Delta t^n} = \theta f\left(t^{n+1}, u^{n+1}\right) + (1-\theta) f\left(t^n, u^n\right) \tag{6.7}$$

with

$$\theta = \frac{1}{2} \tag{6.8}$$

This method is second-order accurate and unconditionally stable, although less robust than FIM for large time-steps. It requires that one linear system is solved for each non-linear iteration so has roughly the same complexity as FIM.

6.3.2 Third-order ESDIRK method

Explicit RK methods, for which the matrix A is strictly lower triangular, are computationally fast as all internal stages of Equation 6.4 can be calculated explicitly. However, they suffer from stability limits [33]. Implicit Runge-Kutta methods are more stable but each time-integration step requires the solution of $m \times s$ equations, where m is the number of independent variables. For Diagonally Implicit Runge-Kutta (DIRK) methods, the matrix A is lower triangular. If all diagonal elements of a DIRK method are identical, the method is said to be Singly Diagonal Implicit (SDIRK). If the first stage of an SDIRK method is explicit, it is said to be Explicit Singly Diagonally Implicit (ESDIRK).

ESDIRK methods are attractive as they can be constructed such that they are stable and stiffly accurate [32]. Also, the diagonal structure of the Butcher tableau allows sequential evaluation of the internal stages. Hence, the computational cost is lower than for general implicit RK methods. Kvaerno et al. [50] described a four-stage third-order

ESDIRK method (ESDIRK3) defined by the Butcher tableau:

$$\begin{array}{c|cccc} 0 & 0 & 0 & 0 & 0 \\ 2\gamma & \gamma & \gamma & 0 & 0 \\ 1 & \frac{-4\gamma^2+6\gamma-1}{4\gamma} & \frac{-2\gamma+1}{4\gamma} & \gamma & 0 \\ 1 & \frac{6\gamma-1}{12\gamma} & \frac{-1}{(24\gamma-12)\gamma} & \frac{-6\gamma^2+6\gamma-1}{6\gamma-3} & \gamma \\ \hline 1 & \frac{6\gamma-1}{12\gamma} & \frac{-1}{(24\gamma-12)\gamma} & \frac{-6\gamma^2+6\gamma-1}{6\gamma-3} & \gamma \end{array} \tag{6.9}$$

with:

$$\gamma = 0.4358665215 \tag{6.10}$$

6.3.3 Comparison of precision with evolving time-step strategy

We compare the precision of FIM and SSO-CKA for different chemical solvers. First, we use the standard backward Euler method (SSO-CKA). Then we solve the chemical reactions with the trapezoidal rule (SSO-CKA-TR) and with the third-order ESDIRK method (SSO-CKA-ESDIRK3).

First, we consider the case of no reaction enthalpies. Figure 6.6 shows the evolution of the normalized error L_1 with dimensionless time for ISU of Athabasca bitumen (test case 1) and ISU of oil shale (test case 2) and Table 6.4 shows the comparison of maximum and average errors for both test cases. The time-stepping strategy used is the one defined in Chapter 4 (Equation 4.13). We observe that applying the trapezoidal rule to the chemical operator (SSO-CKA-TR) improves significantly the precision of the method. Applying the third-order ESDIRK method (SSO-CKA-ESDIRK3) does not decreases the error further.

Next, we consider the case with reaction enthalpies given in Table 6.2. Figure 6.7 shows the evolution of the normalized error L_1 with dimensionless time for ISU of Athabasca bitumen (test case 1) and ISU of oil shale (test case 2) and Table 6.5 shows the comparison of maximum and average error for both test cases. We observe that SSO-CKA gives a larger error than FIM, but this error can be compensated by applying the trapezoidal rule to the chemical operator (SSO-CKA-TR). Again, the precision of the method is not improved by the third-order ESDIRK method (SSO-CKA-ESDIRK3). To summarize, SSO-CKA-TR gives generally a more precise result than FIM. SSO-CKA-ESDIRK3 does not improve the result further.

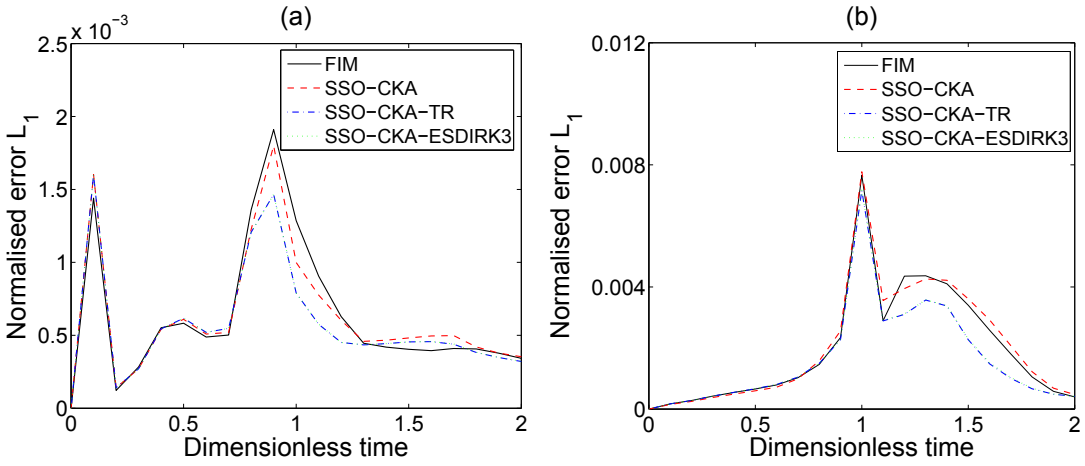

FIGURE 6.6: Comparison of discretization errors between FIM and SSO-CKA using an evolving time-stepping strategy ($\eta = \eta' = 0.01$) for (a) ISU of Athabasca bitumen (test case 1) and (b) ISU of Green River oil shale (test case 2) using different chemical solvers. We observe that applying the trapezoidal rule to the chemical operator (SSO-CKA-TR) improves significantly the precision of the method. Applying the third-order ESDIRK method (SSO-CKA-ESDIRK3) does not decreases the error further.

	Test case 1 $\Delta h_r^* = 0$		Test case 2 $\Delta h_r^* = 0$	
	Max	Mean	Max	Mean
FIM	1.8×10^{-3}	6.3×10^{-4}	8×10^{-3}	2×10^{-3}
SSO-CKA	1.8×10^{-3}	6.3×10^{-4}	8×10^{-3}	2×10^{-3}
SSO-CKA-TR	1.6×10^{-3}	5.7×10^{-4}	7.2×10^{-3}	1.6×10^{-3}
SSO-CKA-ESDIRK3	1.6×10^{-3}	5.7×10^{-4}	7.2×10^{-3}	1.6×10^{-3}

TABLE 6.4: Comparison of maximum and mean errors of FIM and SSO-CKA using an evolving time-stepping strategy ($\eta = \eta' = 0.01$) for ISU of Athabasca bitumen (test case 1) and ISU of Green River oil shale (test case 2) using different chemical solvers. We observe that applying the trapezoidal rule to the chemical operator (SSO-CKA-TR) improves significantly the precision of the method. Applying the third-order ESDIRK method (SSO-CKA-ESDIRK3) does not decreases the errors further

6.4 Efficient algorithm for large compositional model

6.4.1 Full kinetic model

In the previous chapter, test cases 1 and 2 were simulated with simplified kinetic models including three reactions and 6 components. To simulate accurately the chemical reactions, ISU kinetic models generally include a large number of components [12]. Behar et al [8] describe such a model for the heavy components NSO and C_{14+} of Safanya oil (Saudi Arabia). Al Darouich et al. [1] gives a similar model for the decomposition of C_{6-14}. Table 6.6 describes the full kinetic model. This model includes 26 components.

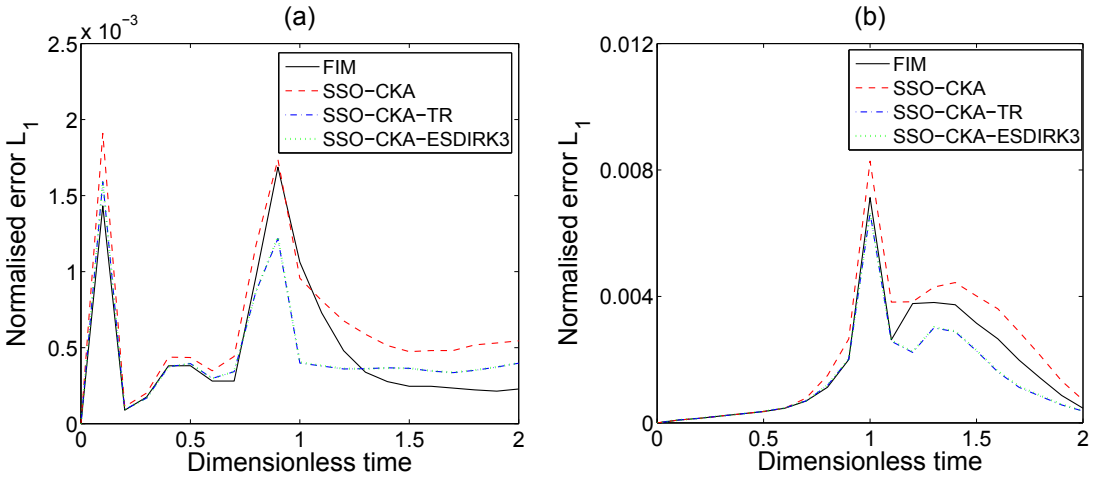

FIGURE 6.7: Comparison of discretization errors between FIM and SSO-CKA using an evolving time-stepping strategy ($\eta = \eta' = 0.01$) for (a) ISU of Athabasca bitumen (test case 1) and (b) ISU of Green River oil shale (test case 2) with modified reaction enthalpies (Table 6.2) using different chemical solvers. We observe that SSO-CKA gives a larger error than FIM, but this error can be compensated by applying the trapezoidal rule to the chemical operator (SSO-CKA-TR). Again, the precision of the method is not improved by the third-order ESDIRK method (SSO-CKA-ESDIRK3).

	Test case 1 Δh_r^* in Table 6.2		Test case 2 Δh_r^* in Table 6.2	
	Max	Mean	Max	Mean
FIM	1.7×10^{-3}	4.7×10^{-4}	7.1×10^{-3}	1.8×10^{-3}
SSO-CKA	1.9×10^{-3}	6.4×10^{-4}	8.3×10^{-3}	2.2×10^{-3}
SSO-CKA-TR	1.6×10^{-3}	4.5×10^{-4}	6.6×10^{-3}	1.4×10^{-3}
SSO-CKA-ESDIRK3	1.6×10^{-3}	4.5×10^{-4}	6.6×10^{-3}	1.4×10^{-3}

TABLE 6.5: Comparison of maximum and mean error of FIM and SSO-CKA using an evolving time-stepping strategy ($\eta = \eta' = 0.01$) for ISU of Athabasca bitumen (test case 1) and ISU of Green River oil shale (test case 2) with modified reaction enthalpies (Table 6.2) using different chemical solvers. We observe that SSO-CKA gives a larger error than FIM, but this error can be compensated by applying the trapezoidal rule to the chemical operator (SSO-CKA-TR). Again, the precision of the method is not improved by the third-order ESDIRK method (SSO-CKA-ESDIRK3).

Solving the transport step fully implicitly with such a large number of components is computationally expensive. However, when we apply SSO-CKA, we can use AIM with a simplified lumped compositional model for the transport step with no loss in accuracy by regrouping the components that have the same thermodynamic properties.

6.4.2 The SSO-CKA-AIM-TR algorithm

The Adaptive Implicit Method (AIM) is routinely used to accelerate FIM for isothermal reservoir simulations with a large number of components [20]. AIM reduces the size of

	H_2S	C_{1-4}	C_{6-14}						C_{14+}				NSO	Res	E	P	A
			Sat	Aro-1	Aro-2	Aro-3	Aro-4	Aro-5	Sat	Aro-1	Aro-2	Aro-3			(kJ/mol)	(%)	(s^{-1})
NSO	0.9	4.3	7.2	4.7					6.7	49.1				27.1	209	37.4	3.16E+12
															218	4.1	
															226	52.8	
															243	5.7	
															Total	100	
C_{14+} Sat		25.9	53.9	5.8							14.4				268	55.4	3.85E+16
															276	25.2	
															285	17.2	
															293	1.8	
															301	0.4	
															Total	100	
C_{14+} Aro-1	1.3	8.8	6.4	3.2					17.8		47.5			15.0	218	20.8	3.05E+13
															226	79.2	
															Total	100	
C_{14+} Aro-2		4.9										63.2		31.9	197	100	4.60E+10
C_{14+} Aro-3		6.5												93.5	206	65.0	5.10E+11
															228	35.0	
C_{6-14} Sat		67.8		32.2											281	100	3.85E+16
C_{6-14} Aro-1	0.1	16.5			15.1	10.0	32.3	3.0			15.0	8.0			233	66.0	5.10E+12
															249	34.0	
															Total	100	
C_{6-14} Aro-2	0.1	18.5				25.7		10.0			39.8	5.9			222	36.0	1.30E+13
															241	64.0	
															Total	100	
C_{6-14} Aro-3	0.1	10.9						50.6			31.9	6.5			216	19.0	5.10E+11
															233	81.0	
															Total	100	
C_{6-14} Aro-4	0.1	9.0						8.1			50.0	32.8			228	100	5.1E+12

TABLE 6.6: Overall kinetic scheme for the thermal cracking of the C_{14+} Safaniya oil (data from Behar et al. 2008 and Al Darouich et al.2006)

the system to be solved by identifying variables that can be treated explicitly with a switching criteria (Appendix B). However, applying AIM to the ISU of heavy oil presents several challenges. First of all, the stability criteria for temperature is generally very restrictive due to thermal conduction [59]. Secondly, large changes in solid saturation during one time-step can induce large changes in permeability. The stability criteria for saturation must take this into account. Finally, the creation of large volume of gas by chemical reaction could violate the quasi-incompressibility hypothesis necessary to obtain the CFL criteria [20].

However, AIM can be easily applied to the heat and mass convection operator in SSO-CKA. Since the heat conduction is not included in this operator, the temperature can be treated like any other variable. Also, we have no chemical reaction so the solid saturation is constant and the quasi-incompressibility hypothesis holds.

The size of the system can be reduced further by regrouping components into lumped pseudo-components. Several of the component defined in table 6.6 only differ by the activation energy and the stoichiometric coefficients of their decomposition. They can be regrouped into 6 lumped components, called chemical classes, for the heat conduction and the heat and mass convection operators without any loss of accuracy. These chemical classes are NSO, C_{14+}, C_{6-14}, C_{1-4}, H_2S and solid residual. Since the components lumped into one chemical class have the same thermodynamic properties, the relative composition inside the class are constant during the transport steps.

To summarize, we define the algorithm SSO-CKA-TR-AIM with the following steps:

1. Compute the new time-step using the target time truncation error and the target maximum variable change
2. Solve the heat conduction operator with FIM
3. Solve the chemical reaction operator with TR
4. Compute the composition of each lumped component
5. Compute and save the relative compositions inside each lumped component
6. Compute the stability criteria
7. Solve the heat and mass convection operator with AIM

8. Compute the composition of each component in the full kinetic model using the composition of the lumped components and the relative compositions saved in step 5

9. Advance time-step and go back to step 1

6.4.3 Comparison of CPU time

In this section, we compare the performance of FIM and SSO-CKA-TR-AIM for the ISU of Athabasca bitumen (test case 1) with the full kinetic model described in Table 6.6. Figure 6.8 shows the evolution of the CPU time with dimensionless time for both methods. SSO-CKA-TR-AIM is roughly seven times faster than FIM.

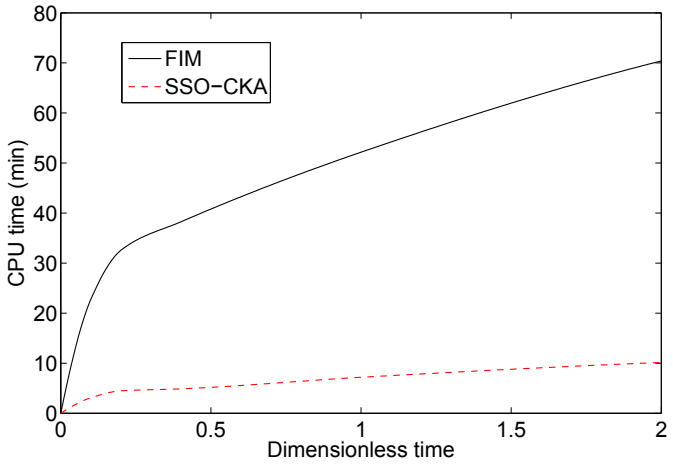

FIGURE 6.8: Comparison of CPU time for FIM and SSO-CKA method for ISU of Athabasca bitumen (test case 1) with the full kinetic model described in Table 6.6.

This speed-up has been obtained without any parallel computing or other code optimization. It is important to note that since the solving of the linear system for each non-linear iteration for the transport step is the bottleneck of the simulation, the complexity of SSO-CKA-TR-AIM is smaller than the one for FIM since the number of variable have been reduced. The speed-up can be improved by optimising the chemical reaction and conduction steps. Optimization for the transport step could improve the performance of both FIM and SSO-CKA-TR-AIM.

6.5 Impact of equilibrium deviation

So far, the results of this chapter have been obtained with a model that assumes equilibrium between the gas and liquid phases, modelled by Wilson K-values (Equation 5.11). Phase equilibrium is generally assumed in reservoir simulation since the time constant of the phase transfer is small compared to the time constant of the transport. However, for ISU, the phase exchanges are in competition with chemical reactions that are very fast when the temperature reaches a high value. In this case, equilibrium deviation can have a significant impact on the process.

6.5.1 Modelling equilibrium deviation with a non-equilibrium reaction

To demonstrate the potential impact of equilibrium deviation, we consider a simplified version of test case 1, with NSO and C_{14+} only present in the liquid phase and C_{1-4} and CO_2 only present in the gas phase. C_{6-14} is described by two components: $C_{6-14}(o)$ for the liquid phase and $C_{6-14}(g)$ for the gas phase. Phase exchange is modelled by a non-equilibrium reaction:

$$C_{6-14}(o) \xrightarrow{r_e} C_{6-14}(g) \tag{6.11}$$

The equilibrium deviation reaction rate r_e is given by:

$$r_e = A_e \rho_o S_o \left(\xi_{o,C_{6-14}} - \frac{\xi_{g,C_{6-14}}}{K_{C_{6-14}}} \right) \tag{6.12}$$

where A_e is the frequency factor of the equilibrium deviation, $\xi_{p,C_{6-14}}$ is the molar fraction of C_{6-14} in phase p and $K_{C_{6-14}}$ the Wilson K-value of C_{6-14} (Equation 5.11). In terms of dimensionless number, the reaction rate is described by the Damköhler number of the equilibrium deviation:

$$D_K^e = A_e \tau \tag{6.13}$$

For foamy oil, A_e ranges from 10^{-4} to 10^3 $1/day$ [75]. This gives a Damköhler range between 0.01 to 10^7.

Figure 6.9 shows the variation of the production profile for different values of D_K^e. We observe that for $D_K^e = 100$ and $D_K^e = 10^4$, the profile hardly changes from the profile for $D_K^e = \infty$ (equilibrium). The reaction is fast enough to be considered instantaneous.

For $D_K^e \leq 0.1$, the profile is almost identical to the one for $D_K^e = 0$. The reaction is too slow and the phase exchange can be ignored.

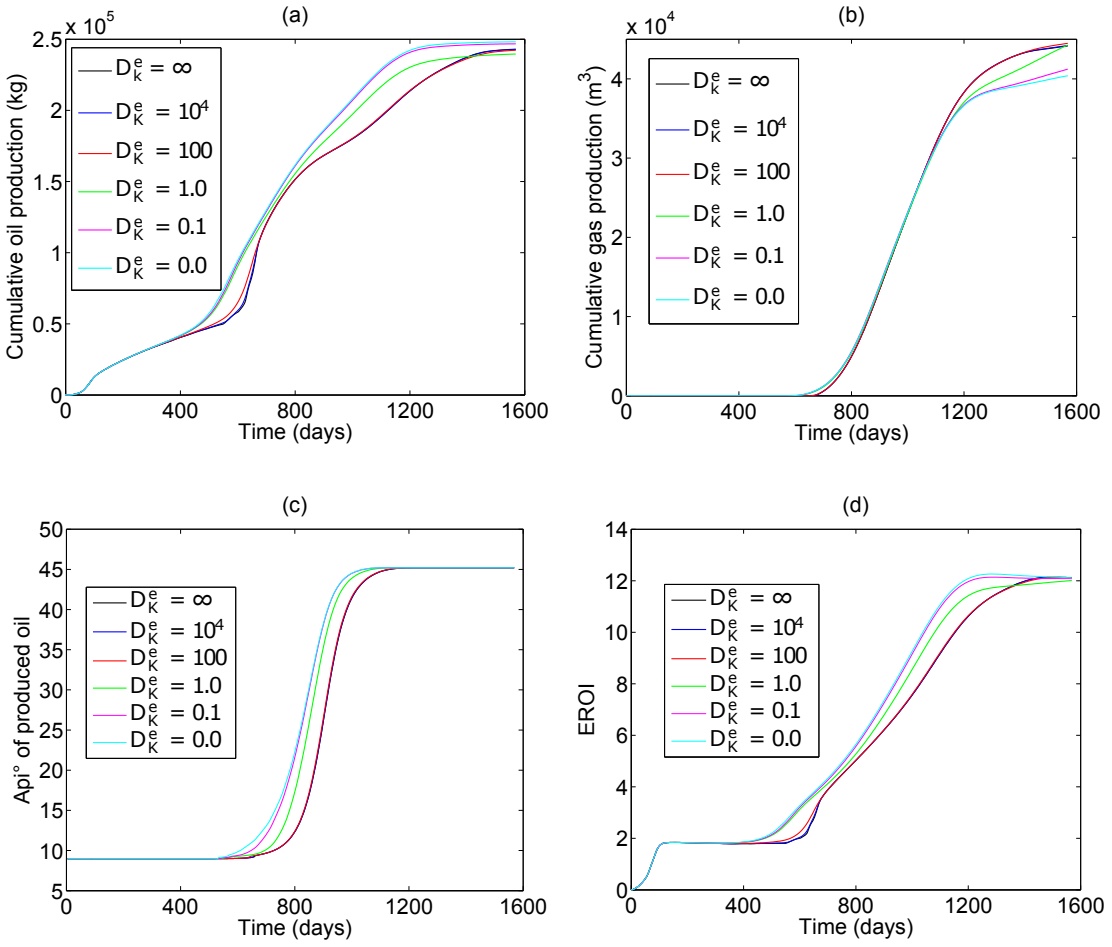

FIGURE 6.9: Variation of hydrocarbon production profile with D_K^e for test case 1 with one equilibrium deviation.

To summarize, we can identify three regimes for the equilibrium:

- Regime 1: $D_K^e \geq 100$, instantaneous equilibrium
- Regime 2: $D_K^e \leq 0.1$, no phase exchange
- Regime 3: $0.1 < D_K^e < 100$, phase transfer with a transient reaction

6.5.2 Application of SSO-CKA

Figure 6.4 shows that SSO-CKA, combined with the trapezoidal rule, gives less error than FIM for a model with instantaneous equilibrium (Regime 1). In this section, we

study the precision of the method when applied to test case 1 with equilibrium in Regime 2 and Regime 3.

Figure 6.10 shows the evolution of the normalized error L_1 for $D_K^e = 0$ (Regime 2) and for $D_K^e = 10$ (Regime 3). We observe that SSO-CKA gives less discretization error than FIM for Regime 2. In this case, the equilibrium reaction rate is zero, and the chemical operator depends mostly on the temperature. The order of the operators in SSO-CKA conserves most of the couplings. However, for Regime 3, we obtain a large discretization error for SSO-CKA toward the end of the simulation. This error is not properly cancelled by applying TR or ESDIRK3 to the chemical operator.

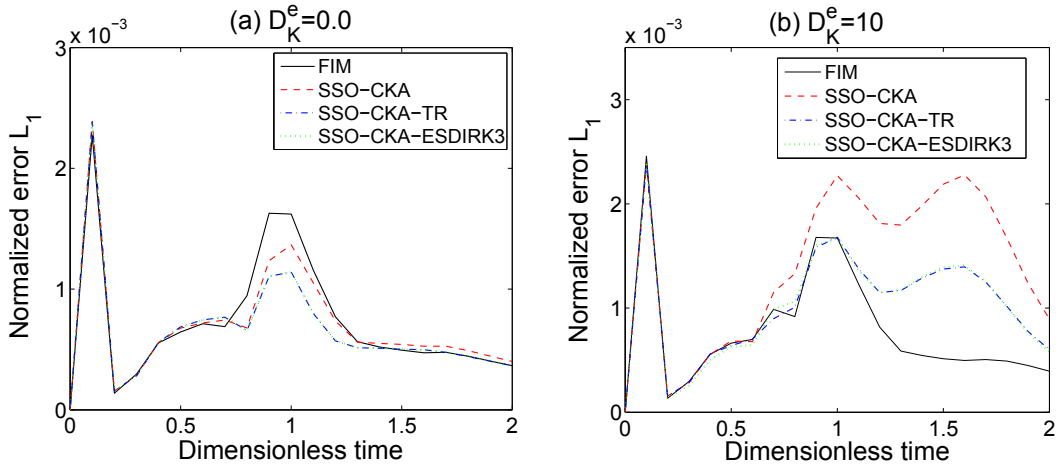

FIGURE 6.10: Comparison of discretization error between FIM and SSO-CKA using an evolving time-stepping strategy for ISU of Athabasca bitumen (test case 1) with equilibrium deviation. Figure (a) shows the result for $D_K^e = 0$ and figure (b) for $D_K^e = 10$).

It can be seen that SSO-CKA has limitations when applied to a case with phase transfer modelled by non-equilibrium reaction. These reactions do not depend strongly on temperature and are better handled by a numerical method based on Strang splitting [4]

6.6 Summary and conclusions

This chapter has focused on numerical methods for the ISU of bitumen and oil shale. We evaluated the various Operator Splitting methods described in Chapter 4. Again, we observed that the Iterative Split-Operator (ISO) did not perform well due to convergence failures and that the Strang-Marchuk Split-Operator (SMSO) gave large discretization

errors. The Sequential Split-Operator (SSO) gave the smallest discretization error when we split the heat conduction operator C, the kinetic operator K and the heat and mass convection operator A in this order (SSO-CKA).

We also evaluated the use of SSO-CKA with an evolving time-stepping strategy based on a target time truncation error and a target maximum variable change of 0.01. For test cases 1 and 2, for which the reaction enthalpies have been neglected, SSO-CKA and FIM gave similar discretization error. However, we demonstrated in Chapter 4 that SSO-CKA worked best when the reaction enthalpies were small. To test the limitations of the method, we modified test cases 1 and 2 so that they included the reaction enthalpies defined in Phillips et al. [67]. In this case, we observed that SSO-CKA gave a larger discretization error than FIM. This error could be cancelled by dividing the target time truncation error and the target maximum variable change by two. However, this strategy involved roughly twice as much computation.

To reduce the splitting error without significantly increasing the computational cost, we applied the second-order trapezoidal rule and the third-order four stage ESDIRK method described in [50] to the chemical operator. The trapezoidal rule reduced the discretization error so that SSO-CKA-TR gave smaller errors than FIM for test cases 1 and 2 with no reaction enthalpies and gave errors of the same order as FIM for test cases 1 and 2 with the reaction enthalpies given in Phillips et al. [67]. The third-order ESDIRK method did not reduce the error further.

Finally, we demonstrated how we could reduce the CPU time in the transport step. We used the Adaptive Implicit Method and reduced the number of variables by regrouping components with the same thermodynamic properties into a small number of lumped chemical classes. The full splitting algorithm was presented and denoted SSO-CKA-TR-AIM. We compared the CPU time of SSO-CKA-TR-AIM with FIM for a test case with a kinetic model including 26 components that could be regrouped into 6 lumped chemical classes for the transport step. For this test case, SSO-CKA-TR-AIM ran roughly 7 times faster than FIM.

Our investigations demonstrated that SSO-CKA-TR-AIM was the best method for the ISU of bitumen and oil shale when all reactions are pyrolysis reactions, for which the reaction rates depend mostly on temperature. However, it might not be suitable if the model includes reactions of a different nature. To demonstrate this, we considered the

case of equilibrium deviation modelled by a non-equilibrium reaction. We identified three regimes for the equilibrium: instantaneous equilibrium, no phase exchange and phase exchange with transient reactions. SSO-CKA was performing well for the regimes of instantaneous equilibrium and no phase exchange, but in the case of transient reactions, the discretization error was large and the increased accuracy of using the trapezoidal rule in the reaction step did not improve this. In this case, another numerical method should be applied. Since SMSO has been applied successfully for groundwater transport models with non-equilibrium reactions [4], a method which combines SMSO and SSO-CKA could improve the result for ISU with non-equilibrium reactions.

Chapter 7

Conclusion, recommendations and further work

This research focused on the numerical modelling of the In-Situ upgrading process and had three main objectives: (1) to quantify the main interactions between the heat conduction, the heat and mass convection and the chemical reactions, (2) to identify the primary parameters for the efficiency of the process and (3) to design a robust numerical method that reduces the CPU time of the simulations with limited loss in accuracy. We used dimensionless analysis to answer objectives (1) and (2), and Operator Splitting Methods for (3).

The methods were first used on a simplified model where one solid reactant decomposes into non-reactive gas. In the absence of ISU experimental data to match, the model was validated using Henderson and Wiecek's experiment [34] describing the thermal decomposition of polymer composite when used as heat-shielding during spacecraft re-entry or for rocket nozzle protection. Our model and Henderson and Wiecek's only differed by the boundary conditions and the description of solid and gas thermal properties, which were taken as functions of temperature for Henderson and Wiecek's instead of constant for our model. Later, the model was extended to include more reactions and a liquid phase, so it described the ISU process more realistically.

7.1 Key findings

We summarize our key findings as follows:

- For a ISU model with n_f fluid components, n_s solid components and k chemical reactions, our model depends on $9 + k(3 + n_f + n_s - 2) + 8n_f + 2n_s$ dimensionless numbers
- Heat conduction is the primary operator controlling the time scale of the process
- The primary parameters controlling the efficiency of the process were the extended Damköhler numbers describing the ratio of chemical rate to heat conduction rate at the heater temperature for each reaction in the model
- In the absence of heat loss and gravity effects, the ISU process was most efficient at a heater temperature for which the minimum of the extended Damköhler numbers of all reactions included in the model was between 10 and 20
- For the numerical method, the standard Iterative Split Operator (ISO) did not perform well due to many convergence failures, whereas the standard Sequential Split Operator (SSO) and the Strang-Marchuk Split Operator (SMSO) gave large discretization errors.
- We have developed a new method, called SSO-CKA, which as smaller discretization error. It simply applies SSO with three decoupled operators: the heat conduction (operator C), the chemical reactions (operator K) and the heat and mass convection (operator A), applied in this order.
- When we applied SSO-CKA with the second-order trapezoidal rule (TR) for solving the chemical reaction operator, we obtained a method which gave smaller discretization errors than FIM for two test cases with no reaction enthalpies and gave discretization errors of the same order as FIM for two test cases with reaction enthalpies $< 1000\ kJ/kg$
- We designed an algorithm, called SSO-CKA-TR-AIM, which is faster and generally more accurate than FIM for simulations with a kinetic model including a large number of components that could be regrouped into a small number of chemical classes for the advection and heat conduction operator

- SSO-CKA worked best for ISU models with no other reaction than pyrolysis reactions. However, we demonstrated that for an ISU model with a non-equilibrium reaction, SSO-CKA could give large discretization error

7.2 Recommendations for kinetic modelling

Kinetic models describing bitumen and kerogen decomposition generally include a large number of components, often more than 20 [1, 8, 12]. However, numerical simulations of ISU with FIM using such large models are very slow. These models are generally lumped into smaller models with 6 components and 3 reactions [24, 53, 56].

Yet, our analysis highlighted the importance of using an accurate kinetic model for describing the chemical reactions. In particular, it is essential to evaluate precisely the activation energy of the decompositions in order to compute the extended Damköhler numbers. Therefore, using a lumped kinetic model for ISU would result in an important loss of accuracy.

This research provided a solution to this problem. The key is to use a kinetic model with as many components and reactions needed to describe accurately the chemical reactions, but to regroup them into a small number of chemical classes for the transport steps. The proposed numerical procedure, called SSO-CKA-TR-AIM, gives a large speed-up with minimum loss of accuracy.

Moreover, reaction enthalpies are often neglected for the modelling of ISU [24, 53, 56]. We demonstrated that they could have an important impact and that they should be measured accurately.

7.3 Recommendations for designing production scheme

The heater temperature is generally chosen arbitrarily, often 350^oC or 400^oC. We demonstrated in this research that there exists a link between the reference length L of the domain and the optimal heater temperature T_H for the efficiency of the process. We demonstrated that in the absence of heat loss and gravity effects, the optimal heater temperature was found between T_{R10}, the temperature for which the minimum extended

Damköhler number in the model is equal to 10, and T_{R20}, the temperature for which the minimum extended Damköhler number in the model is equal to 20. In the case of fixed L, this correlation results in an interval of temperatures that contains the optimal T_H. In the case of fixed T_H, it results in an interval of length that contains the optimal L. This can significantly reduce the number of numerical simulations needed to identify the best production scheme.

7.4 Recommendations for numerical simulation

We demonstrated that SSO-CKA-TR-AIM is generally the best numerical method for the simulation of ISU, since it is fast, accurate and robust. However, due to the splitting error, we do not recommend the use of this method if:

- a reaction enthalpy is larger than 1000 kJ/kg
- the model involves a reaction that is not temperature driven, for example a non-equilibrium reaction

Future work could focus on establishing the reaction enthalpy limit more accurately or designing a method for the case of non-equilibrium reactions.

7.5 Future work

The results of this research can be used to design the heater pattern by reducing the number of numerical experiments necessary to identify the optimal production scheme. However, it should be noted that they have been obtained with a model that does not include (1) heat loss and (2) gravity effects. It has been demonstrated that heat loss to overburden and underburden could have an impact on the efficiency of the process [24] depending on the ratio of formation thickness to well spacing. The wider the well spacing and the thinner the formation then the more important heat loss becomes. In this case, the optimal temperature of the heater could be larger than T_{R20}. Gravity could also have an important impact and should be considered in future work.

We were able to reduce the CPU time of the numerical simulation of ISU with no or limited loss in accuracy. However, the major drawback of the algorithm presented is that SSO-CKA is only first-order accurate. For test cases with large reaction enthalpies, the overall discretization error is driven by the splitting error, and there is no point using a method that is of order > 2 for the chemical solver. Future work could focus on (1) defining the reaction enthalpy limit for which SSO-CKA-TR-AIM is accurate and (2) improving the splitting method for example by using Strang-Marchuk for the coupling between the operators C and K, or by using additive splitting as it is done in Younis and Gerritsen [92].

It should be noted that most of the gain in CPU time was obtained from the lumping of components into chemical classes. This could also be used in a fully coupled approach, by applying a change of variables from the component compositions to the pseudo-component compositions and internal chemical class compositions. Then, since the internal compositions only affect the chemical operator which is fully local, we could reduce the number of variables by applying a Schür complement at the linear level. This technique could decrease the CPU time of the Fully Implicit method, but would not improve its precision.

Appendix A

Deriving the Dimensionless Groups by Inspectional Analysis

The general procedure of scaling the equations that describe a physical process by Inspectional Analysis (IA) involves the introduction of arbitrary scaling factors. They make a linear transformation from dimensional to dimensionless space. The scaling factors are then grouped into dimensionless scaling groups, and their values are selected to minimize the number of groups.

We define the following linear transformations of every variable from the original dimensional space to a general dimensionless space:

$$\begin{aligned} x &= x_1^* x_D + x_2^* & t &= t_1^* t_D + t_2^* \\ S_s &= S_{s1}^* S_{sD} + S_{s2}^* & \omega_R &= \omega_{R1}^* \omega_{RD} + \omega_{R2}^* \\ T &= T_1^* T_D + T_2^* & P &= P_1^* P_D + P_2^* \\ v_g &= v_{g1}^* v_{gD} + v_{g2}^* & q &= q_1^* q_D + q_2^* \end{aligned} \tag{A.1}$$

In these transformations, the scale factors are the "*" quantities and the dimensionless variables are those with a subscript "D". There are 16 scale factors, two for each independent variable (x and t) and depend variable (S_s, ω_R, T, P, v_g, q). The scale factors may be multiplicative (subscript 1) or additive (subscript 2). Since S_s and ω_R are already scaled, we assume $S_{s1}^* = \omega_{R1}^* = 1$ and $S_{s2}^* = \omega_{R2}^* = 0$. This will not change the result. We substitute (A.1) into Equations (2.8), (2.9), (2.10), (2.14), (2.19) and

(2.20) and multiple by selected scale factors to make the equations dimensionless. We obtain :

- Solid decomposition:

$$\frac{\partial}{\partial t_D}\left(\omega_R \rho_{sD} S_s\right) = -\underbrace{\frac{A t_1^*}{S_{s,0}^{n-1}}}_{[1]}\left(\omega_R \rho_{sD} S_s\right)^n \exp\left(\underbrace{-\frac{E_a}{R T_1^*}}_{[2]}\underbrace{\frac{1}{T_D + \frac{T_2^*}{T_1^*}}}_{[3]}\right) \tag{A.2}$$

  with the dimensionless solid density ρ_{sD} defined by:

$$\frac{1}{\rho_{sD}} = \omega_R + (1 - \omega_R)\underbrace{\frac{\rho_R}{\rho_C}}_{[4]} \tag{A.3}$$

- Charred residual conservation

$$\frac{\partial}{\partial t_D}\left(\omega_C \rho_{sD} S_s\right) = -\underbrace{\left(1 - a_G\right)}_{[5]}\frac{\partial}{\partial t_D}\left(\omega_R \rho_{sD} S_s\right) \tag{A.4}$$

- Mass conservation:

$$\frac{\partial \rho_{sD} S_s}{\partial t_D} + \frac{\partial \rho_{gD} S_g}{\partial t_D} = -\underbrace{\frac{v_{g1}^* t_1^*}{\phi x_1^*}}_{[6]}\frac{\partial}{\partial x_D}\left(\rho_{gD}\left(v_{gD} + \underbrace{\frac{v_{g2}^*}{v_{g1}^*}}_{[7]}\right)\right) \tag{A.5}$$

  with the dimensionless gas density ρ_{gD} defined as:

$$\rho_{gD} = \underbrace{\frac{M_G P_1^*}{\rho_R R T_2^*}}_{[8]}\underbrace{\frac{T_2^*}{T_1^*}}_{[3]}\left(\frac{P_D + \frac{P_2^*}{P_1^*}}{T_D + \frac{T_2^*}{T_1^*}}\right)^{\boxed{9}}_{[3]} \tag{A.6}$$

- Darcy's law:

$$v_{gD} = \underbrace{\frac{K_0 P_1^*}{\mu_{g,0} x_1^* v_{g1}^*}}_{[10]}\frac{K_D}{\mu_{gD}}\frac{\partial P_D}{\partial x_D} - \underbrace{\frac{v_{g2}^*}{v_{g1}^*}}_{[7]} \tag{A.7}$$

with the dimensionless permeability:

$$K_D = \underset{[11]}{\exp}\left(-\eta\left(S_s - \underset{[12]}{S_{s,0}}\right)\right) \tag{A.8}$$

and the dimensionless gas viscosity μ_{gD}:

$$\mu_{gD} = 1 + \underset{[13]}{\frac{\delta\mu_g T_1^*}{\mu_{g,0}}}\left(T_D - \underset{[14]}{\frac{T_0 - T_2^*}{T_1^*}}\right) \tag{A.9}$$

- Energy equation:

$$\begin{aligned}\frac{\partial T_D}{\partial t_D} = &-\underset{[15]}{\frac{\phi\rho_R\gamma_R}{(1-\phi)\rho_I\gamma_I}}\left(\rho_{sD}S_s\gamma_{sD} + \rho_{gD}S_g\gamma_{gD}\right)\frac{\partial T_D}{\partial t_D}\\ &-\underset{[6]}{\frac{v_{g1}^* t_1^*}{\phi x_1^*}}\underset{[15]}{\frac{\phi\rho_R\gamma_R}{(1-\phi)\rho_I\gamma_I}}\rho_{gD}\gamma_{gD}\left(v_{gD} + \underset{[7]}{\frac{v_{g2}^*}{v_{g1}^*}}\right)\frac{\partial T_D}{\partial x_D}\\ &-\underset{[16]}{\frac{q_1^* t_1^*}{(1-\phi)\rho_I\gamma_I x_1^* T_1^*}}\frac{\partial q_D}{\partial x_D}\\ &-\underset{[15]}{\frac{\phi\rho_R\gamma_R}{(1-\phi)\rho_I\gamma_I}}\underset{[17]}{\frac{\Delta h_r}{\gamma_R T_1^*}}\frac{\partial\omega_R S_{sD}}{\partial t_D}\\ &-\underset{[15]}{\frac{\phi\rho_R\gamma_R}{(1-\phi)\rho_I\gamma_I}}\left(\underset{[5]}{a_G}\left(\gamma_{sD} - \gamma_{gD}\right)\left(T_D - \underset{[14]}{\frac{T_0 - T_2^*}{T_1^*}}\right)\right)\frac{\partial\omega_R S_{sD}}{\partial t_D}\end{aligned} \tag{A.10}$$

with the dimensionless specific heat capacity of solid and gas defined by:

$$\gamma_{sD} = \underset{[18]}{\left(\omega_R + \omega_C\frac{\gamma_C}{\gamma_R}\right)} \tag{A.11}$$

$$\gamma_{gD} = \underset{[19]}{\frac{\gamma_G}{\gamma_R}} \tag{A.12}$$

- Fourier's law:

$$q_D = -\underset{[20]}{\frac{\kappa_s T_1^*}{q_1^* x_1^*}}\left(1 - \underset{[21]}{\frac{\phi\left(\kappa_s - \kappa_g\right)}{\kappa_s}}\left(1 - S_s\right)\right)\frac{\partial T_D}{\partial x_D} - \underset{[22]}{\frac{q_2^*}{q_1^*}} \tag{A.13}$$

- Oil shale boundary conditions:

$$\begin{aligned}
&\text{- at} \quad x_D = -\frac{x_2^*}{x_1^*}\ \boxed{23} \quad \forall t_D: \\
&T_D = \frac{T_H - T_2^*}{T_1^*}\ \boxed{24} \quad \text{and} \quad v_{gD} = -\frac{v_{g2}^*}{v_{g1}^*}\ \boxed{7} \\
&\text{- at} \quad x_D = \frac{L - x_2^*}{x_1^*}\ \boxed{25} \quad \forall t_D: \\
&q_D = \frac{q_2^*}{q_1^*}\ \boxed{22} \quad \text{and} \quad P_D = \frac{P_0 - P_2^*}{P_1^*}\ \boxed{26}
\end{aligned} \tag{A.14}$$

- Polymer decomposition boundary conditions:

$$\begin{aligned}
&\text{- at} \quad x_D = -\frac{x_2^*}{x_1^*}\ \boxed{23} \quad \forall t_D: \\
&q_D = \frac{\epsilon_s \sigma T_1^{*4}}{q_1^*}\ \boxed{27} \left(\left(\frac{T_H - T_2^*}{T_1^*}\ \boxed{24} + \frac{T_2^*}{T_1^*}\ \boxed{3} \right)^4 - \left(T_D + \frac{T_2^*}{T_1^*}\ \boxed{3} \right)^4 \right) - \frac{q_2^*}{q_1^*}\ \boxed{22} \\
&\text{and} \quad P_D = \frac{P_0 - P_2^*}{P_1^*}\ \boxed{26} \\
&\text{- at} \quad x_D = \frac{L - x_2^*}{x_1^*}\ \boxed{25} \quad \forall t_D: \\
&q_D = -\frac{\epsilon_s \sigma T_1^{*4}}{q_1^*}\ \boxed{27} \left(T_D + \frac{T_2^*}{T_1^*}\ \boxed{4} \right)^4 - \frac{q_2^*}{q_1^*}\ \boxed{22} \quad \text{and} \quad P_D = \frac{P_0 - P_2^*}{P_1^*}\ \boxed{26}
\end{aligned} \tag{A.15}$$

- Initial conditions:

$$\begin{aligned}
&S_{sD} = S_{s0}\ \boxed{12} \\
&P_D = \frac{P_0 - P_2^*}{P_1^*}\ \boxed{26} \ \text{at} \quad t_D = -\frac{t_2^*}{t_1^*}\ \boxed{28} \quad \forall x_D \\
&T_D = \frac{T_0 - T_2^*}{T_1^*}\ \boxed{14}
\end{aligned} \tag{A.16}$$

The scaling groups that appear in these equations are numbered (e.g., $\boxed{1}$). Each equation is dimensionless, and the 28 scaling groups are dimensionless too. The next task is to reduce the number of groups.

A large number of scaling groups can be set to zero by chosing the additive factors to be zero or to the initial or final value of the variable. Therefore, we choose:

$$\begin{aligned} x_2^* &= 0 & t_2^* &= 0 \\ T_2^* &= T_0 & P_2^* &= 0 \\ v_{g2}^* &= 0 & q_2^* &= 0 \end{aligned} \tag{A.17}$$

Then, the groups 7, 9, 14, 22, 23 and 28 are equal to zero. Next, we need to define the multiplicative factors. Setting scaling groups to one usually leaves the final formulation in a compact form that is generally free of constant. Therefore, we choose:

$$\begin{aligned} x_1^* &= L \\ T_1^* &= \Delta T = T_H - T_0 & P_1^* &= P_0 \\ v_{g1}^* &= \frac{K_0 P_0}{\mu_{g,0} L} & q_1^* &= \kappa_s \frac{\Delta T}{L} \end{aligned} \tag{A.18}$$

Thus, the groups 10, 20, 24, 25, and 26 are equal to one. For the multiplicative factor t_1^*, various time scales such as the time scale of the chemical reaction or the time scale of heat conduction could be chosen. Here we chose to normalize our time to the time taken for heat to diffuse at initial conditions. This has the advantage that group 16 in Equation A.10 is set to 1 i.e. the rate of change of heat transfer with distance is 1 at initial time.

$$t_1^* = \tau = \frac{(1-\phi)\,\rho_I \gamma_I L^2}{\kappa_s} \Rightarrow \text{Group } 16 = 1 \tag{A.19}$$

Note that the order of the reaction n and the order of the solid mobility parameter η are two additional parameter. Therefore there remain 16 groups that are not yet defined. These remaining dimensionless groups are no longer arbitrary. The system depends only

on these groups and the order of reaction. The groups are:

$$
\begin{aligned}
&D_K = D_1 S_{s,0}^{n-1} = \frac{A\,(1-\phi)\,\rho_I \gamma_I}{\kappa_s} && N_a = D_2 = \frac{E_a}{R\Delta T} && T_0^* = D_3 = \frac{T_0}{\Delta T} \\
&\rho_C^* = \frac{1}{D_4} = \frac{\rho_C}{\rho_R} && a_G = D_5 && \\
&L_e = \frac{1}{D_6} = \frac{\phi \mu_{g,0} \kappa_s}{K_0 P_0\,(1-\phi)\,\rho_I \gamma_I} && \rho_G^* = D_8 = \frac{M_G P_0}{\rho_s R T_0} && \eta = D_{11} \\
&S_{s0} = D_{12} && \delta\mu_g^* = D_{13} = \frac{\delta \mu_g \Delta T}{\mu_{g,0}} && \\
&\Gamma_R^* = D_{15} = \frac{\phi \rho_R \gamma_R}{(1-\phi)\,\rho_I \gamma_I} && \Delta h_r^* = D_{17} = \frac{\Delta h_r}{\gamma_s \Delta T} && \gamma_C^* = D_{18} = \frac{\gamma_C}{\gamma_R} \\
&\gamma_G^* = D_{19} = \frac{\gamma_G}{\gamma_R} && \Delta\kappa_s^* = D_{21} = \phi \frac{\kappa_s - \kappa_g}{\kappa_s} && \\
&\epsilon^* = D_{27} = \frac{\epsilon_s \sigma \Delta T^3 L}{\kappa_s} &&&&
\end{aligned}
\tag{A.20}
$$

The dimensionless groups satisfy the scaling requirements for the one-dimensional problem. We can demonstrate that they are independent by using the method of elementary row operations descibed in [78]. We obtain the following form of the dimensionless equation:

- Solid decomposition:

$$
\frac{\partial}{\partial t_D}\left(\omega_R S_s\right) = -\frac{D_K}{S_{s,0}^{n-1}}\left(\omega_R S_s\right) \exp\left(-\frac{N_a}{T_D + T_0^*}\right) \tag{A.21}
$$

$$
\frac{1}{\rho_{sD}} = \omega_R + \frac{\omega_C}{\rho_C^*} \tag{A.22}
$$

- Charred residual conservation:

$$
\frac{\partial}{\partial t_D}\left(\omega_C S_s\right) = -a_C \frac{\partial}{\partial t_D}\left(\omega_R S_s\right) \tag{A.23}
$$

- Total mass conservation:

$$
\frac{\partial}{\partial t_D}\left(\rho_{sD} S_s\right) + \frac{\partial}{\partial t_D}\left(\rho_{gD} S_g\right) = -\frac{1}{L_e}\frac{\partial}{\partial x_D}\left(\rho_{gD} v_{gD}\right) \tag{A.24}
$$

$$
\rho_{gD} = \rho_G^*\left(\frac{P_D}{T_D + T_0^*}\right) \tag{A.25}
$$

- Darcy's law:

$$v_{gD} = \frac{K_D}{\mu_{gD}} \frac{\partial P_D}{\partial x_D} \tag{A.26}$$

$$K_D = \exp\left(-\eta \left(S_s - S_{s,0}\right)\right) \tag{A.27}$$

$$\mu_{gD} = 1 + \delta \mu_g^* \left(T_D - T_0^*\right) \tag{A.28}$$

- Energy equation:

$$\begin{aligned} \frac{\partial T_D}{\partial t_D} = & -\Gamma_R^* \left(\rho_{sD} S_s \gamma_{sD} + \rho_{gD} S_g \gamma_{gD}\right) \frac{\partial T_D}{\partial t_D} \\ & - \frac{\Gamma_R^*}{L_e} \rho_{gD} v_{gD} \gamma_{gD} \frac{\partial T_D}{\partial x_D} \\ & - \frac{\partial q_D}{\partial x_D} \\ & - \Gamma_R^* \left(\Delta h_r^* + a_G \left(\gamma_{sD} - \gamma_{gD}\right) T_D\right) \frac{\partial \omega_R S_s}{\partial t_D} \end{aligned} \tag{A.29}$$

$$\gamma_{sD} = \omega_R + \omega_C \gamma_C^* \tag{A.30}$$

$$\gamma_{gD} = \gamma_G^* \tag{A.31}$$

- Fourier's law:

$$q_D = -\left(1 - \Delta \kappa_g^* S_g\right) \frac{\partial T_D}{\partial x_D} \tag{A.32}$$

- Oil shale boundary conditions:

$$\begin{aligned} & \text{- at} \quad x_D = 0 \quad \forall t_D : \\ & T_D = 1 \quad \text{and} \quad v_{gD} = 0 \\ & \text{- at} \quad x_D = 1 \quad \forall t_D : \\ & q_D = 0 \quad \text{and} \quad P_D = 1 \end{aligned} \tag{A.33}$$

- Polymer decomposition boundary conditions:

$$\begin{aligned}
&\text{- at} \quad x_D = 0 \quad \forall t_D : \\
&q_D = \epsilon^* \left(1 + T_0^*\right)^4 - \epsilon^* \left(T_D + T_0^*\right)^4 \quad \text{and} \quad P_D = 1 \\
&\text{- at} \quad x_D = 1 \quad \forall t_D : \\
&q_D = -\epsilon^* \left(T_D + T_0^*\right)^4 \quad \text{and} \quad P_D = 1
\end{aligned} \tag{A.34}$$

- Initial conditions:

$$\begin{aligned}
&S_s = S_{s0} \\
&P_D = 1 \quad \text{at} \quad t_D = 0 \quad \forall x_D \\
&T_D = 0
\end{aligned} \tag{A.35}$$

Appendix B

Numerical simulation of advection-heat diffusion-reaction problems using the Finite Volume Method

In this appendix, we describe the numerical method used for the simulation of advection-heat diffusion-reaction problems and implemented in EXTEND, the C++ simulator developed for this work (source code given in attached CDROM). EXTEND uses an overall molar composition formulation for the fluid description. To distinguish molar from mass quantities, we used $\hat{}$ for the molar quantities.

To simplify the writing of the system of equations, we define M_j the mole accumulation of component j B.1 and E the total energy accumulation B.2 in the domain:

$$M_j\left(P,T,S_p,\xi_{p,j}\right)=\phi\sum_p \xi_{p,j}\hat{\rho}_p S_p \tag{B.1}$$

$$E\left(P,T,S_p,\xi_{p,j}\right)=\left(1-\phi\right)\rho_I u_I+\phi\sum_p \hat{\rho}_p\hat{u}_p S_p \tag{B.2}$$

where ϕ is the rock porosity, S_p, $\hat{\rho}_p$ and $\hat{u}_p$ are the saturation, molar density and molar internal energy of phase p, $\xi_{p,j}$ is the mole fraction of component j in phase p, and ρ_I and u_I are the rock density and internal energy. The mass flow F_j of component j and

the total enthalpy flow F_h are given by:

$$F_j\left(P,T,S_p,\xi_{p,j}\right) = -\sum_p \xi_{p,j}\hat{\rho}_p\lambda_p K\nabla\left(P-\rho_p g D\right) \tag{B.3}$$

$$F_h\left(P,T,S_p,\xi_{p,j}\right) = -\sum_p \hat{h}_p\hat{\rho}_p\lambda_p K\nabla\left(P-\rho_p g D\right) \tag{B.4}$$

where g is the gravitational constant, D is the depth, K is the rock permeability, and ρ_p and $\hat{h}_p$ are the mass density and the molar internal enthalpy of phase p. The mobility λ_p of phase p is defined by:

$$\lambda_p = \frac{k_{rp}}{\mu_p} \tag{B.5}$$

where $k_{r,p}$ and μ_p are the relative permeability and the viscosity of phase p. Finally, the mass reaction rate R_j of component j and the total enthalpy of reaction R_h are given by:

$$R_j\left(P,T,S_p,\xi_{p,j}\right) = \sum_i \hat{a}_{ij}A_i\exp\left(-\frac{E_{ai}}{RT}\right)\hat{C}_i \tag{B.6}$$

$$R_h\left(P,T,S_p,\xi_{p,j}\right) = \sum_i \Delta\hat{h}_{ri}A_i\exp\left(-\frac{E_{ai}}{RT}\right)\hat{C}_i \tag{B.7}$$

where $\hat{a}_{i,j}$ is the molar stoichiometric coefficient for component j as a product ($\hat{a}_{i,j} > 0$) or a reactant ($\hat{a}_{i,j} < 0$), A_i and E_{ai} are the frequency factor and the activation energy of reaction i, R is the universal gas constant, $\hat{C}_i$ is the mole concentration of the reactant X_i and $\Delta\hat{h}_{ri}$ the molar enthalpy of reaction i.

So the system of equations for an advection-heat diffusion-reaction problem is:

$$\frac{\partial}{\partial t}M_j\left(P,T,S_p,\xi_{p,j}\right) = -\nabla F_j(P,T,S_p,\xi_{p,j}) + R_j\left(P,T,S_p,\xi_{p,j}\right) \tag{B.8}$$

$$\frac{\partial}{\partial t}E\left(P,T,S_p,\xi_{p,j}\right) = \nabla\left(\kappa\nabla T\right) - \nabla F_h(P,T,S_p,\xi_{p,j}) + R_h\left(P,T,S_p,\xi_{p,j}\right) \tag{B.9}$$

This system has $n_t + 1$ equations, where n_t is the total number of components. Several representations of the fluid are possible. With the natural variables formulation, we represent the fluid with the variables P, T, S_p and $\xi_{p,j}$. This system includes $2 + n_p + n_p \times n_t$ variables, where n_p is the number of phases. To close the system, we need $1 + n_p + n_t \times (n_p - 1)$ additional equations. They are:

- (1) $\sum_p S_p = 1$

- (n_p) $\sum_j \xi_{p,j} = 1$
- $(n_t \times (n_p - 1))$ equilibrium constraints for components j in phase p and $p+1$

This formulation has the advantage of representing the fluid with the natural saturation variables. However, the equilibrium equations are only valid if $S_p > 0$. Otherwise, they need to be replaced by $S_p = 0$ and $\xi_{p,j} = cst$. This switch of equations could generate convergence problems when a phase appears or disappears. To remedy this, we use the overall molar composition formulation.

B.1 Overall molar composition formulation

B.1.1 Overall molar fractions

We define the overall molar fraction ζ_j of component j :

$$\zeta_j = \frac{\sum_p \xi_{p,j} \hat{\rho}_p S_p}{\sum_p \hat{\rho}_p S_p} \tag{B.10}$$

For the overall molar composition formulation, the fluid is represented by $P, T, \zeta_1, ..., \zeta_{n_t}$. This system includes $n_t + 2$ variables. To close it, we simply use $\sum \zeta_j = 1$.

With this formulation, S_p and $\xi_{j,p}$ are no longer variables but are function of $P, T, \zeta_1, ..., \zeta_{n_t}$. In practice, the saturations and phase compositions are obtained from $P, T, \zeta_1, ..., \zeta_{n_t}$ by an algorithm called a flash computation. In the next section, we describe the method for $n_p = 2$ and an equilibrium modelled by K-values.

B.1.2 K-values two-phase flash computation

Here we assume that the system contains only two phases, for example a gas phase g and an oil phase o. Therefore, for each component j, the overall molar composition ζ_j is given by:

$$\zeta_j = \xi_{o,j} \Pi_o + \xi_{g,j} \Pi_g \tag{B.11}$$

where Π_p is the molar fraction of phase p:

$$\Pi_p = \frac{\hat{\rho}_p S_p}{\hat{\rho}_g S_g + \hat{\rho}_o S_o} \tag{B.12}$$

The equilibrium equation for component j is given by:

$$\xi_{g,j} = K_j \xi_{o,j} \tag{B.13}$$

Therefore, the phase composition are given by:

$$\begin{aligned} \xi_{o,j} &= \frac{z_j}{1 + \Pi_g \left(K_j - 1\right)} \\ \xi_{g,j} &= \frac{K_j z_j}{1 + \Pi_g \left(K_j - 1\right)} \end{aligned} \tag{B.14}$$

Moreover, the phase compositions are constrained by the equations:

$$\sum_j \xi_{o,j} = \sum_j \xi_{g,j} = 1 \tag{B.15}$$

Therefore, the gas molar fraction can be found by solving the Rashford-Rice equation:

$$g\left(\Pi_g\right) = \sum \left(\xi_{g,j} - \xi_{o,j}\right)) = \sum \frac{\left(K_j - 1\right) z_j}{1 + \Pi_g \left(K_j - 1\right)} \tag{B.16}$$

An efficient algorithm to solve Equation B.16 can be found in Leibovici and Neoschil [54]. When Π_g has been obtained, we can compute the phase composition using Equation B.14. Then, we can compute the molar density and finally, the phase saturations using Equation B.12.

B.2 Finite Volume Method

B.2.1 Finite Volume Discretization

The Finite Volume Method is a discretization technique for solving PDEs which uses a volume integral formulation of the problem with a finite partitioning set of volumes to discretize the equations. In this work, we use Cartesian grids (figure B.1).

For cell centered grids, the variables are defined at the cell centres. We then assume that all variables and physical quantities are piecewise constant in each cell. Therefore,

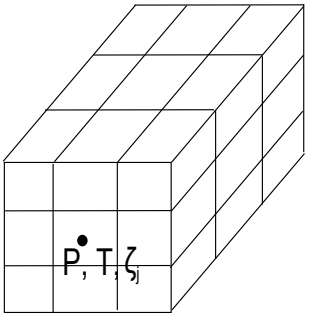

FIGURE B.1: Cartesian grid. For cell centered grids, the variables are defined at the cell centres.

the discrete formulation of Equations B.8 and B.9 for cell i is given by:

$$\begin{aligned} V_i \frac{d}{d_t} M_j &= -\sum_{ei} F_j.n_{ei}S_{ei} + V_i R_j \\ V_i \frac{d}{d_t} E &= \sum_{ei} \kappa \nabla T.n_{ei}S_{ei} - \sum_{ei} F_h.n_{ei}S_{ei} + V_i R_h \end{aligned} \tag{B.17}$$

where V_i is the volume of the cell i, and n_{ei} and S_{ei} are the normal and the surface of the edge ei of cell i. To avoid instability oscillations, we use upstream weighted flows, so that the mass and energy flows between the cells $ei-$ and $ei+$ of an edge ei are given by:

$$\begin{aligned} F_j.n_{ei}dS_{ei} &= -\sum_p \xi_{p,j}\hat{\rho}_p\lambda_p T^f_{rei}\left(P_{ei+} - P_{ei-} + \rho_{p,ei}g\Delta D\right) \\ F_h.n_{ei}dS_{ei} &= -\sum_p \hat{h}_p\hat{\rho}_p\lambda_p T^f_{rei}\left(P_{ei+} - P_{ei-} + \rho_{p,ei}g\Delta D\right) \\ \nabla T.n_{ei}dS_{ei} &= T^e_{rei}\left(T_{ei+} - T_{ei-}\right) \end{aligned} \tag{B.18}$$

where $\xi_{p,j}$, $\hat{\rho}_p$, λ_p and $\hat{h}_p$ are taken at cell $up = ei+$ if $P_{ei+} > P_{ei-}$, $up = ei-$ otherwise. T^f_{rei} and T^e_{rei} are the flow and energy transmissibility for edge ei:

$$\begin{aligned} T^f_{rei} &= \frac{KS_{ei}}{l_{ei}} \\ T^e_{rei} &= \frac{\kappa S_{ei}}{l_{ei}} \end{aligned} \tag{B.19}$$

where l_{ei} is the distance between the centres of the cell $ei-$ and $ei+$. For simplicity, the mass density in the gravity term is averaged between $ei+$ and $ei-$

To obtain the time-space discretized problem, the system of equations B.17 is integrated between t^n and $t^{n+1} = t^n + \Delta t$. The variations of the accumulation terms M_j and E are then calculated between time $n+1$ and time n. However, the choice between using

each variable at time n or $n+1$ remains for the operators F_j, F_h, R_j, R_h and $\nabla(\kappa\nabla T)$. For the explicit method, all variables are taken at time n. In this case, the values of the variables at time $n+1$ can be directly computed from the values at time n, so that the time integration is computationally cheap. However, very small time steps are generally required for stability. To avoid this issue, we only consider integration schemes where:

- the reaction term is treated implicitly
- the pressure term in the flow is treated implicitly

Therefore, the time-space discretized problem is given by:

$$\begin{aligned} V_i\frac{M_j^{n+1}-M_j^n}{\Delta t} &= -\sum_{ei,p}\xi_{p,j}^k\hat{\rho}_p^k\lambda_{p,}^k T_{rei}^f\left(P_{ei+}^{n+1}-P_{ei-}^{n+1}+\rho_{p,ei}^k g\Delta D\right) \\ &\quad + V_i R_j^{n+1} \\ V_i\frac{E^{n+1}-E^n}{\Delta t} &= -\sum_{ei,p}\hat{h}_{p,j}^k\hat{\rho}_p^k\lambda_p^k T_{rei}^f\left(P_{ei+}^{n+1}-P_{ei-}^{n+1}+\rho_{p,ei}^k g\Delta D\right) \\ &\quad + \sum_{ei}T_{rei}^e\left(T_{ei+}^k-T_{ei-}^k\right)+V_i R_h^{n+1} \end{aligned} \tag{B.20}$$

with $k=n+1$ or $k=n$. In this work, we consider three possible methods: the Fully Implicit Method (FIM), the IMplicit Pressure Explicit Saturation (IMPES) method, and the Adaptive Implicit Method (AIM). In each case, the system of non-linear equations B.20 is solved using Newton's method (Section B.2.5).

B.2.2 Fully Implicit Method

The Fully Implicit Method takes every variables in each operator implicitly ($k=n+1$):

$$\begin{aligned} V_i\frac{M_j^{n+1}-M_j^n}{\Delta t} &= -\sum_{ei,p}\xi_{p,j}^{n+1}\hat{\rho}_p^{n+1}\lambda_{p,}^{n+1}T_{rei}^f\left(P_{ei+}^{n+1}-P_{ei-}^{n+1}+\rho_{p,ei}^{n+1}g\Delta D\right) \\ &\quad + V_i R_j^{n+1} \\ V_i\frac{E^{n+1}-E^n}{\Delta t} &= -\sum_{ei,p}\hat{h}_{p,j}^{n+1}\hat{\rho}_p^{n+1}\lambda_p^{n+1}T_{rei}^f\left(P_{ei+}^{n+1}-P_{ei-}^{n+1}+\rho_{p,ei}^{n+1}g\Delta D\right) \\ &\quad + \sum_{ei}T_{rei}^e\left(T_{ei+}^{n+1}-T_{ei-}^{n+1}\right)+V_i R_h^{n+1} \end{aligned} \tag{B.21}$$

FIM is the most common approach for thermal reservoir simulations. This method is unconditionally stable and can take very large time-steps, but is computationally expensive. Indeed, each non-linear iteration in Newton's algorithm (Section B.2.5) solves a linear system that can be quite large, especially for models with a large number of component n_t.

B.2.3 IMPES method

The IMPES method treats the saturation (and composition and temperature) terms in the flows explicitly ($k = n$):

$$\begin{aligned} V_i \frac{M_j^{n+1} - M_j^n}{\Delta t} &= -\sum_{ei,p} \xi_{p,j}^n \hat{\rho}_p^n \lambda_{p,}^n T_{rei}^f \left(P_{ei+}^{n+1} - P_{ei-}^{n+1} + \rho_{p,ei}^n g \Delta D \right) \\ &\quad + V_i R_j^{n+1} \\ V_i \frac{E^{n+1} - E^n}{\Delta t} &= -\sum_{ei,p} \hat{h}_{p,j}^n \hat{\rho}_p^n \lambda_p^n T_{rei}^f \left(P_{ei+}^{n+1} - P_{ei-}^{n+1} + \rho_{p,ei}^n g \Delta D \right) \\ &\quad + \sum_{ei} T_{rei}^e \left(T_{ei+}^n - T_{ei-}^n \right) + V_i R_h^{n+1} \end{aligned} \tag{B.22}$$

For the same time-step, the IMPES formulation is computationally more efficient than FIM. Indeed the temperature and the overall compositions at time $n+1$ only appear in the accumulation terms of Equation B.22. Therefore, they only appear in the diagonal part of the Jacobian matrices used for the linear system solved at each Newton's iteration (Section B.2.5). This means that T^{n+1} and $\zeta_1^{n+1} ... \zeta_{n_t}^{n+1}$ can be directly obtained from P^{n+1}. The linear system can therefore be reduced to a system with only one variable by block i (P_i^{n+1}). Also IMPES is more accurate than FIM (introduces less numerical dispersion). However, treating some variables explicitly introduces limits on the size of the stable time-step that can be taken.

To obtain a stability criteria, we use the Courant-Friedrich-Levy (CFL) condition for incompressible two-phase flow. In this case, we obtain a saturation equation by adding the component conservation equations:

$$\frac{\partial}{\partial t} \left(\phi \hat{\rho}_g S_g + \hat{\rho}_o S_o \right) = -\nabla \left(\hat{\rho}_g v_g + \hat{\rho}_o v_o \right) \tag{B.23}$$

We further assume that we can neglect the phase interactions for the purpose of the stability analysis. Equation B.23 becomes:

$$\begin{aligned} \frac{\partial}{\partial t}\left(\phi\hat{\rho}_g S_g\right) &= -\nabla\left(\hat{\rho}_g v_g\right) \\ \frac{\partial}{\partial t}\left(\phi\hat{\rho}_o S_o\right) &= -\nabla\left(\hat{\rho}_o v_o\right) \end{aligned} \tag{B.24}$$

Since the flow is assumed incompressible, $v_t = cst$ and the gas velocity can be obtained as:

$$v_g = f_g v_t \tag{B.25}$$

where f_g is the gas fractional mobility:

$$f_g = \frac{\lambda_g}{\lambda_g + \lambda_o}\left(1 + \frac{\lambda_o\left(\rho_g - \rho_o\right) g\Delta D}{Q_t} T^f_{rei}\right) \tag{B.26}$$

where Q_t is the total flow of of velocity v_t across the surface of the finite volume i. Therefore, we obtain the saturation equation:

$$\frac{\partial S_g}{\partial t} = -\frac{v_t}{\phi} f'_g \nabla S_g \tag{B.27}$$

By applying the Von Neumann stability analysis to Equation B.27, we obtain the following CFL stability condition for saturations:

$$\left(\frac{Q_t}{V_i\phi} f'_g\right)\Delta t < 1 \tag{B.28}$$

The composition equation is given by

$$\frac{\partial}{\partial t}\left(\phi\xi_{g,j}\hat{\rho}_g S_g + \phi\xi_{o,j}\hat{\rho}_o S_o\right) = -\nabla\left(\xi_{g,j}\hat{\rho}_g v_g + \xi_{o,j}\hat{\rho}_o v_o\right) \tag{B.29}$$

We assume that $K_j = \frac{\xi_{g,j}}{\xi_{o,j}}$ varies slowly with pressure and temperature for the purpose of the stability analysis. By substituting Equation B.24 into Equation B.29, we obtain:

$$\frac{\partial \xi_{o,j}}{\partial t}\left(\phi K_j\hat{\rho}_g S_g + \phi\hat{\rho}_o S_o\right) = -\nabla\left(\xi_{o,j}\right)\left(\hat{\rho}_g v_g + \xi_{o,j}\hat{\rho}_o v_o\right) \tag{B.30}$$

By applying the Von Neumann stability analysis, we obtain the following CFL stability condition for compositions:

$$\left(\frac{1}{V_i\phi}\frac{\xi_{o,j}\hat{\rho}_o Q_o + \xi_{g,j}\hat{\rho}_g Q_g}{\xi_{o,j}\hat{\rho}_o S_o + \xi_{g,j}\hat{\rho}_g S_g}\right)\Delta t < 1 \tag{B.31}$$

where Q_g and Q_o are the total gas and oil flow across the surface of the finite volume i.

Finally, we obtain the temperature equation by substituting Equation B.27 in Equation B.9:

$$\left((1-\phi)\,\rho_I\gamma_I + \phi\hat{\rho}_o S_o\hat{\gamma}_o + \phi\hat{\rho}_g S_g\hat{\gamma}_g\right)\frac{\partial T}{\partial t} = -\left(\hat{\rho}_o v_o\hat{\gamma}_o + \hat{\rho}_g v_g\hat{\gamma}_g\right)\frac{\partial T}{\partial x} + \kappa\frac{\partial^2 T}{\partial x^2} \tag{B.32}$$

By applying the Von Neumann stability analysis, we obtain the following CFL stability condition for temperature:

$$\left[\frac{1}{V_i\phi}\left(\frac{\hat{\rho}_o\hat{\gamma}_o Q_o + \hat{\rho}_g\hat{\gamma}_g Q_g}{\hat{\rho}_o S_o\hat{\gamma}_o + \hat{\rho}_g S_g\hat{\gamma}_g} + \frac{2T^e_{rei}}{\hat{\rho}_o S_o\hat{\gamma}_o + \hat{\rho}_g S_g\hat{\gamma}_g}\right)\right]\Delta t < 1 \tag{B.33}$$

Therefore, the time-step used in an IMPES simulation is constrained by Equations B.28, B.31 and B.33. The CFL conditions are locally defined and during a simulation, they are large for only a few cells (the one near the saturation or temperature front). However, since the time-step is the same for all finite volumes, it is restricted by the less stable cell. To solve this problem, we can use the Adaptive Implicit Methods.

B.2.4 Adaptive Implicit Method

The Adaptive Implicit Method (AIM) combines the two previous approaches by treating some cells in the discrete model with FIM and other with IMPES using the CFL conditions as a switching criterion. If all CFL conditions related to a cell are smaller than 0.9, the cell is treated with IMPES. Otherwise, it is treated with FIM. For robustness, the cells containing a well are always treated implicitly.

AIM is very efficient for advection problems with a large number of components. However, for thermal reactive problems, two issues appear:

- For stiff reactions and/or fast phase transfers, the CFL conditions for incompressible two-phase flow may not be representative of the stability of the problem

- The thermal conduction part in Equation B.33 is generally large, and a doubling of the space resolution increases it by a factor 4

AIM could be applied with various integration schemes such as IMPTES (IMplicit Pressure and Temperature Explicit Saturations) or IMPSAT (IMplicit Pressure and Saturation explicit rest), but in this work we only considered AIM with IMPES.

B.2.5 Newton's method

For FIM, IMPES or AIM, integrating between time n and $n+1$ implies solving the non-linear system of Equations B.20. We defined R the residual:

$$R(X) = \begin{pmatrix} V_i \frac{M_j^{n+1} - M_j^n}{\Delta t} + \sum_{ei} F_j . n_{ei} S_{ei} - V_i R_j \\ V_i \frac{E^{n+1} - E^n}{\Delta t} - \sum_{ei} \kappa \nabla T . n_{ei} S_{ei} - \sum_{ei} F_h . n_{ei} S_{ei} - V_i R_h \end{pmatrix} = 0 \tag{B.34}$$

where $X = \left(P^{n+1}, T^{n+1}, \zeta_1^{n+1}, ...\zeta_{n_t}^{n+1}\right)$ is the set of variables. If X_r is a root of Equation B.34, X_0 an estimate of X_r, and $h = X_r - X_0$:

$$0 = R(X_r) = R(X_0 + h) \approx R(X_0) + \frac{\partial R}{\partial X}(X_k) . h \tag{B.35}$$

Therefore:

$$h \approx -\left(\frac{\partial R}{\partial X}(X_k)\right)^{-1} . R(X_0) \tag{B.36}$$

The matrix $J = \frac{\partial R}{\partial X}$ is the Jacobian matrix of the system. For a problem with n_b grid cells (or blocks) and n_t component, J is of size $m \times m$ where $m = n_b \times (n_t + 2)$.

The Newton's algorithm for finding a root of equation B.34 is defined as:

1. Choose initial estimation $X = X_0$, a tolerance $\epsilon > 0$ and a maximum number of iterations k_{max}
2. Compute $R(X_k)$
3. If $||R(X_k)|| < \epsilon$, return X_k
4. Compute $J(X_k)$ and solve $h = -J^{-1} . R$
5. $X_{k+1} = X_k + h$

6. if $k+1 = k_{max}$, return X_{k+1}

7. $k = k+1$ and go back to 2

By a Taylor series expansion at order 2, it can be easily demonstrated that the Newton's method converges quadratically if the Jacobian of R is non-singular for every X between X_k and X_r [47]. Otherwise, Newton's method is said to have overshot. To avoid this, the solution h obtained at step 4 is usually damped by a factor α so that $h_{damp} = \alpha h < h_{max}$. In EXTEND, we use $h_{max} = 0.1$.

B.3 Operator Splitting Methods

Here we recall the definition of the splitting methods described in Chapter 4 and give some implementation details. The methods are described on a simple problem of the form:

$$\begin{cases} \dfrac{\partial u}{\partial t} = A.u + K.u, \quad t \in (0,T]\,. \\ u(0) = u_0 \end{cases} \tag{B.37}$$

where A is the advection-heat diffusion operator and K the chemical reaction operator. We also define the heat diffusion operator C and the heat and mass convection operator $A' = A - C$.

B.3.1 Sequential Split Operator

The Sequential Split Operator (SSO) solves each operator sequentially as if they were following each other in time. The order of the splitting can have a significant impact on the precision of the method. In this work, we consider three different SSO methods:

- SSO-AK

$$\begin{cases} \dfrac{\partial u^*}{\partial t} = A.u^*, & t \in \left[t^n, t^{n+1}\right],\ u^*(t^n) = u(t^n) \\ \dfrac{\partial u^{n+1}}{\partial t} = K.u^{n+1}, & t \in \left[t^n, t^{n+1}\right],\ u^{n+1}(t^n) = u^*(t^{n+1}) \end{cases} \tag{B.38}$$

- SSO-KA

$$\begin{cases} \dfrac{\partial u^*}{\partial t} = K.u^*, & t \in \left[t^n, t^{n+1}\right], u^*(t^n) = u(t^n) \\ \dfrac{\partial u^{n+1}}{\partial t} = A.u^{n+1}, & t \in \left[t^n, t^{n+1}\right], u^{n+1}(t^n) = u^*(t^{n+1}) \end{cases} \tag{B.39}$$

- SSO-CKA

$$\begin{cases} \dfrac{\partial u^*}{\partial t} = C.u^*, & t \in \left[t^n, t^{n+1}\right], u^*(t^n) = u(t^n) \\ \dfrac{\partial u^{**}}{\partial t} = K.u^{**}, & t \in \left[t^n, t^{n+1}\right], u^{**}(t^n) = u^*(t^{n+1}) \\ \dfrac{\partial u^{n+1}}{\partial t} = A'.u^{n+1}, & t \in \left[t^n, t^{n+1}\right], u^{n+1}(t^n) = u^{**}(t^{n+1}) \end{cases} \tag{B.40}$$

For non-linear operators, each substep of the method defines a system of non-linear equations, which can be solved using Newton's method. The initial guess for the Newton's iterations can have a large impact on the performance of the method. If the initial guess is far from the final solution, it can lead to convergence failure. We observed in our numerical experiments for the ISU process that this was particularly true for the advection operator. The solution of the chemical reaction steps could have very large pressures, far from the solution of the advection step. Therefore, in our implementation, we use the solution of the last advection step as an initial guess. This solution is saved at the end of each advection step to be used for the next time-step.

B.3.2 Strang-Marchuk Split Operator

In this procedure, the transport equation is first solved over half a step, then the chemistry operator is solved over the entire time-step. Finally, the solution is obtained after solving another transport step over half a time-step:

$$\begin{cases} \dfrac{\partial u^*}{\partial t} = A.u^*, & t \in \left[t^n, t^{n+1/2}\right], u^*(t^n) = u(t^n) \\ \dfrac{\partial u^{**}}{\partial t} = K.u^{**}, & t \in \left[t^n, t^{n+1}\right], u^{**}(t^n) = u^*(t^{n+1/2}) \\ \dfrac{\partial u^{n+1}}{\partial t} = A.u^{n+1}, & t \in \left[t^{n+1/2}, t^{n+1}\right], u^{n+1}(t^n) = u^{**}(t^{n+1}) \end{cases} \tag{B.41}$$

In our implementation, we solve the chemistry step with two time-steps of size $\Delta t/2$. This is equivalent to using the Alternating Split Operator (ASO) method proposed by

Kaluarachchi and Morshed [44], but with a half time-step. This way SMSO, applied with a time-step of $2 \times \Delta t$ computes the same number of transport and chemical steps as SSO-AK and SSO-KA with Δt. Therefore, we always compare the result with a time-step for SMSO twice the size as for SSO-AK and SSO-KA.

B.3.3 Iterative Split Operator

The Iterative Split Operator (ISO) method tries to reduce the splitting error by iterating over the splitting scheme. Unlike SNIA, each sub-step of an iterative scheme solves an approximation to the fully coupled PDE system so that the iteration could converge toward the solution of the fully coupled system. For the first step, the chemical reaction is taken explicitly and the transport operator is solved using FIM. For the second step, the chemical reaction is solved with FIM with the transport operator taken explicitly:

$$\begin{aligned}
&\frac{\partial u^*_{2i+1}}{\partial t} = A.u^*_{2i+1} + K.u^*_{2i} \qquad t \in \left[t^n, t^{n+1}\right].\\
&u^*_{2i+1}(t^n) = u_n(t^n)\\
&\frac{\partial u^*_{2i+2}}{\partial t} = A.u^*_{2i+1} + K.u^*_{2i+2} \quad t \in \left[t^n, t^{n+1}\right].\\
&u^*_{2i+2}(t^n) = u_n(t^n)
\end{aligned} \tag{B.42}$$

for $i = 0, 1, ..., m$ or until convergence.

For non-linear problems, an additional difficulty arises from the fact that each substep i defines a system of non-linear equations, which we solve with Newton's method. Due to the instability issues induced by the explicit treatment of one of the operator, these substeps might not have a solution. For example, if the operator K has one of more eigen values with modulus higher than 1, the transport steps, which treat K explicitly, are unstable.

This happens regularly when we apply ISO for the numerical simulation of the ISU process. In that case, we simply ignore the convergence failure and go to the next step. Many times, ISO converges despite this problem. More generally, our numerical experiments showed that the performance of the method was improved by fixing a maximum number N of Newton's iterations for each substep. For the test cases considered in this work, choosing $N = 5$ gave the best results.

We also observed that the choice of u_0^* can have a large impact on the convergence of ISO. However, we were unable to find a better choice that $u_0^* = u^n$. Finding the right guess that ensured the stability of the splitting iteration could potentially make ISO applicable for the numerical simulation of ISU.

B.4 Validation

Our implementations of FIM, IMPES and AIM were validated by considering three 1D PDE with analytical solution:

1. Buckley-Leverett
2. Advection-heat diffusion with constant coefficients
3. Advection-reaction with constant coefficients

We then validated our splitting methods with an advection-heat diffusion-reaction with constant coefficients by comparison with FIM.

B.4.1 Buckley-Leverett

The Buckley-Leverett equation is used to model incompressible immiscible two-phase flow in porous media. We consider a 1D reservoir which is initially filled with oil (S_o=0). We inject water on the left end at constant rate and we produce fluid on the right end at constant pressure. Both phases are assumed incompressible so that the total velocity $v_t = v_w + v_o$ is constant. The Buckley-Leverett equation is given by:

$$\frac{\partial S_w}{\partial t} = -\frac{v_t}{\phi} f_w'\left(S_w\right) \frac{\partial S_w}{\partial x} \tag{B.43}$$

where f_w is the water fractional flow. For simplicity, we neglect the effects due to gravity and capillary pressure, so that the fractional flow is simply the ratio of the water mobility λ_w to the total mobility of the fluid $\lambda_t = \lambda_w + \lambda_o$:

$$f_w = \frac{\lambda_w}{\lambda_t} \tag{B.44}$$

By defining the dimensionless space variable $x_D = x/L$ and the dimensionless time variable $t_D = tv_t/(\phi L)$, we obtained the dimensionless Buckley-Leverett equation:

$$\frac{\partial S_w}{\partial t_D} = -f'_w\left(S_w\right)\frac{\partial S_w}{\partial x_D} \tag{B.45}$$

To develop a solution, Equation B.45 must be reduced to one dependent variable. Since $S_w = S_w\left(x,t\right)$:

$$dS_w = \left(\frac{\partial S}{\partial x_D}\right)_{t_D} dx_D + \left(\frac{\partial S}{\partial t_D}\right)_{x_D} dt_D \tag{B.46}$$

By tracing a fixed saturation line through the domain, that is $\frac{dS_w(x_D,t_D)}{dt_D}_{|S_w} = 0$

$$\left(\frac{dx_D}{dt_D}\right)_{S_w} = -\frac{\left(\partial S_w/\partial t_D\right)_{x_D}}{\left(\partial S_w/\partial x_D\right)_{t_D}} \tag{B.47}$$

Since f_w is a function of S_w only:

$$\left(\frac{\partial f_w}{\partial x_D}\right)_{t_D} = \left(\frac{\partial f_w}{\partial S_w}\right)_{t_D} \cdot \left(\frac{\partial S_w}{\partial x_D}\right)_{t_D} \tag{B.48}$$

Substituting Equations B.47 and B.48 into Equation B.45, we obtain the frontal advance equation:

$$\frac{dx_D}{dt_D}_{|S_w} = f'\left(S_w\right) \tag{B.49}$$

Since Equation B.47 is only valid for $\left(\partial S_w/\partial x_D\right)_{t_D} \neq 0$, Equation B.49 describes the displacement of a shock front with saturation $S_w = S_f$. By integrating the conservation equation B.45 on the right end of the front, we obtain the shock saturation equation:

$$S_f f'_w\left(S_f\right) = f_w\left(S_f\right) \tag{B.50}$$

The position of the front is then given by:

$$x_f = t_D f'_w\left(S_f\right) \tag{B.51}$$

Therefore, the analytical solution of Equation B.43 writes:

$$\begin{aligned} &\text{If} \quad S_w \geq S_f \\ &\qquad x_D\left(S_w, t_D\right) = t_D f'_w\left(S_w\right) \\ &\text{If} \quad x_D > x_f \\ &\qquad S_w = 0 \end{aligned} \tag{B.52}$$

Figure B.2 shows the saturation profiles for (a) $\mu_o/\mu_w = 1$ and (b) $\mu_o/\mu_w = 5$ at dimensionless time $t_D = 0.5$ obtained with FIM, IMPES and AIM, and with the analytical solution. The results were obtained with a grid containing 50 cells and a dimensionless time-step of 0.01. For $\mu_o/\mu_w = 1$, the maximum CFL is 0.8. IMPES gives a more accurate result than FIM. Since CFL<1 for every cell, AIM uses IMPES except for the two cells containing a well. For $\mu_o/\mu_w = 0.5$, the maximum CFL is 1.2. IMPES is unstable. We observe than the water saturation is non-monotonous near the front. In this case, AIM uses 20% of FIM cells in average and we obtain a stable solution.

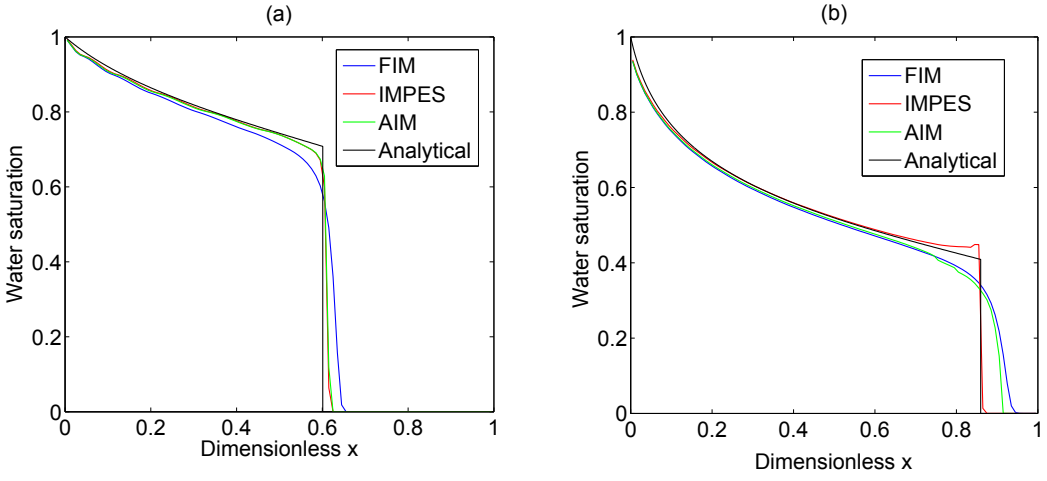

FIGURE B.2: Comparison of numerical and analytical solution for dimensionless Buckley-Leverett equation B.45 at $t_D = 0.5$ for $k_{rw}\left(S_w\right) = S_w^2$ with $\mu_o/\mu_w = 1$ and $\mu_o/\mu_w = 10$.

B.4.2 Advection-heat diffusion with constant coefficients

For this case, we consider a 1D porous media of length L initially filled with water at $T_0 = 20^oC$. We assume that the inert solid and the water have the same volumetric heat capacity, so that the overall volumetric capacity $\rho\gamma$ is constant. We set on the left end of the domain a constant temperature boundary condition $T_1 = 30^oC$ and a velocity v.

On the right end, we set a no heat flow $\partial T/\partial x = 0$ and constant pressure boundary condition. We assume that the water is incompressible so that the velocity is constant in the domain. Therefore, the energy equation B.9 becomes:

$$\rho\gamma\frac{\partial T}{\partial t} = \kappa\frac{\partial^2 T}{\partial x^2} - v\rho\gamma\frac{\partial T}{\partial x} \tag{B.53}$$

The time scale of the heat conduction in the domain is defined by:

$$\tau = \frac{\rho\gamma L^2}{\kappa} \tag{B.54}$$

By defining the dimensionless variables $x_D = x/L$, $t_D = t/\tau$ and $T_D = (T - T_0)\,/\,(T_1 - T_0)$, we obtained the dimensionless advection-diffusion equation:

$$\frac{\partial T_D}{\partial t_D} = \frac{\partial^2 T_D}{\partial x_D^2} - \lambda\frac{\partial T_D}{\partial x_D} \tag{B.55}$$

where $\lambda = v\tau/L$ is the advection constant. An approximated analytical solution of Equation B.55 has been proposed by Siemienuich and Gladwell [80]:

$$\begin{aligned} T_D\left(x_D, t_D\right) \quad &= \frac{1}{2}\left\{\operatorname{erfc}\left(\frac{x_D - \lambda t_D}{2\sqrt{t_D}}\right) + \operatorname{erfc}\left(\frac{x_D + \lambda t_D}{2\sqrt{t_D}}\right)\right\} \\ &+ \exp\left(-\lambda\right)\left(1 + \frac{\lambda\left(2 - x_D - \lambda t_D\right)}{2}\right)\operatorname{erfc}\left(\frac{2 - x_D + \lambda t_D}{2\sqrt{t_D}}\right) \\ &- \exp\left(-\lambda\right)\lambda\sqrt{\frac{t_D}{\pi}}\exp\left(-\frac{\left(2 - x_D - \lambda t_D\right)^2}{4t_D}\right) \end{aligned} \tag{B.56}$$

Figure B.3 shows the temperature profiles at dimensionless time $t_D = 0.5$ for (a) $\lambda = 0.1$ and (b) $\lambda = 1.0$ obtained with FIM and the analytical solution. The results were obtained with a grid containing 50 cells. Since the conduction part of the temperature CFL condition (Equation B.33) is proportional to Δx^2, we use a very small dimensionless time-step of 0.001. The maximum CFL obtained is 5.005 for $\lambda = 0.1$ and 5.05 for $\lambda = 1.0$. Since CFL> 1, IMPES cannot be used for this case.

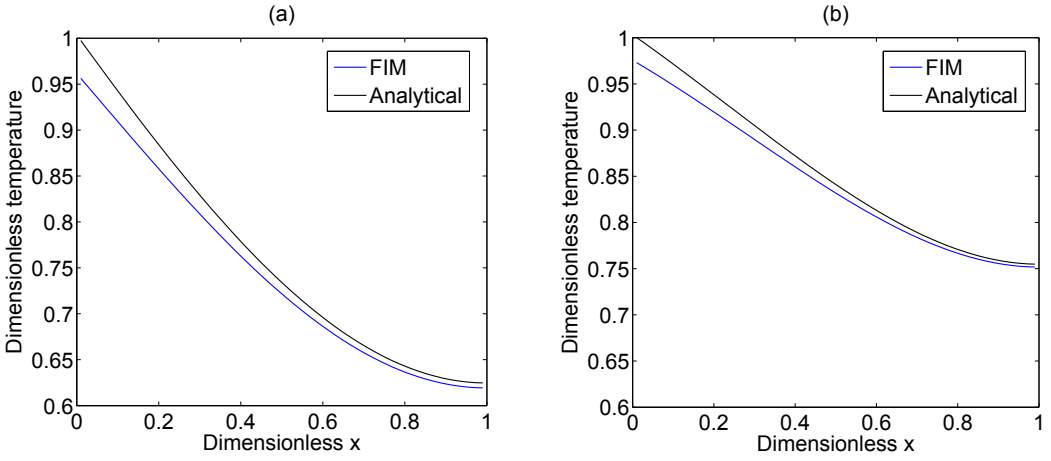

FIGURE B.3: Comparison of numerical and analytical solution for dimensionless advection-diffusion equation B.55 at $t_D = 0.5$ with (a) $\lambda = 0.1$ and (b) $\lambda = 1.0$. The results were obtained with a grid containing 50 cells and a dimensionless time-step of 0.001.

B.4.3 Advection-reaction with constant coefficients

We consider a 1D porous media of length L and a fluid model with two water components: a reactant R and a product P. R decomposes with the reaction:

$$R \xrightarrow{r} P \tag{B.57}$$

The reaction is a first-order decay, so the chemical rate is equal to:

$$r = K\phi\zeta_R\rho_w \tag{B.58}$$

Initially, we have $\zeta_R = 0$. We inject on the left end of the domain with constant velocity v and we produce at the right end with constant pressure. The water is assumed incompressible so that the velocity is constant through the domain. The conservation of component R writes:

$$\phi\rho_w\frac{\partial\zeta_R}{\partial t} = -\rho_w v\frac{\partial\zeta_R}{\partial x} - K\phi\rho_w\zeta_R \tag{B.59}$$

By defining the dimensionless variables $x_D = x/L$ and $t_D = tv/(\phi L)$, we obtain the dimensionless advection with first-order decay equation:

$$\frac{\partial \zeta_R}{\partial t_D} = -\frac{\partial \zeta_R}{\partial x_D} - D_K \zeta_R \tag{B.60}$$

where $D_K = K\phi L/v$ is the Damköhler number of the reaction. This equation has the following analytical solution:

$$\begin{aligned} &\text{If} \quad x_D \leq t_D \\ &\qquad \zeta_R = exp\,(-D_K x_D) \\ &\text{If} \quad x_D > x_f \\ &\qquad \zeta_R = 0 \end{aligned} \tag{B.61}$$

Figure B.4 shows the reactant mole fraction profiles for (a) $D_K = 0.1$ and (b) $D_K = 1.0$ at dimensionless time $t_D = 0.5$ obtained with FIM, IMPES and AIM, and with the analytical solution. The results were obtained with a grid containing 50 cells and a dimensionless time-step of 0.01. The CFL numbers are constant equal 0.5 in the domain. Therefore, IMPES is stable and AIM uses IMPES everywhere except for the cells which include a well, which are taken implicitly.

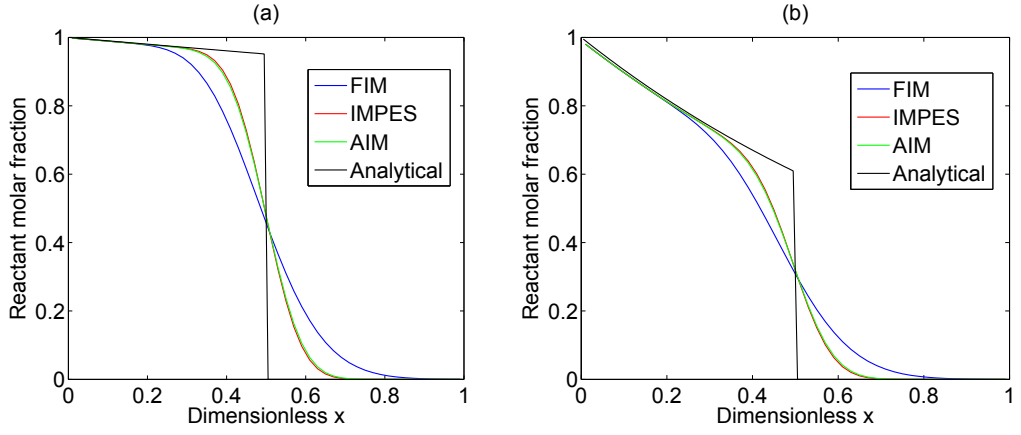

FIGURE B.4: Comparison of numerical and analytical solution for dimensionless advection-reaction with constant coefficient B.60 at $t_D = 0.5$ with (a) $K = 0.1$ and (b) $K = 1.0$. The results were obtained with a grid containing 50 cells and a dimensionless time-step of 0.01.

B.4.4 Advection-diffusion-reaction with constant coefficients

To validate our splitting method, we consider a simple advection-diffusion-reaction problem which is a combination of 2 and 3 but with a reaction enthalpy to couple the two equations:

$$\begin{aligned} \rho\gamma\frac{\partial T}{\partial t} &= \kappa\frac{\partial^2 T}{\partial x^2} - v\rho\gamma\frac{\partial T}{\partial x} - \Delta h_r K\phi\rho\zeta_R \\ \phi\rho\frac{\partial \zeta_R}{\partial t} &= -\rho v\frac{\partial \zeta_R}{\partial x} - K\phi\rho\zeta_R \end{aligned} \tag{B.62}$$

We assume for simplicity that the two time constants $\frac{\rho\gamma L^2}{\kappa}$ and $\frac{L\phi}{v}$ are equal. Therefore, by using the dimensionless variables $x_D = x/L$, $t_D = t/\tau$ and $T_D = (T - T_0)\,/\,(T_1 - T_0)$, we obtained the following system:

$$\begin{aligned} \frac{\partial T_D}{\partial t_D} &= \frac{\partial^2 T_D}{\partial x_D^2} - \phi\frac{\partial T}{\partial x} - \Delta h_r^* D_K\zeta_R \\ \frac{\partial \zeta_R}{\partial t_D} &= -\frac{\partial \zeta_R}{\partial x_D} - D_K\zeta_R \end{aligned} \tag{B.63}$$

where $D_K = K\tau$ is the Damköhler number and $\Delta h_r^* = \frac{\phi\Delta h_r}{\gamma(T_1 - T_0)}$ is the reduced reaction enthalpy.

Figure B.5 shows the temperature and reactant mole fraction profiles at dimensionless time $t_D = 0.5$ obtained with FIM, SSO-AK, SSO-KA, SMSO, SSO-CKA. The results were obtained with a grid containing 50 cells and a dimensionless time-step of 0.05. ISO is the most accurate method since we cancel the splitting error by iterations. For this case, ISO performs three splitting iterations in average, so it requires roughly three time more computation than FIM. We observe than SMSO gives the best compromise between accuracy and performance of all splitting methods.

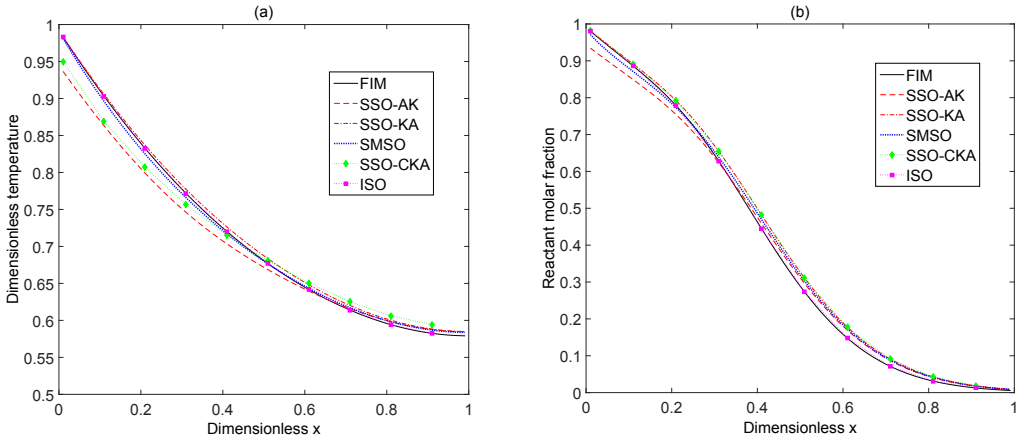

FIGURE B.5: Comparison of numerical and analytical solution for dimensionless advection-heat diffusion-reaction with constant coefficient B.63 at $t_D = 0.5$ with $\phi = 0.1$, $K = 1.0$ and $\Delta h_r^* = 1.0$. For this case, ISO performs three splitting iterations in average, so it requires roughly three time more computation than FIM. We observe than SMSO gives the best compromise between accuracy and performance of all splitting methods.

Bibliography

[1] T. Al Darouich, F. Behar, and C. Largeau. Thermal cracking of the light aromatic fraction of Safaniya crude oil – Experimental study and compositional modelling of molecular classes. *Organic Geochemistry*, 37:1130–1154, 2006.

[2] M. J. Anderson and P. J. Whitcomb. *DOE simplified: practical tools for effective experimentation.* Productivity Press, 2nd edition, 2007.

[3] M. Ashrafi, Y. Souraki, H. Karimaie, O. Torsaeter, and B. J. A. Bjorkvik. Experimental PVT property analyses for Athabasca bitumen. *Canadian Unconventional Resources Conference, Alberta, Canada, 15-17 November 2011*, 2011.

[4] D. Barry, K. Bajracharya, M. Crapper, H. Prommer, and C. Cunningham. Comparison of split-operator methods for solving coupled chemical non-equilibrium reaction/groundwater transport models. *Mathematics and computers in simulation*, 53(1-2):113–127, August 2000.

[5] D. A. Barry, C. T. Miller, and P. Culligan. Temporal discretisation errors in non-iterative split-operator approaches to solving chemical reaction/groundwater transport models. *Journal of Contaminant Hydrology*, 22:1–17, 1995.

[6] D. A. Barry, C. T. Miller, P. Culligan, and K. Bajracharya. Analysis of split-operator methods for non-linear and multispecies groundwater chemical transport models. *Mathematics and Computers in Simulation*, 43:331–341, 1997.

[7] F. Behar, F. Lorant, and M. Lewan. Role of NSO compounds during primary cracking of a type II Kerogen and a type III Lignite. *Organic Geochemistry*, 39: 1–22, 2008.

[8] F. Behar, F. Lorant, and L. Mazeas. Elaboration of a new compositional kinetic schema for oil cracking. *Organic Geochemistry*, 39:764–782, 2008.

[9] W. D. Bennon and F. P. Incropera. A continuum model for momentum, heat and species transport in binary solid-liquid phase change systems-I. Model formulation. *International Journal of Heat and Mass Transfer*, 30(10):2161–2170, 1987.

[10] M. A. Biot and D. G. Willis. The elastic coefficient of the theory of consolidation. *Journal of Applied Mechanics*, 24:594–601, 1957.

[11] G. E. P. Box and K. B. Wilson. On the experimental attainment of optimum conditions. *Journal of the Royal Statistical Society*, 13(B):1–45, 1951.

[12] R. L. Braun and A. K. Burnham. Mathematical model of oil generation, degradation, and expulsion. *Energy & Fuels*, 4(2):132–146, April 1990.

[13] J. C. Butcher. *Numerical methods for ordinary differential equations*. John Wiley & Sons Ltd, 2nd edition, 2008.

[14] R. M. Butler. Steam-assisted gravity drainage: concept, development, performance and future. *The Journal of Canadian Petroleum Technology*, 33(2):44–50, Feb 1994.

[15] R. M. Butler. SAGD Comes to age! *The Journal of Canadian Petroleum Technology*, 37(7):9–12, Jul 1998.

[16] R. M. Butler and D. J. Stephens. The gravity drainage of steam-heated heavy oil to parallel horizontal wells. *The Journal of Canadian Petroleum*, 20(2):90–96, Apr-Jun 1981.

[17] H. Cao, H. A. Tchelepi, J. Wallis, and H. Yardumian. Parallel scalable unstructured CPR-type linear solver for reservoir simulation. *SPE Annual Technical Conference and Exhibition, 9-12 October 2005, Dallas, Texas*, 2005.

[18] J. Carrayrou, R. Mose, and P. Behra. Operator-splitting procedures for reactive transport and comparison of mass balance errors. *Journal of Contaminant Hydrology*, 68:239–268, 2004.

[19] CMG-STARS. *User's guide*. Computer Modeling Group Ltd, 2012.

[20] K. H. Coats. IMPES stability: selection of stable timesteps. *SPE Journal*, 8(2): 181–187, June 2003.

[21] A. T. Corey. The interrelation between gas and oil relative permeabilities. *Producers monthly*, 19(1):38–41, 1954.

[22] P. M. Crawford and K. Biglarbigi. Advances in world oil-shale production technologies. *SPE Annual Technical Conference and Exhibition, 21-24 September 2008, Denver, Colorado, USA*, 2008.

[23] M. Delshad, S. G. Thomas, and M. F. Wheeler. Parallel numerical reservoir simulations of nonisothermal compositional flow and chemistry. *SPE Journal*, 16(2): 181–187, June 2011.

[24] Y. Fan, L. Durlofsky, and H. Tchelepi. Numerical simulation of the in-situ upgrading of oil shale. *SPE Reservoir Simulation Symposium, 2-4 February 2009, The Woodlands, Texas, USA*, 2010.

[25] I. Farago. A modified iterated operator splitting method. *Applied Mathematical Modelling 32*, 32:1542–1551, 2007.

[26] I. Farago, G. Boglarka, and A. Havasi. Additive and iterative operator splitting methods and their numerical investigation. *Computers and Mathematics with Applications*, 55:2266–2279, 2008.

[27] J. Florio, J. B. Henderson, F. L. Test, and R. Hariharan. A study of the effects of the assumption of local-equilibrium on the overall thermally-induced response of decomposing, glass-filled polymer composite. *International Journal of Heat and Mass Transfer*, 34(4):135–147, 1991.

[28] T. Fowler and H. Vinegar. Oil shale ICP-Colorado field pilot. *SPE Western Regional Meeting, 24-26 March 2009, San Jose, California, USA*, 2009.

[29] J. Geiser. Consistency of iterative operator-splitting methods: Theory and applications. *Numerical Methods for Partial Differential Equations*, 26:135–158, January 2010.

[30] J. Gersten, V. Fainberg, G. Hetsroni, and Y. Shindler. Kinetic study of the thermal decomposition of polypropylene, oil shale, and their mixture. *Fuel*, 79(13):1679–1686, Oct 1999.

[31] R. B. C. Gharbi. Dimensionally scaled miscible displacements in heterogeneous permeable media. *Transport in Porous Media*, 48(3):271–290, 2002.

[32] E. Hairer and G. Wanner. *Solving Ordinary Differential Equations II.* Springer, 2nd revised edition, 1996.

[33] E. Hairer, S. Nørsett, and G. Wanner. *Solving Ordinary Differential Equations I.* Springer, 2nd revised edition, 1996.

[34] J. B. Henderson and T. E. Wiecek. A numerical study of the thermally-induced response of decomposing, expanding polymer composites. *Wärme und Stoffübertragung*, 22(5):275–284, 1988.

[35] J. B. Henderson, Y. P. Verma, M. R. Tant, and G. R. Moore. Measurement of the thermal conductivity of polymer composites to high temperatures using the line source technique. *Polymer Composites*, 4:219–224, 1983.

[36] J. B. Henderson, J. A. Wiebelt, and M. R. Tant. A model for the thermal response of polymer composite materials with experimental verification. *Journal of Composite Matererials*, 19:579–595, 1985.

[37] J. B. Henderson, W. D. Emmerich, L. Hagemann, and E. Post. Thermophysical property measurement on a complex high-temperature polymer composite. *High temperatures high pressures*, 25(6):693–698, 1993.

[38] J. Herzer and W. Kinzelbach. Coupling of transport and chemical processes in numerical transport models. *Geoderma*, 44:115–127, 1989.

[39] W. J. Hill and W. G. A. Hunter. A review of response surface methodology: a litterature survey. *Technometries*, 8:571–590, 1966.

[40] W. Hundsdorfer and J. G. Verwer. A note on splitting error for advection-reaction equations. *Applied Numerical Mathematics*, 18:191–199, 1995.

[41] W. Hundsforfer and J. G. Verwer. *Numerical Solution of Time-Dependent Advection-Diffusion-Reaction Equations.* Springer-Verlag, Berlin, Germany, 2003.

[42] A. A. Jennings, K. D. J., and T. T. L. Multicomponent equilibrium chemistry in groundwater quality models. *Water Resources Research*, 18(4):1089–1096, 1982.

[43] R. W. Johnson. *The Handbook of Fluid Dynamics.* Boca Raton; London: CRC Press, 1998.

[44] J. J. Kaluarachchi and J. Morshed. Critical-assessment of the operator-splitting technique in solving the advection-dispersion-reaction equation. 1 first-order reaction. *Advances in Water Resources*, 18(2):89–100, 1995.

[45] J. F. Kanney, C. T. Miller, and C. T. Kelley. Convergence of iterative split-operator approaches for approximating non-linear reactive transport problems. *Advances in Water Resources*, 26:247–261, 2003.

[46] E. J. Kansa, H. E. Perler, and R. F. Chaiken. Mathematical model of wood pyrolysis including internal convection force. *Combustion and Flame*, 29:311–324, 1977.

[47] C. T. Kelley. *Solving nonlinear equations with Newton's method.* SIAM, 2003.

[48] M. Kobchenko, H. Panahi, F. Renard, D. K. Dysthe, A. Malthe-Sorenssen, A. Mazzini, J. Scheibert, B. Jamtveit, and P. Meakin. 4D imaging of fracturing in organic-rich shales during heating. *Journal of Geophysical Research*, 116(B12201), December 2011.

[49] J. Kumar, L. Fusetti, and B. Corre. Modeling in-situ upgrading of extra-heavy oils/-tar sands by subsurface pyrolysis. *Canadian Unconventional Resources Conference, 15-17 November 2011, Alberta, Canada*, 2011.

[50] A. Kværno. Singly diagonal implicit rung-kutta mehods with an explicit first stage. *BIT Numerical Mathematics*, 44:489–502, August 2004.

[51] D. Lanser and J. Verwer. Analysis of operator splitting for advection-diffusion-reaction problems from air pollution modelling. *Journal of Computational and Applied Mathematics 111 (1999) 201-216*, 111:201–216, 1999.

[52] K. Lee, G. J. Moridis, and C. A. Ehlig-Economides. Oil shale in-situ upgrading by steam flowing in vertical hydraulic fractures. *SPE Unconventional Resources Conference, 1-3 April, The Woodlands, Texas, USA*, 2014.

[53] K. Lee, G. J. Moridis, and C. A. Ehlig-Economides. A comprehensive simulation model of kerogen pyrolysis for the in-situ upgrading of oil shales. *SPE Reservoir Simulation Symposium, 23-25 February 2015, Houston, Texas, USA*, 2015.

[54] C. F. Leibovici and J. Neoschi. A solution of Rachford–Rice equations for multiphase systems. *Fluid Phase Equilib.*, 112:217–221, 1995.

[55] R. Lenth. Quick and easy analysis of unreplicated factorials. *Technometrics*, 31: 469–473, 1989.

[56] H. Li, J. C. Vink, and F. O. Alpak. An efficient multiscale method for the simulation of in-situ conversion processes. *SPE Journal*, 2014.

[57] P. Li and R. J. Chalaturnyk. History match of the UTF phase. A project with coupled reservoir geomechanical simulation. *The Journal of Canadian Petroleum Technology*, 48(1):29–35, Jan 2009.

[58] R. B. Lowrie. A comparison of implicit time integration methods for nonlinear relaxation and diffusion. *Journal of Computational Physics*, 196(2):566–590, 2004.

[59] J. Maes, A. Moncorgé, and H. Tchelepi. Thermal adaptive implicit method: Time step selection. *Journal of Petroleum Science and Engineering*, 106(10):34–45, 2013.

[60] J. L. McCauley. Models of permeability and conductivity of porous media. *Physica A*, 187(1-2):18–54, August 1992.

[61] R. F. Meyer, E. D. Attanasi, and P. Freeman. Heavy oil and natural bitumen resources in geological basins of the world. *US Geological Survey Open-File Report 2007-1084*, 2007.

[62] A. Miadonye, B. Singh, and V. R. Puttagunta. Modeling the viscosity-Ttmperature relationship of Alberta bitumens. *Fuel Sci. and Tech. International*, 12(2):335–350, 1994.

[63] R. T. Mifflin, J. W. Watts, A. Weiser, and U. Rice. A fully coupled, fully implicit reservoir simulator for thermal and other complex reservoir processes. *SPE Symposium on Reservoir Simulation, 17-20 February 1991, Anaheim, California*, 1991.

[64] D. C. Montgomery. *Design and Analysis of Experiments*. John Wiley and Sons, Inc., New York City, 5th edition, 2000.

[65] R. H. Myers, D. C. Montgomery, and C. M. Anderson-Cook. *Response Surface Methodology: Process and Product Optimization Using Design of Experiments*. John Wiley and Sons, Inc., Oxford, 3rd edition, 2009.

[66] R. H. Perry and D. W. Green. *Perry's Chemical engineering Handbook*. McGraw Hill, 6th edition, 1984.

[67] C. Phillips, R. Luymes, and T. Halahel. Enthalpies of pyrolysis and oxidation of Athabasca oil sands. *FUEL*, 61:639–646, July 1981.

[68] S. B. Pope and Z. Ren. Efficient implementation of chemistry in computational combustion. *Flow Turbulence and Combustion*, 82(4):437–453, June 2009.

[69] A. Prothero and A. Robinson. On the stability and accuracy of one-step methods for solving stiff systemsof ordinary differential equations. *Math. Comput.*, 28(125): 145–162, 1974.

[70] N. Puiroux, A. Prat, and M. Quintard. Non-equilibrium theories for macroscale heat transfer: Ablative composite layer systems. *International Journal of Thermal Sciences*, 43(6):541–554, 2004.

[71] D. L. Ropp and J. N. Shadid. Stability of operator splitting methods for systems with indefinite operators: Advection-diffusion-reaction systems. *Journal of Computational Physics*, 228:3508–3516, 2009.

[72] A. E. Ruark. Inspectional analysis: A method which supplements dimensional analysis. *Jour. Elisha Mitchell*, 51:127–133, 1935.

[73] T. F. Russell. Stability analysis and switching criteria for adaptive implicit methods based on the CFL condition. *SPE Reservoir Simulation Symposium, 6-8 February 1989, Houston, Texas, USA*, 1989.

[74] M. C. Ruzicka. On dimensionless numbers. *Chemical Engineering Research and Design*, 86(8a):835–868, 2008.

[75] L. A. Saputelli B., C. M. Canache P., and E. Lopez. Application of a non-equilibrium reaction model for describing horizontal well performance in foamy oils. *SPE international conference on horizontal well technology, 1-4 November, Calgary, Alberta, Canada*, 198.

[76] A. Shahbazi and M. Pooladi-Darvish. Application of operator splitting technique in numerical simulation of gas-hydrate reservoirs. *SPE Reservoir Simulation Symposium, 21-23 February 2011, The Woodlands, Texas, USA*, 2011.

[77] S. B. Shi, J. Liang, F. J. Yi, and G. D. Fang. Modelling of one-dimensional thermal response of silica-phenolic composites with volume ablation. *Journal of Composite Materials*, 47(18):2219–2235, 2013.

[78] M. Shook, D. Li, and W. L. Lake. Scaling immiscible flow through permeable media by inspectional analysis. *IN SITU*, 16(4):311–349, 1992.

[79] M. K. Shukla, F. J. Kastanek, and D. R. Nielsen. Inspectional analysis of convective-dispersive equation and application on measured breakthrough curves. *Soil Science Society of America Journal*, 66(4):1087–1094, 2002.

[80] J. L. Siemieniuch and I. Gladwell. Analysis of explicit difference methods for a diffusion-convection equation. *International Journal of Numerical Methods in Engeeniring*, 12:899–916, 1978.

[81] A. L. Siu and L. X. Nghiem. Modelling steam assisted gravity drainage process in the UTF. *SPE Annual Technical Conference and Exhibition, 6-9 October 1991, Dallas, Texas, USA*, 1991.

[82] R. Snow. In-situ upgrading of bitumen and shale oil by RF electrical heating. *SPE Heavy Oil Conference and Exhibition, 12-14 December 2011, Kuwait City, Kuwait*, 2011.

[83] J. E. J. Staggs. Heat and mass transport in developing chars. *Polymer Degradation and Stability*, 82(2):297–307, 2003.

[84] G. Strang. On the constuction and comparison of difference schemes. *SIAM Journal on Numerical Analysis*, 5(3):506–517, September 1968.

[85] B. Tissot and J. Espitalie. Thermal evolution of organic-matter in sediments - Application of a mathematical simulation - Petroleum potential of sedimentary basins and reconstructing thermal history sediments. *Revue de l'Institut Français du Pétrole*, 30(5):743–77, 1975.

[86] B. Tissot and D. Welte. *Petroleum formation and occurence.* Springer-Verlag, Berlin, Germany, seconded edition, 1984.

[87] P. Ungerer, F. Behar, and M. Villalba. Kinetic modeling of oil cracking. *Organic Geochemistry*, 13(4-6):857–868, 1988.

[88] A. J. Valocchi and M. Malmstead. Accuracy of operator splitting for advection-dispersion-reaction problems. *Water Resources Research*, 28(5):1471–1476, Mai 1992.

[89] J. W. Watts. A compositional formulation of the pressure and saturation equations. *SPE Reservoir Engineering*, 1(3):243–253, Mai 1986.

[90] G. Wilson. A modified Redlich-Kwong EOS, application to general physical data calculations. *Annual AIChE National Meeting, Cleveland, Ohio*, 1968.

[91] G. T. Yeh and V. S. Tripathi. A critical evaluation of recent developments in hydrogeochemical transport models of reactive multichemical components. *Water Resources Research*, 25(1):93–108, January 1989.

[92] R. Younis and M. Gerritsen. Multiscale process coupling by adaptive fractional stepping: an in-situ combustion model. *SPE/DOE symposium on improved oil recovery, 22-26 April 2006, Tulsa, Oklahoma, USA*, 2006.

[93] M. S. K. Youstos, E. Mastorakos, and R. S. Cant. Numerical simulation of thermal and reaction front for oil shale upgrading. *Chemical Engineering Science*, 94:200–213, May 2013.

[94] A. Zhou and Z. Yu. Effect of flame heat flux on thermal response and fire properties of char-forming composite materials. *Fire and Materials*, 38:100–110, 2014.